

Electronic Thesis and Dissertation Repository

---

8-15-2011 12:00 AM

## Real-time Three-dimensional Photoacoustic Imaging

Michael B. Roumeliotis, *The University of Western Ontario*

Supervisor: Dr. Jeffrey Carson, *The University of Western Ontario*

A thesis submitted in partial fulfillment of the requirements for the Doctor of Philosophy degree in Medical Biophysics

© Michael B. Roumeliotis 2011

Follow this and additional works at: <https://ir.lib.uwo.ca/etd>



Part of the [Medical Biophysics Commons](#)

---

### Recommended Citation

Roumeliotis, Michael B., "Real-time Three-dimensional Photoacoustic Imaging" (2011). *Electronic Thesis and Dissertation Repository*. 227.

<https://ir.lib.uwo.ca/etd/227>

This Dissertation/Thesis is brought to you for free and open access by Scholarship@Western. It has been accepted for inclusion in Electronic Thesis and Dissertation Repository by an authorized administrator of Scholarship@Western. For more information, please contact [wlsadmin@uwo.ca](mailto:wlsadmin@uwo.ca).

REAL-TIME THREE-DIMENSIONAL PHOTOACOUSTIC IMAGING

(Spine title: REAL-TIME 3D PHOTOACOUSTIC IMAGING)

(Thesis format: Integrated-Article)

by

Michael B. Roumeliotis

Graduate Program in Medical Biophysics

A thesis submitted in partial fulfillment  
of the requirements for the degree of  
Doctor of Philosophy

The School of Graduate and Postdoctoral Studies  
The University of Western Ontario  
London, Ontario, Canada

© Michael B. Roumeliotis 2011

THE UNIVERSITY OF WESTERN ONTARIO  
SCHOOL OF GRADUATE AND POSTDOCTORAL STUDIES

## CERTIFICATE OF EXAMINATION

Supervisor

\_\_\_\_\_  
Dr. Jeffrey J.L. Carson

Supervisory Committee

\_\_\_\_\_  
Dr. Jerry Battista

\_\_\_\_\_  
Dr. James Lacefield

\_\_\_\_\_  
Dr. Terry Thompson

Examiners

\_\_\_\_\_  
Dr. Terry Peters

\_\_\_\_\_  
Dr. Hanif Ladak

\_\_\_\_\_  
Dr. Jagath Samarabandu

\_\_\_\_\_  
Dr. Roger Zemp

The thesis by

**Michael Barret Roumeliotis**

entitled:

**Real-time Three-dimensional Photoacoustic Imaging**

is accepted in partial fulfillment of the  
requirements for the degree of  
Doctor of Philosophy

Date \_\_\_\_\_

\_\_\_\_\_  
Chair of the Thesis Examination Board

# Abstract

Photoacoustic imaging is a modality that combines the benefits of two prominent imaging techniques; the strong contrast inherent to optical imaging techniques with the enhanced penetration depth and resolution of ultrasound imaging. PA waves are generated by illuminating a light-absorbing object with a short laser pulse. The deposited energy causes a pressure change in the object and, consequently, an outwardly propagating acoustic wave. Images are produced by using characteristic optical information contained within the waves.

We have developed a 3D PA imaging system by using a staring, sparse array approach to produce real-time PA images. The technique employs the use of a limited number of transducers and by solving a linear system model, 3D PA images are rendered.

In this thesis, the development of an omni-directional PA source is introduced as a method to characterize the shift-variant system response. From this foundation, a technique is presented to generate an experimental estimate of the imaging operator for a PA system. This allows further characterization of the object space by two techniques; the crosstalk matrix and singular value decomposition. Finally, the results of the singular value decomposition analysis coupled with the linear system model approach to image reconstruction, 3D PA images are produced at a frame rate of 0.7 Hz.

This approach to 3D PA imaging has provided the foundation for 3D PA images to be produced at frame rates limited only by the laser repetition rate, as straightforward system improvements could see the imaging process reduced to tens of milliseconds.

**Keywords:** Photoacoustic imaging, 3D imaging, Photoacoustic point source, System calibration, Crosstalk matrix, Singular value decomposition, Real-time imaging

# Co-Authorship

This section describes the contribution from various authors for the work completed in Chapters 2, 3, and 4 as well as Appendices 1 and 2.

**Chapter 2:** M. Roumeliotis, P. Ephrat, J. Patrick, J.J.L. Carson. "Development and characterization of an omni-directional photoacoustic point source for calibration of a staring 3D photoacoustic imaging system", *Optics Express* **17**(17), pp. 15228-15238, 2009.

Dr. Ephrat aided in the conceptual design of the PA system as well as contributed to discussion and analysis of results. Mr. Patrick aided in the design and construction of the PA system. Dr. Carson aided in project design, developed and coded software, edited the manuscript, and provided general project supervision. I aided in the design and construction of the PA system, designed and performed the experiments, analyzed and interpreted the results, and wrote the manuscript.

**Chapter 3:** M. Roumeliotis, R.Z. Stodilka, M.A. Anastasio, G. Chaudhary, H. Al-Abed, E. Ng, A. Immucci, J.J.L. Carson. "Analysis of a photoacoustic imaging system by the crosstalk matrix and singular value decomposition", *Optics Express* **18**(11), pp. 11406-11417, May 2010.

Drs. Stodilka and Anastasio contributed to the discussion and analysis, as it related to the interpretation of the crosstalk matrix and singular value decomposition. Mr. Chaudhury performed related simulated experiments. Mr. Ng and Mrs. Immucci both aided in the development and interfacing of the robot with Labview™ software. Dr. Carson aided in the project design, analysis of results, edited the manuscript, and provided general project supervision. I aided in project design, developed software in MATLAB®, performed all experiments, analyzed and interpreted the results, and wrote the manuscript.

**Chapter 4:** M. Roumeliotis, R.Z. Stodilka, M.A. Anastasio, E. Ng, J.J.L. Carson. "Singular value decomposition analysis of a photoacoustic imaging system and 3D imaging at 0.7 fps", *Optics Express*.

Drs. Stodilka and Anastasio as well as Mr. Ng contributed to the discussion and analysis, as it related to singular value decomposition. Dr. Carson aided in the project design, analysis of results, modified data acquisition and image display software in Labview™, edited the manuscript, and provided general project supervision. I aided in the project design, developed and coded image reconstruction software in MATLAB®, performed all experiments, analyzed and interpreted the results, and wrote the manuscript.

**Appendix 1:** M. Roumeliotis, G. Chaudhary, M.A. Anastasio, R. Stodilka, A. Immucci, E. Ng, J.J.L. Carson. "Analysis of a photoacoustic imaging system by singular value decomposition" SPIE Annual Meeting, Symposium on Biomedical Optics (BiOS), 7564-113, San Francisco, USA, 2010.

Mr. Chaudhary and Dr. Anastasio both contributed to the production of the simulated portion of the work. Dr. Stodilka and Dr. Anastasio contributed to the interpretation of the singular value decomposition results. Mrs. Immucci and Mr. Ng both aided in interfacing the robot with Labview™ software. Dr. Carson aided in project design, analysis of results, edited the manuscript, and general project supervision. I aided in project design, performed all experiments, developed and coded singular value decomposition software in MATLAB®, analyzed and interpreted results, and wrote the manuscript.

**Appendix 2:** M. Roumeliotis, M.A. Anastasio, J.J.L. Carson. "Estimate of effective singular values of a photoacoustic imaging system by noise characterization" SPIE Annual Meeting, Symposium on Biomedical Optics (BiOS), 7899-65, San Francisco, USA, 2011.

Dr. Anastasio aided in the interpretation of singular value decomposition and imaging concepts. Dr. Carson aided in project design, analysis of results, edited the manuscript, and general project supervision. I aided in project design, performed all experiments, developed and coded image reconstruction software in MATLAB®, analyzed and interpreted results, and wrote the manuscript.

# Acknowledgments

This project is certainly more than the culmination of simply my own work and thoughts. Without the support of many people, this could never have been possible.

To Jeff, my supervisor: you provided immeasurable support over the years through seemingly endless dedication and attention. Your genuine interest in research has cultivated a sense of learned scientific creativity that I did not think possible before pursuing my PhD. Thank you.

To Pinhas, my mentor: while you graduated relatively early in my PhD, the year of mentorship you provided was invaluable to the maturing of my approach to scientific research and cultivating my scientific personality.

I would like to acknowledge the financial support provided by a variety of funding sources through the duration of my time at UWO. This includes the Western Graduate Scholarship (WGRS), the Translational Breast Cancer Research Unit (TBCRU), and the Canadian Institutes of Health Research (CIHR).

Finally, I would like to thank my family and friends for their support and encouragement through the years. To my brothers, who have guided me through the normalcy of dedication and success. And to my parents, who have provided me limitless support through not only this PhD, but my entire life. Without their support, this achievement would not be possible.

# Table of Contents

Certificate of Examination.....	ii
Abstract.....	iii
Co-Authorship .....	iv
Acknowledgments .....	vi
Table of Contents.....	vii
Table of Figures.....	xv
List of Appendices.....	xxi
List of Abbreviations and Symbols .....	xxii
Preface .....	xxiv
Chapter 1: Introduction.....	1
1.1 Background.....	1
1.1.1 Imaging .....	1
1.1.2 Optical imaging .....	2
1.1.3 Photoacoustic imaging.....	4
1.2 Photoacoustic Imaging Theory .....	4
1.2.1 Photoacoustic wave generation .....	5
1.2.2 Photoacoustic wave propagation .....	6
1.2.3 The photoacoustic wave in the time domain .....	7
1.2.4 The photoacoustic wave in the frequency domain .....	11



1.2.5 Photoacoustic image reconstruction .....	12
1.3 Photoacoustic Imaging Approaches .....	15
1.3.1 2D photoacoustic imaging approaches .....	15
1.3.2 3D photoacoustic imaging approaches .....	17
1.3.3 Photoacoustic imaging in real-time .....	19
1.4 Photoacoustic System Characterization .....	19
1.4.1 System characterization approaches .....	20
1.5 Photoacoustic System Analysis .....	21
1.5.1 The linear system model and the imaging operator .....	22
1.5.2 The crosstalk matrix .....	23
1.5.3 Singular value decomposition .....	24
1.6 Imaging Tasks and Singular Value Decomposition ....	26
1.6.1 Pseudoinverse of the imaging operator .....	26
1.6.2 Regularization of the imaging operator .....	27
1.7 Motivation and Objectives .....	28
1.8 References .....	29
Chapter 2: Development and characterization of an omnidirectional photoacoustic point source for calibration of a staring 3D photoacoustic imaging system.....	38
2.1 Introduction .....	38

2.1.1 Background.....	38
2.1.2 Objective and approach .....	40
<b>2.2 Methods .....</b>	<b>41</b>
2.2.1 The photoacoustic imaging system .....	41
2.2.2 Source uniformity characterization .....	42
2.2.3 Source directionality characterization .....	43
2.2.4 System calibration scan .....	44
<b>2.3 Results .....</b>	<b>44</b>
2.3.1 Source uniformity characterization .....	44
2.3.2 Source directionality characterization .....	45
2.3.3 System calibration scan .....	46
<b>2.4 Discussion.....</b>	<b>48</b>
2.4.1 Overview of basic findings.....	48
2.4.2 MB <sup>+</sup> /IL as a PA source .....	49
2.4.3 Variation in PA signal intensity as a function of zenith and azimuth .....	50
2.4.4 Calibration maps .....	50
2.4.5 Impact of calibration maps on image reconstruction .....	51
2.4.6 Advantages/Disadvantages of approach.....	52
2.4.7 Future work.....	53
<b>2.5 Conclusion .....</b>	<b>53</b>

2.6 References .....	54
Chapter 3: Analysis of a photoacoustic imaging system by the crosstalk matrix and singular value decomposition.....	57
3.1 Introduction .....	57
3.1.1 Background.....	57
3.1.2 Singular value decomposition .....	59
3.1.3 The crosstalk matrix .....	59
3.1.4 Objective.....	59
3.1.5 Approach .....	60
3.2 Methods .....	60
3.2.1 Photoacoustic imaging system .....	60
3.2.2 System calibration scan .....	61
3.2.3 Singular value decomposition and singular vector correlation .....	63
3.2.4 The crosstalk matrix .....	63
3.3 Results .....	64
3.3.1 Crosstalk sensitivity and aliasing .....	64
3.3.2 Singular value decomposition: Singular vectors .....	65
3.4 Discussion.....	67
3.4.1 Crosstalk sensitivity and aliasing .....	67
3.4.2 Singular value decomposition .....	69

3.4.3 Computation considerations .....	71
3.4.4 Imaging considerations.....	71
3.5 Conclusion .....	72
3.6 References .....	72
Chapter 4: Singular value decomposition analysis of a photoacoustic imaging system and 3D imaging at 0.7 fps .....	76
4.1 Introduction .....	76
4.1.1 Background.....	76
4.1.2 Singular value decomposition .....	78
4.1.3 Estimate of effective singular values.....	78
4.1.4 Experimental objective.....	79
4.2 Methods .....	80
4.2.1 Photoacoustic imaging system .....	80
4.2.2 System calibration scan .....	80
4.2.3 Singular value decomposition .....	81
4.2.4 Regularized pseudoinverse image reconstruction .....	81
4.2.5 Real-time photoacoustic imaging.....	82
4.3 Results .....	83
4.3.1 Estimate of matrix rank .....	83

4.3.2 Image reconstruction of objects with different transducer count ...	86
4.3.3 Image reconstruction of objects with different measurement space temporal sampling rate .....	87
4.3.4 Image reconstruction of a point source in real-time (1.4 seconds per frame).....	88
<b>4.4 Discussion.....</b>	<b>89</b>
4.4.1 Estimate of matrix rank .....	89
4.4.2 Image reconstruction of objects with different transducer count ...	92
4.4.3 Image reconstruction of objects with different measurement space temporal sampling rate .....	93
4.4.4 Real-time imaging of a photoacoustic point-like source.....	93
4.4.5 Implications to previous work .....	95
4.4.6 Technical Considerations for faster 3D frame rates.....	95
<b>4.5 Conclusion .....</b>	<b>96</b>
<b>4.6 References .....</b>	<b>97</b>
<b>Chapter 5: Discussion and future work.....</b>	<b>99</b>
<b>5.1 Technology Development.....</b>	<b>99</b>
5.1.1 Calibration protocol.....	99
5.1.2 System improvements.....	101
<b>5.2 Characterization Technique Improvements .....</b>	<b>102</b>
5.2.1 The crosstalk matrix .....	103

5.2.2 Singular value decomposition .....	103
5.3 Applications .....	104
5.3.1 Contrast tracking.....	104
5.3.2 Object tracking .....	105
5.4 Recommendations.....	105
5.4.1 Weaknesses.....	105
5.5 Conclusions .....	107
5.6 References .....	109
Appendix 1: Analysis of a photoacoustic imaging system by singular value decomposition .....	110
A1.1 Introduction.....	110
A1.1.1 Background.....	110
A1.1.2 Singular value decomposition .....	111
A1.2 Methods .....	112
A1.3 Results .....	113
A1.4 Discussion.....	115
A1.5 Conclusion .....	117
A1.6 References.....	118

Appendix 2: Estimate of effective singular values of a photoacoustic imaging system by noise characterization .....	119
A2.1 Introduction.....	119
A2.1.1 Background.....	119
A2.1.2 Singular value decomposition .....	120
A2.2 Methods .....	121
A2.2.1 The photoacoustic system.....	121
A2.2.2 The imaging operator.....	121
A2.3 Results .....	122
A2.4 Discussion.....	124
A2.5 Conclusion .....	125
A2.6 References.....	126
Curriculum Vitae .....	128

# Table of Figures

**Figure 1.1:** Pressure profile representing the resultant PA wave in the time domain for a spherical source of radius  $R_s$ . Representative of the solution to the forward model.....9

**Figure 1.2:** Velocity potential profile representing the resultant PA wave in the time domain for a spherical source of radius  $R_s$ . Representative of the solution to the backward model.....10

**Figure 1.3:** Spectrum amplitude of acoustic frequencies for spherical sources of varying dimension. Frequency content illustrated for PA sources of 1 mm diameter (solid) and 2mm diameter (dashed). .....11

**Figure 1.4:** 2D illustration of the backprojection principle. PA source located at the intersection of the arcs produced by each of the 3 transducers (T1, T2, T3), determined by the associated time of flight from PA source to transducer.....13

**Figure 2.1:** (a). Isometric view of the hemispherical PA imaging array illustrating the transducer arrangement, placement of the liquid reservoir, and the optical fibre PA source. (b). Isometric view of the system for detailed PA source characterization illustrating one transducer, the transducer arm, the liquid reservoir and the optical fibre. The transducer arm was capable of rotation in  $15^\circ$  increments in the zenith direction and  $22.5^\circ$  increments in the azimuthal direction. (c). Example of raw data acquired on



a single acoustic transducer. Signal time-of-flight, amplitude, and FWHM are labeled. ....42

**Figure 2.2:** (a). Peak-to-peak PA signal amplitude as a function of absorption ( $MB^+$ , top legend) and scatter (Intralipid<sup>TM</sup>) for a liquid PA point source. Error bars represent  $\pm$  one standard deviation. (b) Coefficient of variation for data corresponding to (a). ....45

**Figure 2.3:** Curves illustrating signal amplitude as a function of azimuthal position for varying zenith orientations. Error bars represent  $\pm$  one standard deviation. ....46

**Figure 2.4:** Calibration maps of the metrics describing the PA signal detected by each transducer at each position within the calibration volume. (a) Signal amplitude - the magnitude of the peak-to-peak voltage acquired (b) Signal width - the FWHM of the signal, and (c) Signal time-of-flight - a measure of the arrival time after laser trigger. ....47

**Figure 3.1:** (a) Isometric view of the hemispherical PA imaging array illustrating the transducer arrangement, placement of the liquid reservoir, and the optical fibre PA source. (b) Example of raw data acquired on a single acoustic transducer. ....61

**Figure 3.2:** Displays sensitivity of the PA system at each location in object space acquired from the main-diagonal of the crosstalk matrix corresponding to the  $30 \times 30 \times 30 \text{ mm}^3$ . Both x and y axes represent voxel number in the y

and z directions, respectively. Accordingly, each x-plane in object space is 10x10 voxels. ....64

**Figure 3.3:** (a) Illustrates aliasing from the center voxel for the 16x16x16 mm<sup>3</sup> scan (each x-plane is 8x8 voxels) while (b) shows aliasing from the same position for the 30x30x30 mm<sup>3</sup> scan (each x-plane is 10x10 voxels). (c) Shows representative aliasing plots from a voxel located at the corner of the object space for the 30x30x30 mm<sup>3</sup> scan (each x-plane is 10x10 voxels). ....65

**Figure 3.4:** (a) and (b) Displays the center y-z plane of the first 8 singular vectors acquired via experiment and de-noised, respectively. The field-of-view for each singular vector is 30x30 mm<sup>2</sup>. The singular vector number reads from left to right with the leftmost image representing singular vector 1.....66

**Figure 3.5:** (a) Displays the correlation among the set of 1000 corresponding singular vectors in the de-noised and experimental matrices,  $\mathbf{V}^T$ . (b) Shows the same computation as in (a) but in descending order for an imaging operator with (i) 1/4 the intrinsic system noise, (ii) 1/2 the intrinsic system noise, (iii) the experimental imaging operator, (iv) 2 times the intrinsic system noise, and (v) 5 times the intrinsic noise. The singular vector index changed with the order as the true singular vector number (corresponding to the matrix  $\mathbf{V}^T$ ) was unknown after the initial projection operations were completed. The vertical axis in both (a) and (b) is shared. .67

**Figure 4.1:** (a) Isometric view of the hemispherical PA imaging array illustrating the transducer arrangement. Columns with transducers lightly shaded in green correspond to zenith angles of  $22.5^\circ$ ,  $45^\circ$ , and  $67.5^\circ$  while columns with transducers lightly shaded blue correspond to zenith angles of  $33.75^\circ$ ,  $56.25^\circ$ , and  $78.75^\circ$ . (b) Represents an unfolded schematic of (a) whereby each plane of 5 transducers is referenced P1 through P6, with P1 representing the bottom-most row and P6 the top-most row. (c) Summarizes the results of the estimate of effective matrix rank on the 6 different transducer arrangements. (d) Semi-logarithmic plot of the magnitude of the singular values versus singular value index for each of the 6 transducer arrangements. Left-most curve corresponds to the 5 transducer imaging operator while right-most to the 30 transducer imaging operator with intermediate curves represent increasing transducer count from left to right. ....84

**Figure 4.2:** (a) Displays the estimated matrix rank for variable transducer count and arrangements. (b) Displays the estimated matrix rank for variable measurement space temporal sampling rates. Linear regression for (b) was performed only on the 4 data points contained within region (ii). The line is shown throughout the entire figure to show the expected value of the matrix rank. (c) Compares the expected matrix rank to the measured rank and is plotted as a percent error to highlight the deviation from linearity in regions (i) and (iii). (d) Provides a visual interpretation of the geometry associated with selected singular vectors for the imaging operator corresponding to the 30 transducer, 5 MHz temporal sampling rate. Images (i) through (iv) correspond to singular vectors of index 1, 10, 3632, and 4036.....86

**Figure 4.3:** Reconstruction of a simulated point, line, and multi-point source for each of the 6 transducer arrangements. The iterative technique was implemented on the system with 30 transducers and 5 MHz temporal sampling rate (shown in the column second from right). Ideal image based on phantom is shown in the right-most column. ....87

**Figure 4.4:** Reconstruction of a simulated point, line, and multi-point source for each of the 8 measurement space temporal sampling rates (MHz). .....88

**Figure 4.5:** 4D real-time photoacoustic imaging experiment where data acquisition and image reconstruction were performed in real time. Images were captured from a photoacoustic point-like source translated in the negative  $x$ -direction at a velocity of 0.40 mm/s. The interval between 3D photoacoustic images was 1.4 s and rate-limited by the data acquisition transfer speed, computational, and data storage overhead. The first row shows an  $xy$ -plane ( $z = 4$  mm). The second row shows the same reconstruction in a  $zy$ -plane ( $x = 7$  mm) and the third row displays an  $xz$ -plane ( $y = 11$  mm). Each column represents the 3D image data acquired at a specific point in time (indicated along bottom).....89

**Figure A1.1:** (a) and (b) Displays the center  $x$ - $y$  plane of the first 64 singular vectors acquired via experiment and simulation, respectively. The field-of-view for each singular vector is  $30 \times 30$  mm<sup>2</sup>. The singular vector number reads from left to right and top to bottom.....114

**Figure A1.2:** Plot indicates the magnitude of the first 1000 singular values acquired from the SVD matrix,  $\mathbf{S}$ . .....115

**Figure A2.1:** (a) Displays the magnitude of the singular values plotted against their index for the experimental imaging operator (red), the de-noised imaging operator (black), and the noise-only imaging operator (blue).  
.....123

**Figure A2.2:** (a) Shows the centre planes of the singular vectors at the 1<sup>st</sup> index for the experimental and noise-only imaging operators. (b) Shows the centre planes of the singular vectors at the 1555<sup>th</sup> index for the experimental and noise-only imaging operators. (c) Shows the centre planes of the singular vectors at the 3134<sup>th</sup> index for the de-noised and noise-only imaging operators.....124

# List of Appendices

A1 - Analysis of a photoacoustic imaging system by singular value decomposition .....110

A2 - Estimate of effective singular values of a photoacoustic imaging system by noise characterization .....119

# List of Abbreviations and Symbols

1D, 2D, 3D	One, two, three dimensional
cm	Centimeter
CT	Computed tomography
DAQ	Data acquisition
dB	Decibel
DOT	Diffuse optical tomography
FFT	Fast Fourier Transform
fps	Frames per second
FWHM	Full width at half-maximum
g	Gram
Hz	Hertz
IL	Intralipid™
J	Joule
K	Kelvin
kHz	Kilohertz
LOIS	Light-induced optoacoustic imaging system
MB <sup>+</sup>	Methylene blue
MHz	Megahertz
mJ	Millijoule
mM	Milli-molar
mm	Millimeter
MRI	Magnetic resonance imaging
ms	Millisecond
Nd:YAG	Neodymium-doped yttrium aluminum garnet
NIRS	Near infrared spectroscopy
ns	Nanosecond
OCT	Optical coherence tomography
OPO	Optical parametric oscillator

Pa	Pascal
PA	Photoacoustic
PAI	Photoacoustic imaging
PAM	Photoacoustic microscopy
PAT	Photoacoustic tomography
PC	Personal computer
PET	Positron emission tomography
PSF	Point spread function
RF	Radio frequency
s	Second
SNR	Signal-to-noise ratio
SPECT	Single-photon emission computed tomography
SVD	Singular value decomposition
US	Ultrasound
USB	Universal serial bus
VP	Velocity potential
$\mu\text{M}$	Micro-molar
$\mu\text{m}$	Micrometer
$\mu\text{s}$	Microsecond
$\emptyset$	Diameter



# Preface

This thesis summarizes the work completed through the duration of my PhD degree at The University of Western Ontario and Lawson Health Research Institute.

In Chapter 1, context and motivation for my research is described. A general overview of medical imaging is provided and the role of optical imaging in the field is given context. From here, a background of the photoacoustic principle and related mathematical models and techniques are described, which provides the foundation for my research. Finally, a current review of the major approaches to photoacoustic imaging and relevant applications are outlined.

Chapters 2 to 4 are based on manuscripts in peer-reviewed journals that were published over the course of my PhD. The first publication focused on the characterization and calibration of the photoacoustic imaging system; the second manuscript describes the experimental application of techniques used to characterize the imaging system; the third paper describes the implementation of earlier techniques to produce fast, 3D photoacoustic images. In Appendix 1 and 2, additional information is provided that was published as conference manuscripts. Each of these appendices provides supplemental work that was performed, usually as a lead-up to the peer-reviewed publications in Chapter 2, 3, and 4.

Chapter 5 provides a summary and discussion of the project in its entirety. General conclusions and foreseeable future work are discussed.

# Chapter 1:

## *Introduction*

This chapter includes a review of the role of optical imaging in the context of medical imaging. Photoacoustic imaging, a facet of optical imaging, employs the use of a pulsed laser to produce acoustic waves carrying optical information inherent to the light-absorbing object. In order to cultivate a broad understanding of the photoacoustic effect, the generation and propagation of a photoacoustic wave are described in detail. This leads to a broad summary of different approaches to photoacoustic imaging, including illumination schemes, detection schemes, and reconstruction techniques.

Broadly, the objective of this work was to develop a staring, sparse array, approach to produce fast, 3D, photoacoustic images. Since relatively few transducers were used to acquire measurements of the PA waves, it was necessary to characterize the shift-variant response of the imaging system. Calibration of the object space led to the characterization of the PA system by the crosstalk matrix and singular value decomposition. These foundations were built upon and led to a technique by which 3D image reconstruction could be accomplished at greatly improved frame rates from earlier work. This chapter also includes background relevant to understanding technical details introduced only briefly in Chapters 2, 3, and 4.

## **1.1 Background**

### *1.1.1 Imaging*

The scientific advancement of imaging technology has provided great motivation for the widespread use of imaging as a method to detect, diagnose, and treat human diseases in a clinical setting. Common imaging technologies include magnetic resonance imaging (MRI), x-ray computed tomography (CT), ultrasonography (US), single photon

emission computed tomography (SPECT), and positron emission tomography (PET). Each technology has established a niche in which it finds application based on the physical characteristic it seeks to differentiate. MRI provides strong anatomical contrast between soft tissues but does not display functional information and is associated with very high cost. CT produces images with very good resolution at imaging depths relevant to the human body and offers excellent contrast between bone and soft tissues. However, the images differentiate very little among varying soft tissues and is also limited in the frequency of use because it makes use of harmful ionizing radiation. Ultrasound detects differences in tissue density with relatively strong resolution and penetration depth. However, traveling acoustic waves are impeded by abrupt changes in density (bone and air) and contrast suffers greatly among soft tissues because the variations in density are relatively minor. SPECT and PET are both used to provide functional information by detecting the emissions of radioactive tracers injected in the human body. These tracers are designed such that they bind or localize to a specific site in the body and, therefore, imaging of the tracer becomes a surrogate marker for that functionality. Examples include myocardial perfusion imaging and brain blood flow. SPECT and PET are often used in conjunction with anatomical imaging systems to provide functional information with anatomical context. The preferential imaging modality used for a particular application can be one or more of these common clinical technologies because of differences in measured information.

### ***1.1.2 Optical imaging***

Optical imaging techniques provide an important complement to the already existing technologies as they offer strong contrast between optically absorbing objects. However, the foremost limitation of optical imaging modalities is poor resolution associated with the high scatter of photons in human tissue. In order to maintain high resolution information, only photons acquired from relatively small penetration depths (microns to a few centimeters) can be used. Common optical imaging techniques include diffuse optical tomography, optical coherence tomography, angular domain imaging, fluorescence imaging, and near infrared spectroscopy. Other variations of these

techniques exist but are all derived from either the measurement of ballistic or scattered photons.

Ballistic photon imaging regimes are those in which photons are not scattered. These photons retain their spatial information because the net interaction with the object has not perturbed the photon's direction of propagation. Therefore, high resolution optical images can be produced from ballistic photons but, in tissue, these images are generally limited to approximately a few millimeters in depth, significantly reducing widespread applicability of the technology [1,2].

Imaging in the quasiballistic regime, in which photons are minimally scattered, has been achieved. Angular domain imaging utilizes photons that have been minimally scattered as they maintain relatively high spatial detail of the object [3-5]. This technique implements the use of filters that serve to attenuate any photons significantly deviating from the initial transillumination pattern. The scattered photons that normally serve to obscure object information are eliminated, greatly increasing the depth at which useful optical information can be retrieved. Depending on the application, high resolution images can be produced at depths from a few millimeters to a few centimeters.

The alternative to ballistic optical imaging is the diffuse optical imaging regime. In this scheme, information is garnered from photons that have undergone significant interaction with the object. Consequently, spatial resolution is lost as depth penetration is increased. Common technologies operating in the diffuse photon detection regime include diffuse optical tomography (DOT) [2,6], near-infrared spectroscopy (NIRS) [1], as well as particular bioluminescent imaging techniques [7], and fluorescent imaging techniques [8]. Optical coherence tomography (OCT) is another example of optical imaging technology that primarily uses coherent scatter to generate images. Advances have been made in filtering photons based on time-gating and spatial filtering techniques to eliminate obscured information from multiple-scattered photons, allowing for increased imaging depth on the order of ~10 mm [2,9].

### ***1.1.3 Photoacoustic imaging***

Photoacoustic imaging is a hybrid imaging modality that serves to combine the advantages of optical imaging with that of acoustic imaging. Review papers are referenced to provide additional literature reviewing the current state-of-the-art [10-12]. As described in section 1.1.2, the primary drawback of optical imaging is the strong scatter of photons within human tissue. In order to overcome this limitation, imaging by the photoacoustic principle is enabled by the object's optical information being transported to transducers by acoustic waves. Acoustic waves aid in circumventing the issue of optical scatter because ultrasound waves attenuate much less significantly in human tissue ( $\sim 1\text{dB/cm/MHz}$ ). Characteristic features of the photoacoustic wave are determined by features inherent to the optically absorbent object [13]. This permits optical information to be retrieved from much greater penetration depths (a few centimeters) with resolution comparable to that of US imaging [14-16].

While the photoacoustic effect was discovered in the 1880s, it was not until the 1980s when Bowen [17] suggested a technique to produce soft-tissue images. Since, significant advances have been made and images were produced of excised tissue samples [18-20], animals [21-25], and finally humans [15,26].

## **1.2 Photoacoustic Imaging Theory**

Material in section 1.2.1 and 1.2.2 are adapted from "Biomedical Optics: Principles and Imaging", L.V. Wang and H.I. Wu, 2007.

Generally, photoacoustic imaging employs the use of pulsed laser radiation to illuminate the optically absorbing object very quickly. Objects exposed to the laser radiation convert the light to heat, resulting in a small temperature increase. The temperature increase instigates the thermoelastic expansion of the object and a localized pressure change. This causes an acoustic wave to propagate from the object where it can

be collected by ultrasound transducers. The characteristic information contained within the photoacoustic waves is used to perform image reconstruction.

### ***1.2.1 Photoacoustic wave generation***

In photoacoustic imaging, the generation of the wave is usually caused by a short laser pulse (usually a few nanoseconds). The required time scale over which the light must be delivered is determined by the time scale of energy dissipation and physical characteristics of the object exposed to the laser pulse, specifically, the thermal and stress relaxation times. The thermal relaxation time is described by:

$$\tau_{th} = \frac{d_c^2}{\alpha_{th}} \quad (1.1)$$

where  $\alpha_{th}$  is the thermal diffusivity ( $\text{m}^2/\text{s}$ ) and  $d_c$  is the characteristic dimension of the heated region. For soft tissues, the thermal diffusivity is on the order of  $10^{-7} \text{ m}^2/\text{s}$  [27]. Therefore, an object of dimension 1 mm will have an associated thermal relaxation time measured in the tens of seconds. However, this parameter scales with the square of the object dimension. Objects of 1  $\mu\text{m}$  have an associated thermal relaxation time in the tens of microseconds. The stress relaxation time is described by:

$$\tau_s = \frac{d_c}{v_s} \quad (1.2)$$

where  $v_s$  is the speed of sound in the respective medium ( $\sim 1500 \text{ m/s}$  in tissue). In objects with dimensions relevant to our imaging system (discussed later), the stress relaxation time is typically much smaller than the thermal relaxation time. Generally, the stress relaxation time is on the order of a few hundred ns for objects in the mm or sub-mm range. From time scales examined by this criterion, it is apparent why a short duration pulsed laser is used to produce photoacoustic waves.

The increase in temperature due to the absorbed laser energy can be written as:

$$T = \frac{\eta_{th} \mu_a F}{\rho C_V} \quad (1.3)$$

where  $\eta_{th}$  is the percentage of light converted to heat,  $\mu_a$  is the optical absorption coefficient ( $\text{cm}^{-1}$ ),  $F$  is the optical fluence,  $\rho$  is the density, and  $C_V$  is the specific heat capacity at constant volume. Typically in soft tissue,  $\rho$  is  $\sim 1 \text{ g/cm}^3$  and  $C_V$  is  $\sim 4 \text{ J/(g}\cdot\text{K)}$ . In representative soft tissue values, and a laser fluence of  $10 \text{ mJ/cm}^2$ , the temperature increase is on the order of a few tenths of a mK.

Provided the thermal and stress confinement criteria have been met, the local pressure change is:

$$p_0 = \frac{\beta T}{\kappa} \quad (1.4)$$

where  $\beta$  denotes the thermal coefficient of volume expansion ( $\text{K}^{-1}$ ) and  $\kappa$  is the isothermal compressibility ( $\text{Pa}^{-1}$ ). Typical soft tissue values are a  $\beta$  of  $4 \times 10^{-4} \text{ K}^{-1}$  and  $\kappa$  of  $5 \times 10^{-10} \text{ Pa}^{-1}$ . The dimensionless unit that relates the pressure increase to the deposited optical energy is the Grueneisen parameter:

$$\Gamma = \frac{\beta}{\kappa \rho C_V} = \frac{\beta v_s^2}{C_P} \quad (1.5)$$

where  $C_P$  is the specific heat capacity at constant pressure ( $\text{J/g}\cdot\text{K}$ ). For soft tissue, the Grueneisen parameter can be estimated by the following empirical formula:

$$\Gamma_{water} = 0.0043 + 0.0053T_0 \quad (1.6)$$

where  $T_0$  is the temperature in degrees Celsius. In soft tissue, the Grueneisen parameter is estimated at 0.24 and is considered relatively constant [28]. Then, assuming the conversion of light to heat is lossless, an expression describing the local pressure rise in an object is:

$$p_0 = \Gamma \mu_a F \quad (1.7)$$

where a typical value for  $\mu_a$  is  $0.1 \text{ cm}^{-1}$  and  $F$  is  $10 \text{ mJ/cm}^2$ , resulting in a pressure change of  $\sim 240 \text{ Pa}$ .

### ***1.2.2 Photoacoustic wave propagation***

The generalized wave equation is used to describe the propagation of the photoacoustic wave, described in section 1.2.1:

$$\left(\nabla^2 - \frac{1}{v_s^2} \frac{\partial^2}{\partial t^2}\right) p(\mathbf{r}, t) = \frac{\beta}{\kappa v_s^2} \frac{\partial^2 T(\mathbf{r}, t)}{\partial t^2} \quad (1.7)$$

where  $p(\mathbf{r}, t)$  indicates the pressure at location  $\mathbf{r}$  and time  $t$ , and  $T$  is the temperature rise. The left side of the equation describes the wave propagation and the right side describes the source term. Under the thermal confinement condition, the change in temperature directly relates to the energy deposition:

$$\rho C_V \frac{\partial T(\mathbf{r}, t)}{\partial t} = H(\mathbf{r}, t) \quad (1.8)$$

where temperature has become a time-dependent variable, and the heating function is related to the time-dependent optical fluence. Eq. (1.7) is modified to describe the wave generation at thermal confinement:

$$\left(\nabla^2 - \frac{1}{v_s^2} \frac{\partial^2}{\partial t^2}\right) p(\mathbf{r}, t) = -\frac{\beta}{c_p} \frac{\partial H}{\partial t} \quad (1.9)$$

Because the source term on the right side of the equation is related to  $H$  by the first time derivative, an invariant heating function will not produce a pressure wave.

The general approach to solving Eq. (1.9) is accomplished by applying a Green's function. The method is a common technique used to solve inhomogeneous differential equations. The solution is expressed in Eq. (1.10):

$$p(\mathbf{r}, t) = \frac{1}{4\pi v_s^2} \frac{\partial}{\partial t} \left[ \frac{1}{v_s t} \int d\mathbf{r}' p_0(\mathbf{r}') \delta\left(t - \frac{|\mathbf{r}-\mathbf{r}'|}{v_s}\right) \right] \quad (1.10)$$

where  $\mathbf{r}'$  and  $t'$  are the location of the source and the time the source is delivered, respectively,  $p_0$  is the initial pressure response due to the delta heating function.

### ***1.2.3 The photoacoustic wave in the time domain***

Characteristic information of the light-absorbing object is contained within the generated PA wave. The frequency content of the resultant photoacoustic wave from a PA monopole source in one, two, and three dimensions was first considered by Diebold et al. [13,29]. Later, the work was extended to consider objects of greater geometric complexity, such as an isotropic sphere and cylinder [30,31]. Here, the original derivation is used as an instructive tool from which other, more complex shapes, are considered.



If a sphere of radius  $R_S$  and uniform optical absorption,  $\mu_a$ , is illuminated by a short laser pulse, the solution describing the resultant PA wave is found from the general solution to the PA wave equation expressed in Eq. (1.10). The pressure increase inside the sphere is uniform at the initial energy deposition. The solution indicates that two equal pressure waves are generated that propagate as spherical waves originating from the surface of the sphere. One PA wave travels inward, seen as a converging, negative magnitude, spherical pressure wave (rarefaction). The other PA wave travels outward, seen as a diverging, positive magnitude, spherical pressure wave (compression). From a 1D perspective, the positive compression is first observed, followed by the negative rarefaction. The resultant profile is commonly described as a bipolar wave, or an n-shaped wave, observed following the delta heating of a PA source.

The pressure profile measured as a function of time at a point,  $\mathbf{r}$ , will have a bipolar shape that contains maximum amplitude of  $p_0 R_S / \mathbf{r}$ , and width equal to twice the quotient of  $R_S / v_s$ . This is shown in a representative illustration, Fig 1.1.

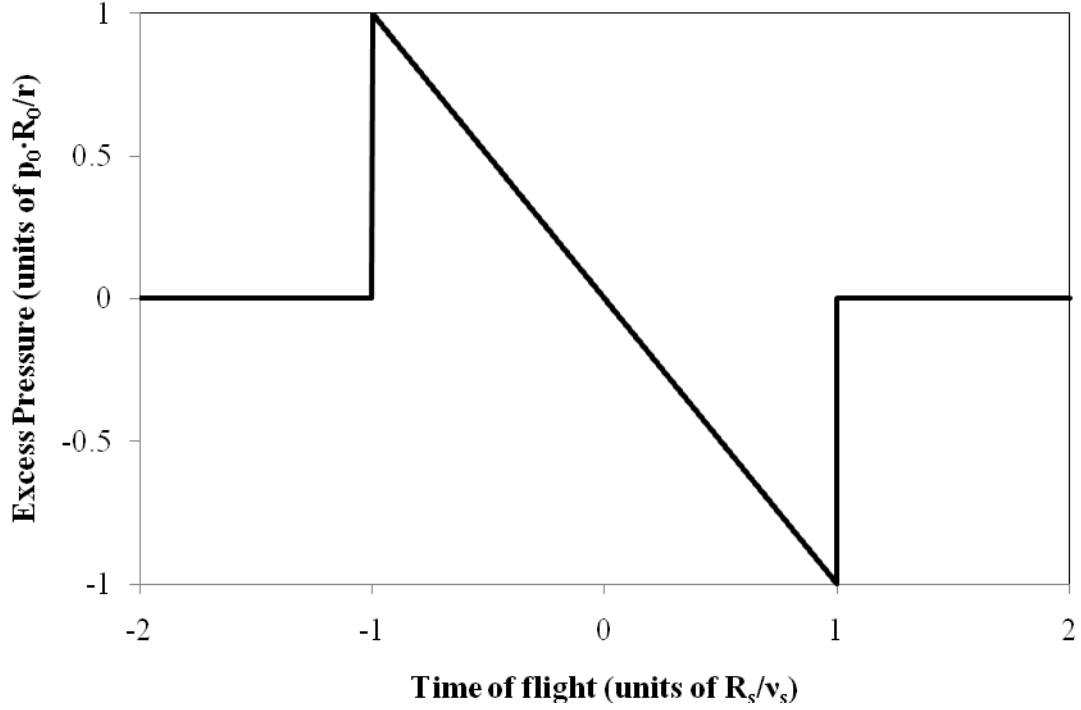


**Figure 1.1:** Pressure profile representing the resultant PA wave in the time domain for a spherical source of radius  $R_s$ . Representative of the solution to the forward model.

The temporal profile of the PA wave can be expressed mathematically, as follows:

$$p(\tau) = \frac{\Gamma \mu_a F}{2r} \begin{cases} -v_s \tau, & |v_s \tau| \leq R_s \\ 0, & |v_s \tau| > R_s \end{cases} \quad (1.11)$$

where  $\tau = t - r/v_s$  is the time of flight of the PA wave. Therefore, three important characteristic features can be derived from the n-shaped wave produced from a PA source. The arrival time of the PA wave, relative to the laser energy incident on the PA source, indicates the distance from the centre of the object to the transducer. The time difference between the abrupt edges of the n-shaped wave, related by the speed of sound in the propagating medium, indicates the width of the sphere. The amplitude of the PA wave provides information about the optical absorption of the PA source and incident laser fluence. Of course, the amplitude of the PA wave provides intrinsically coupled information because it is generated by more than one variable term during a PA experiment. Specifically, it is a function of the laser energy delivered to the PA source, the magnitude of the Grueneisen coefficient, and the optical absorption of the PA source.

Therefore, significant work has been directed towards modeling the light delivery to a PA source, as this is the crucial factor in developing quantitative PA imaging [32-38].

For purposes related to image reconstruction (discussed in later sections), it can be useful to adopt a definition for the pressure profile in terms of the velocity potential (VP), which is proportional to the integral of the pressure profile. This is useful when modeling the backward solution to the reconstruction problem because the profile maintains all the characteristic information of the PA source but is represented as a non-negative function. A strictly positive function serves to eliminate any interference effects when localizing PA signal in voxels during the backward model of the reconstruction process. This correlates with a physical interpretation of the generation of the PA wave, as it is the width of the entire pulse that indicates the dimensions of the object. The velocity potential of the bipolar shape illustrated in Fig. 1.1 is a parabola (shown in Fig. 1.2).

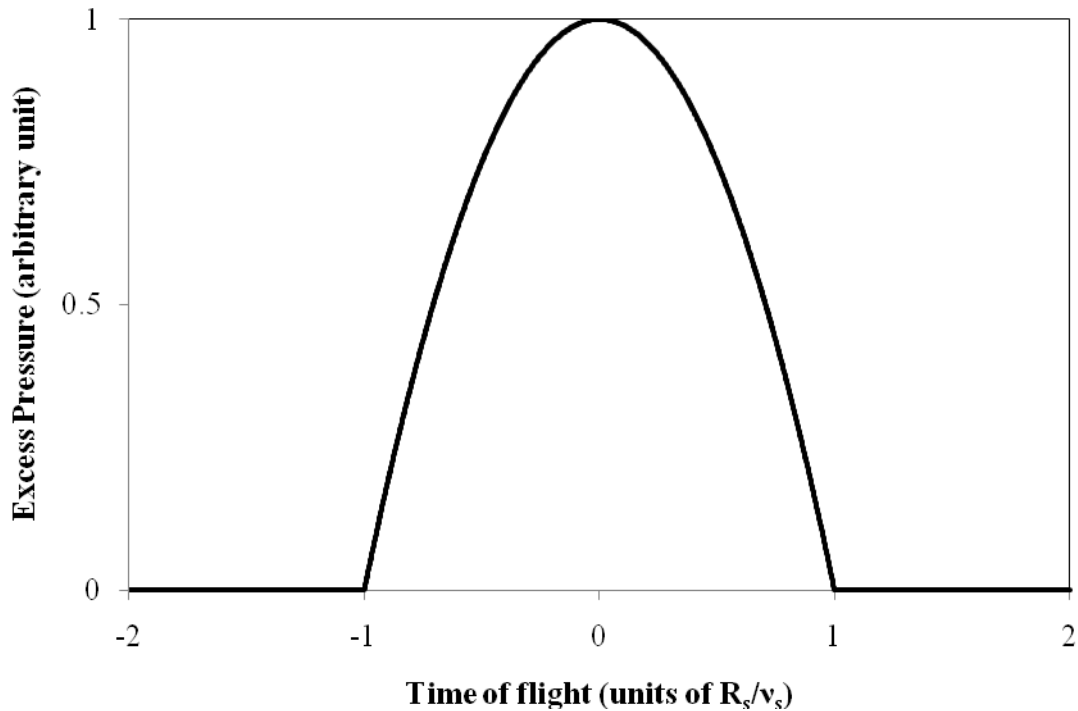


**Figure 1.2:** Velocity potential profile representing the resultant PA wave in the time domain for a spherical source of radius  $R_s$ . Representative of the solution to the backward model.

Mathematically, this function is represented by the following equation:

$$VP(\tau) = \frac{\Gamma \mu_a F}{4r} \begin{cases} -v_s(1 - \tau^2), & |v_s \tau| \leq R_s \\ 0, & |v_s \tau| > R_s \end{cases} \quad (1.12)$$

where Eq. (1.12) represents the integrated function of the bipolar wave described in Eq. (1.11).

### 1.2.4 The photoacoustic wave in the frequency domain

The bipolar pressure wave generated by a PA source has also been considered in the frequency domain [39]. Useful characteristics of the PA source can be extracted by analyzing the wave in the frequency domain. Because the bipolar wave possesses abrupt edges, a broad band of harmonics is associated with the wave when represented in the frequency domain. The amplitude spectrum is represented in Eq. (1.13):

$$p(\omega) = \frac{\left(\frac{\omega a}{c_0}\right) \cos\left(\frac{\omega a}{c_0}\right) - \sin\left(\frac{\omega a}{c_0}\right)}{\left(\frac{\omega a}{c_0}\right)^2} \quad (1.13)$$

Where  $\omega$  is the frequency,  $a$  is the object dimension, and  $c_0$  is the speed of sound. An illustrative example is shown in Fig. 1.3, for PA sources of diameter 1 and 2 mm.

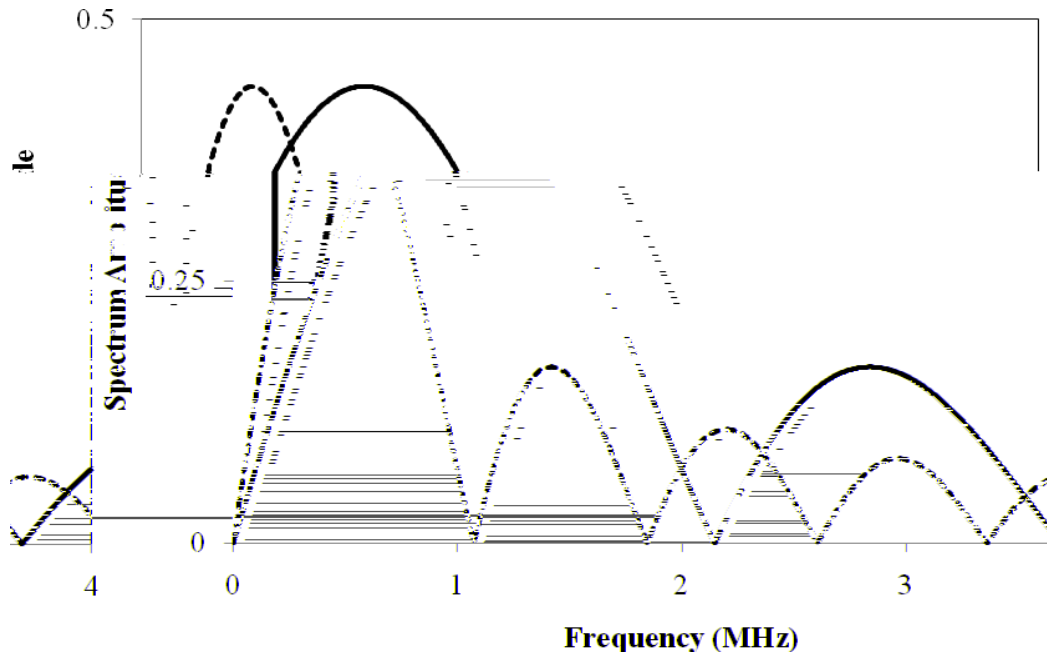


**Figure 1.3:** Spectrum amplitude of acoustic frequencies for spherical sources of varying dimension. Frequency content illustrated for PA sources of 1 mm diameter (solid) and 2mm diameter (dashed).

It is important to observe that the maximum value of the ultrasonic frequency increases with decreasing PA source dimension. Consequently, transducers of increasing bandwidth must be used to accurately measure the ultrasonic waves of decreasing dimension. In a practical situation, the detection of the front pulse is considered accurate when the rise-time of the front equals 0.3 of the entire pulse duration [39]. The upper limit of the frequency detection range is expressed as:

$$f_{max} = \frac{1.5c_0}{a} \quad (1.14)$$

In the case of the 1 and 2 mm PA sources represented in Fig. 1.3, the maximum transducer bandwidth required are 4.5 and 2.25 MHz, respectively. Consequently, detecting objects of many sizes is a technical challenge. A range of PA sources from, for example, 0.5 to 2 mm diameters requires a bandwidth range (based on the maximum frequency of the PA source) of 2.25 to 9 MHz, according to Eq. (1.14).

### ***1.2.5 Photoacoustic image reconstruction***

Many techniques have been developed to accurately reconstruct a PA image based on the data collected from a variety of transducer arrangements and detection schemes. While there are differences in each of the techniques, in a general sense, the goal of any reconstruction algorithm is to create a map of the initial pressure distribution,  $p_0(\mathbf{r}')$ , in a defined object space. Of course, the general solution will not differentiate between the particular heating function applied to the PA sources, and therefore, the absorption coefficient associated with each voxel in the object space remains unknown. As mentioned earlier, a significant effort has been directed towards quantifying the distribution of laser energy in the object space so that derivation of the localized absorption coefficients is possible [32-36].

The general PA image reconstruction solution is centered on localizing the voxel from which each of the surface measurements originated [40,41]. When a PA wave is detected, the distance the wave has traveled can be measured by recording the time of

flight difference between the initial laser pulse and the centre of the detected bipolar wave. The process of positioning the time domain surface measurements back into an enclosed object space is called the backward model. In 3D, with the distance of the PA source to transducer known, the surface measurement is projected onto a spherical arc with the centre of the sphere being the point of PA wave measurement and radius equaling the distance the PA wave traveled before detection. A simple example of the backward model in 2D is shown in Fig. 1.4.

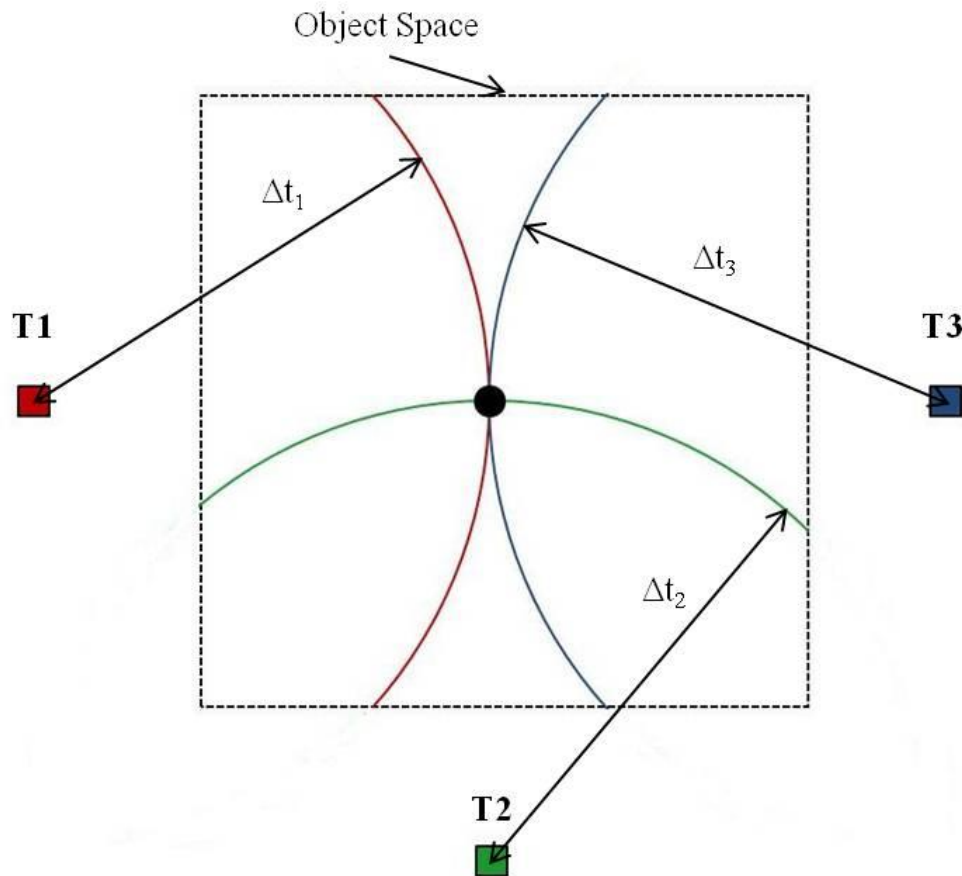


**Figure 1.4:** 2D illustration of the backprojection principle. PA source located at the intersection of the arcs produced by each of the 3 transducers (T1, T2, T3), determined by the associated time of flight from PA source to transducer.

Each of the transducers produces a circular shell based on the time of flight of the PA wave. Provided the speed of sound in the object space is homogeneous, the arcs overlap at a common point, indicating the location of the PA source. In this case, streaking artifacts in the image would be  $1/3^{\text{rd}}$  the intensity of the PA source. Of course,

increasing the number of surface measurements serves to increase the contrast between the PA source and residual artifacts as the consequence of the backprojected arcs is lessened.

In experimental imaging systems, the measurement surface never entirely encloses the pressure volume; a consequence known as limited-view imaging. Many reconstruction algorithms have considered this inevitability and great effort has been placed in understanding the consequence of measuring the PA wave with only a limited-view [42-49]. In order to compensate for limited-view artifacts, an iterative reconstruction approach was proposed by Paltauf et al. [50]. In this approach, the error between the measured surface measurements and estimated surface measurements is minimized by alternating between the forward and backward model, while subtracting the residual error from the master image. The foundation of this algorithm was used to produce images in our group's earlier work [51-53]. Other forms of backprojection techniques are employed by using the planar approximation of the Radon transform to localize the pressure signals [54]. Here, the second spatial derivative of each projection is computed and then backprojected such that an approximation of the absorption properties of the object can be estimated. Backprojection is also performed in the frequency domain where the solution to the wave equation is expressed in frequency components [55-57]. In this method, computation efficiency is significantly improved by use of the fast-Fourier-transform algorithm (FFT), which can improve reconstruction times of up to two orders of magnitude compared with the standard backprojection technique [58].

The delay-and-sum technique was originally developed for traditional ultrasonography but has been applied in the reconstruction of PA images as well [14,19,59]. In this technique, interference effects are taken advantage of such that the net sensitivity of the transducer array is focused to a field point. This is achieved by algorithmically applying a time-delay to each transducer's signal based on the transit time between the field point and the transducer surface. Signals are then windowed around a delay that corresponds to the transit time to a particular voxel.

Many other methods for image reconstruction have been considered. Finite element solutions have been employed to solve the wave equation [60-62], far-field approximations [63,64], compressed sensing [65,66], and variations of SVD-based algorithms [67].

The technique we chose to utilize for image reconstruction (discussed in section 1.6) was made for a number of practical reasons. Implementing standard backprojection algorithms requires the position of the transducers be known precisely. The PA system used throughout this work uses transducers that are relatively large and, consequently, any estimate of the transducer position becomes problematic. Other reconstruction techniques, such as beamforming require the transducers be focused to receive acoustic waves from only a specified field-point in the imaging volume. In our system, directionally sensitive transducers are used to acquire all the PA information from a single laser pulse, making beamforming an impractical decision for our system. Of course, other reconstruction techniques are available. In general, we selected the imaging matrix approach because it employed the use of the experimentally measured response of our system.

## **1.3 Photoacoustic Imaging Approaches**

### ***1.3.1 2D photoacoustic imaging approaches***

A variety of different approaches have been developed in order to produce PA images. Here, the approaches are broadly summarized to provide context and motivation for our approach to producing 3D PA images.

A 2D photoacoustic tomography (PAT) system is widely used because it is a relatively simple and inexpensive way to produce comparatively high resolution PA images. The system employs the use of a single transducer that is mechanically scanned around the perimeter of the sample. At each transducer location, the PA wave is recorded



and, after scanning, the universal backprojection algorithm is used to reconstruct a 2D image. This system has been used to successfully visualize light-absorbing objects, including vasculature in the mouse brain [21], peripheral joints in humans [68], measure fluorescent agents [23], characterize hypoxia in mouse brain [69], monitor angiogenic vascular growth in mouse [70], and many others. Because this system only uses a single transducer and single acquisition channel, it is relatively inexpensive and simple to construct. However, the system suffers from relatively long data acquisition times due to the mechanical scanning of a single transducer. As well, images are localized to the selected plane and, therefore, translation to 3D images is not possible without scanning the object or transducer to produce images of multiple 2D planes.

Another design, called light-induced optoacoustic imaging system (LOIS) was developed by Oraevsky et al., in order to image and diagnose breast tumors [28]. In various generations, the system utilizes a curved array of transducers with 32, 64, or 128 channels. The array is designed with very high focus in the selected imaging plane but extremely directional sensitivity elsewhere. Therefore, a slice of the breast can be selected. The sensitivity of the system to detector breast tumors is compared to other imaging modalities, where it was recently shown to have higher sensitivity than x-ray mammography but lower than ultrasound. The system can display images at relatively high frame rate (1-10 Hz) but suffers from high cost associated with the transducer count and data acquisition channels utilized. Of course, this system is also limited to producing only 2D images.

In 2008, Zemp et al., introduced a high frequency photoacoustic microscopy (PAM) system capable of producing 2D images in real-time [71]. The system consists of a high-repetition rate laser and an ultrasound array with peak detection at 30 MHz. The entire imaging process, from data acquisition to image display, is produced at 50 fps. The system has been used to image a variety of phantoms as well as *in vivo* absorbing structures at depths around 3 mm.

### ***1.3.2 3D photoacoustic imaging approaches***

Photoacoustic microscopy utilizes a highly focused, high frequency transducer that is scanned across the sample. Because the transducer is highly focused, each PA measurement recorded is well localized. 3D images are then rendered by stacking the PA line scans that are garnered from sequential scanning. This technique produces high resolution images at depths much greater than conventional microscopy. PAM has been used broadly for a variety of applications to produce 3D PA images. Examples include imaging skin melanoma [72], vasculature features [73-76], skin burns [77], and has been recently integrated with OCT to do simultaneous multimodal imaging [78].

An etalon scanner was developed by Beard et al., to produce 3D PA images. In this scheme, a thin film acts as a Fabry-Perot etalon [79-81]. The acoustic pressure causes slight changes in the film thickness and can be probed by a laser to quantify these changes. This approach acquires the pressure measurements in a 2D plane, which are then reconstructed into a 3D volume using a Fourier transform algorithm. This detection scheme produces images of relatively high resolution and contrast but suffers from limited penetration depth and slow image acquisition times.

Carson et al., implemented a system similar to the PAT system developed by Wang. That is, a single transducer is stepped around the object within a single plane. By applying the universal backprojection algorithm, tomographic images are produced. In order to generate 3D images, the PA signals must be collected along the surface of a sphere. This concept was applied by scanning the transducer along an arc in which a relatively large solid angle was covered. This was utilized to successfully image animal joints with resolution of a few hundred micrometers [82].

Kruger et al., developed a method using a hemispherical array of transducers with a directional sensitivity overlapping at the centre of the hemisphere but using thermoacoustic principles [54]. This method employs the use of a radio frequency (RF) antenna, emitting waves at 434 MHz directed towards the centre of the hemisphere. The

hemisphere is rotated, and at each position, the RF pulse is absorbed by the PA source where the transducers can sample the PA wave. Once data is acquired over 360°, a Radon transform reconstruction algorithm is utilized to produce 3D images. While the implementation and detection scheme is similar to the realization employed in our system, a significant difference is the mechanical scanning utilized by Kruger et al. to acquire data, greatly increasing the time required to produce a single 3D image.

Paltauf et al., has done significant research producing PA images using integrating line transducers. This has been used to generate 2D images and, with modifications to the reconstruction technique, has produced 3D images as well. These transducers are organized such that they satisfy the 2D wave equation and, therefore, measured data can be used to produce images by temporal backprojection algorithms. This technique has been used to represent a variety of phantom objects [63,83].

A group based out of the University of Twente has integrated a light delivery system with a disc-shaped piezoelectric transducer. The optical fibers are situated at the side of the transducer where reflection mode imaging is used. In this particular realization, weighted delay-and-sum reconstruction was used to produce 3D maximum intensity projection images of the PA source distribution. This was first used to image neovascularization in tumour angiogenesis in rats [84].

Earlier work developed by our group utilized the same detection scheme as is described in Chapter 2 [51,53]. Data are acquired on 15 channels simultaneously, where image reconstruction was performed offline via an iterative reconstruction algorithm. This system has been used to perform fast 3D data acquisition (DAQ) at the repetition rate of the laser pulse (10 Hz) [51], as well as localization of spherical lesions embedded in tissue mimicking phantoms up to approximately 2 cm [53]. This scheme collects 3D image data at rates limited only by laser repetition with relatively good image depth. However, the system suffers from lengthy reconstruction times because an iterative reconstruction technique is used. Reconstruction technique combined with relatively low transducer count has contributed to relatively poor image quality as well.

### ***1.3.3 Photoacoustic imaging in real-time***

As mentioned as a general theme throughout Chapter 1 is the notion that taking advantage of the potential high temporal resolution is of paramount importance when utilizing a system with a sparse detection scheme. Real-time imaging is vital in viewing dynamic processes. Mentioned earlier, Zemp et al. produced real-time 2D images of cardiovascular dynamics in a mouse at 50 fps by using a beam-forming technique and a 48-channel array [71,85]. Niederhauser et al. also demonstrated real-time imaging at 7.5 fps of human vasculature in a 64-channel array [86]. Most recently, Gamelin et al. produced a 512-element curved transducer array (parallel channel acquisition) to produce tomographic images of small animals at 8 fps [87]. Other PA analysis has been done in real-time, including real-time flow cytometry [88]. However, the extension to real-time 3D images is not trivial as the 2D real-time techniques would require scanning the transducer array to transition to the 3D regime.

A 3D real-time technique was developed by Song et al. [89], producing 3D PA images of mouse vasculature at 3 seconds per frame. The system scanned the transducer array over the mouse skin while employing a laser with 1 kHz repetition rate. 996 laser pulses were used to produce a single 3D image. While this was a significant technological advancement, multiple laser shots were utilized to produce a single 3D image, diminishing the effective temporal resolution of the system. Ideally, a system would utilize a single laser pulse to produce a 3D PA image such that each 3D frame represents a snap-shot of the PA source over the interval of the lasers pulse duration (~5-10 ns).

## **1.4 Photoacoustic System Characterization**

As described in previous sections, various detection schemes and light delivery systems have been realized in an experimental setting. However, in a few of these schemes, a very limited number of transducers are utilized to capture time domain

measurements. While these approaches generally possess a relatively high temporal resolution, they suffer from spatially-dependent sensitivity to PA sources in the object space. Since there are relatively few transducers recording surface measurements, the effect can be significant for objects located at the periphery of the object space. This is largely because the frequency response and sensitivity of the transducers vary as a function of the angle the PA source is located from the normal vector to the transducer face. Furthermore, the interaction of the PA wave with transducers of finite dimension causes the width of the PA wave to broaden and can create subtle ambiguities in the arrival time of the PA waves. Here, motivation for this work is discussed in order to provide context for the work in Chapter 2.

### ***1.4.1 System characterization approaches***

In 2003, Kruger et al. [90] characterized a linear array by translating a point-like source across the face of the array and measuring the axial response. The characterization technique allowed the experimental estimate of the system's lateral resolution in a plane of specified distance from the transducer array. Later, the work was extended to estimate the effective field-of-view (FOV) of the PA imaging system [91]. Here, a bilinear array of dots was fabricated on transparent film and imaged. The intensities of the dots were computed as a function of distance from the centre of the object space. The point in which the dot intensity decreased to below half-power provided an estimate of the effective lateral FOV. The major limitation in each of the previous works is the inability to translate the point-like object to a 3D characterization setting. As well, the work by Kruger et al. did not demonstrate the PA wave produced by the point-like source truly emitted a uniform PA wave in the relevant dimensions. However, the encouraging results did serve to validate the assumption of PA wave uniformity.

A second approach was taken by Yang et al. [92] to use virtual point detectors to circumvent the shift-variant response of the object space. Using virtual point detectors provides the advantages of a real point detector (high and uniform spatial resolution) without the associated drawbacks (relatively high thermal noise). This is accomplished by

using a ring detector and exploiting geometric considerations based on the arrival time of the PA wave. It is possible to then emulate a PA wave that has been produced by a point detector but without the increase thermal noise associated with small area detectors. In effect, this strategy detects a PA wave in the detection plane equally, regardless of location. While this detection scheme is potentially useful in 2D, it cannot be easily translated to 3D in a practical system. Moreover, this scheme is not sparse, and therefore suffers from similar drawbacks in temporal resolution to densely sampled systems. Particularly, data acquisition and image reconstruction times are on the order of those densely sampled systems.

In earlier work performed by our group, a ring array of transducers was characterized by coating a 400  $\mu\text{m}$  core optical fibre with a black coating [52]. The fibre was raster scanned through the object space. At each point, a laser was pulsed and directed into the fibre. Each pulse generated a PA wave at the tip of the fibre, where the pressure measurement could be made by each transducer in the ring array. The measured sensitivity recorded for each transducer was then used in the iterative reconstruction algorithm as a weighting factor to correct for non-uniform detection in the object space. While this point source worked well with a detection scheme arranged in a single plane, it does not translate to the hemispherical array used in our later work.

## **1.5 Photoacoustic System Analysis**

It is the aim of any photoacoustic image reconstruction to accurately determine the position and magnitude of the optical absorber for each voxel in a specified object space. However, image reconstruction techniques have their own advantages and disadvantages beyond what is dictated by inherent system properties. In a system utilizing limited projections to acquire PA wave measurements, it is crucial to understand the constraints of the system based on the detection scheme (independent of the chosen reconstruction technique). Here, general concepts are introduced that are used in the characterization of the PA imaging system.

### ***1.5.1 The linear system model and the imaging operator***

It is common in imaging science to consider image formation as a mapping process from one measurement space to another. In PA imaging, the mapping utilizes time-domain pressure measurements to produce an estimate of the voxel coefficients which produced the PA wave. A linear model is typically used to describe an imaging system to the first order. Fortunately, this is typically quite accurate as most transducers respond linearly in the range selected for PA wave measurement. The approach has been implemented by other imaging modalities and serves as the model used in this thesis for photoacoustic image reconstruction. Mathematically, the linear model for a noiseless system is expressed as:

$$\mathbf{g} = \mathbf{H}\mathbf{f} \quad (1.15)$$

where  $\mathbf{g}$  is a vector that represents the measured data set,  $\mathbf{H}$  is a continuous-to-discrete imaging operator, and  $\mathbf{f}$  is a vector that represents a finite-dimensional approximation of the unknown object(s) that produced the data in  $\mathbf{g}$ . To perform image reconstruction, the vector  $\mathbf{f}$  is estimated directly by solving this linear equation.

To produce an experimental estimate of the imaging operator,  $\mathbf{H}$ , it is required that the system response to a PA source be measured. That is, a PA source should be localized to each voxel in the object space, where each transducer's response to the PA source can be recorded by a DAQ system. It follows that the content of each row of the imaging operator corresponds to the concatenated time series that each transducer recorded at a particular voxel. Intuitively, this is a sensible approach to mapping a measured data set to an estimate of the object because any experimentally measured data set must be a linear combination of PA waves measured in the imaging operator. This is valid provided all PA waves originate from within the enclosed object space. The goal is then to determine the voxel coefficients that produced the measured data set. Essentially, the optical properties of each voxel in the object space that produced the data set.

### 1.5.2 The crosstalk matrix

For all practical PA imaging systems, there is intrinsic spatially-dependent sensitivity in the object space. This is a result of real, finite-dimension transducers measuring the PA wave. As well, the temporal signature associated with each voxel in the object space is not necessarily unique from other voxels. This is most intuitive by recalling the backprojection principle illustrated in Fig. 1.4. Any single transducer can only distinguish between voxels that possess different temporal signatures as determined by the radius of the backprojected arc. Therefore, regardless of the merits of the reconstruction method, the signal produced by a PA source in these temporal regions can never be distinguished. This effect is a form of aliasing (though not determined by undersampling in time, as is the conventional definition).

The crosstalk matrix, introduced by Barrett et al. [93], is a technique that utilizes the imaging operator to broadly quantify spatially dependent system sensitivity and aliasing features. Originally, the technique was used to recover Fourier coefficients used to describe an object in the frequency domain. Since, it has been extended to recover expansion coefficients in the spatial domain as well as wavelet coefficients [94]. In this thesis, the discussion is limited to the spatial domain since it is these expansion functions that are experimentally measured by our imaging system.

Any object can be approximately represented by a series of expansion functions in the spatial domain. In our imaging system, the object is represented by cubic voxels. The measured data,  $\mathbf{g}$ , and the voxel coefficients in  $\mathbf{f}$  are related by the imaging operator,  $\mathbf{H}$ . The crosstalk matrix explicitly quantifies the relative magnitude of each voxel coefficient as it contributes to the object space:

$$\mathbf{B} = \mathbf{H}^T \mathbf{H} \quad (1.16)$$

with each element in  $\mathbf{B}$  defined as:

$$B_{jj'} = \sum_{k=1}^K (\mathbf{H}_{jk}^T \mathbf{H}_{j'k}) \quad (1.17)$$



where  $\mathbf{H}^T$  represents the transpose of  $\mathbf{H}$ ,  $j$  and  $j'$  represent the index of the first and second voxel coefficient,  $k$  denotes the product of the time index for a given transducer and the index of the transducer, and  $K$  denotes the product of the total number of indices and the total number of transducers.

The crosstalk matrix is an important tool in describing two metrics related to system performance. The first, by examining the main diagonal of the matrix, the cumulative system sensitivity is explicitly indicated. Each entry in the main diagonal of the matrix is computed by multiplying the time series associated with a particular voxel in the imaging operator with itself. Consequently, a scalar value is retrieved indicating the sum of the photoacoustic signal magnitude associated with a particular voxel.

Second, by examining the rows of the crosstalk matrix, a type of aliasing is quantified. When computing the crosstalk matrix, each entry in the row is calculated by multiplying the time series for a particular voxel with the time series of another voxel. Qualitatively, this computes the intersection of a particular voxel's time series with any other voxel's time series. For example, entry  $B_{12}$  multiplies the first voxel's time series with the second voxel's time series. The result then yields a scalar value indicating the overlap, or aliased signal, which is indistinguishable among the two time series (and by association, the two voxels).

### ***1.5.3 Singular value decomposition***

The transducer frequency response, number of transducers recording PA wave measurements, and the measurement space sampling rate are vital in determining the complexity of objects that can be recovered by an imaging system. These parameters defining the detection scheme describe the object space in which PA measurements are recorded.

As described in earlier sections, image reconstruction is an inverse problem where the objective is to recover one or more objects from a measured data set. It is the imaging

operator that fundamentally describes the relationship between an object and the time-dependent pressure measurements detected by the set of transducers. Analysis of the imaging operator,  $\mathbf{H}$ , by singular value decomposition (SVD) can be performed to generate detailed system information indicating, broadly, the complexity of objects that can be represented by the imaging system, irrespective of the merits of the reconstruction technique. SVD also provides the sensitivity of an imaging system to an object composed of one or more singular vectors in the object space.

In experimental imaging operators, it is generally found that  $\mathbf{H}$  is singular and cannot be inverted directly. However, for singular matrices, it can be shown that an  $M \times N$  matrix can be decomposed into three component matrices by SVD, which is described as:

$$\mathbf{H} = \mathbf{U}\mathbf{S}\mathbf{V}^T \quad (1.18)$$

where  $\mathbf{U}$  is an  $M \times M$  matrix,  $\mathbf{V}$  is an  $N \times N$  matrix, and both are nonsingular. The  $M \times N$  matrix,  $\mathbf{S}$ , is a diagonal matrix with entries listed in descending order, representing the singular values of the imaging operator. The rows of  $\mathbf{U}$  and columns of  $\mathbf{V}^T$  are both orthonormal singular vectors that completely describe the measurement space and object space, respectively. The decomposition is performed by solving the generalized singular value problem for the imaging operator,  $\mathbf{H}$ .

For an experimental imaging operator, it is generally possible to find a vector,  $\boldsymbol{\psi}$ , such that  $\mathbf{H}\boldsymbol{\psi}$  is the same as  $\boldsymbol{\psi}$ , changed only by a multiplicative constant. These vectors are called the eigenvectors of  $\mathbf{H}$ . These vectors satisfy the generalized eigenvalue equation:

$$\mathbf{H}\boldsymbol{\psi} = \lambda\boldsymbol{\psi} \quad (1.19)$$

It can be shown that the non-zero eigenvalues belonging to  $\mathbf{U}$  and  $\mathbf{V}^T$  are identical. In order to find these eigenvalues, the characteristic equation of the imaging operator is solved:

$$(\mathbf{H} - \lambda\mathbf{I})\boldsymbol{\psi} = \mathbf{0} \quad (1.20)$$

where  $\mathbf{I}$  is the identity matrix. Once the singular values are computed, singular vectors associated with each orthonormal matrix,  $\mathbf{U}$  and  $\mathbf{V}^T$ , can be computed by substituting the singular value into the generalized eigenvalue equation and reducing the set of equations.

Typically, it is the singular vectors of the matrix  $\mathbf{V}^T$  that are of interest because they describe the imaging system's object space. That is, any object that can be represented by the imaging system must be made of a linear combination of the vectors in  $\mathbf{V}^T$ . However, not all the vectors in each matrix  $\mathbf{U}$  and  $\mathbf{V}^T$  contribute to image reconstruction. At a threshold in the matrix  $\mathbf{S}$ , the singular values will become zero-valued, indicating the associated singular vectors are in the null space of the imaging system. Experimentally, the values never become precisely zero, but approach values exceedingly small and are considered effectively zero. Therefore, it is crucial to identify the number of singular vectors that contribute usefully to the retrieval of an object when an imaging task is performed.

## **1.6 Imaging Tasks and Singular Value Decomposition**

From the developments in Chapter 2 and 3, our reconstruction technique was modified to solve the linear system introduced in Eq. (1.15). Here, details of this technique are described.

### ***1.6.1 Pseudoinverse of the imaging operator***

Any experimental imaging operator is found to be singular and, consequently, the inverse of the imaging operator does not exist. Therefore, in order to perform image reconstruction by solving the linear system model, the pseudoinverse of the imaging operator must be computed. It should be noted that to perform image reconstruction in

this thesis, the component matrices computed from SVD analysis are used when solving the linear system model. Therefore, the solution to the equation is described by:

$$\mathbf{f} = \mathbf{H}^{-1}\mathbf{g} = (\mathbf{U}^T\mathbf{S}^+\mathbf{V})\mathbf{g} \quad (1.21)$$

where  $\mathbf{S}^+$  is the pseudoinverse of the diagonal matrix,  $\mathbf{S}$ . Because the matrix,  $\mathbf{H}$ , in the above equation is measured experimentally, simple matrix multiplication can be done to produce an estimate of the object vector,  $\mathbf{f}$ .

Computational problems can arise when the dimensions of the imaging operator become large as the complexity of the SVD scales as  $O\{N^3\}$ . It should be noted, however, that the SVD is computed for the imaging operator prior to any imaging experiment. While these computation times can be lengthy, they do not impact the reconstruction time. It is possible memory requirements prohibit the SVD of a large imaging operator. However, this is merely a technological limitation rather than a fundamental problem with the reconstruction approach used throughout this work. The increase in SVD time did not correlate precisely to a rise in the cube of the matrix dimension in practice. It was not tested systematically, but was perceived as a limit when considering reasonable decomposition times. The discrepancy could be in part attributed to the number of zero entries in the imaging operator, which varied significantly depending on imaging operator construction parameters.

### ***1.6.2 Regularization of the imaging operator***

When performing the pseudoinverse computation on the matrix  $\mathbf{S}$ , the inverse of the zero-valued singular values become exceedingly large and dominate the singular values that are associated with lower order singular vectors. In all cases of our image reconstruction, these values are simply forced to zero in order to remove any impact of null space singular vectors on image reconstruction. Because some of the remaining singular vectors are comprised entirely of noise, it has become an empirical exercise in determining which of the lower order singular vectors should be regularized. This has been performed in other imaging modalities in which the linear model was used to

perform image reconstruction [95]. For the work in Chapter 4, image reconstruction for simulated objects was performed by regularizing any singular value associated with an index greater than 90% of the matrix rank index. Image reconstruction for experimental objects was performed by regularizing any singular value associated with an index greater than 20% of the matrix rank index.

## 1.7 Motivation and Objectives

Based on the review of literature in previous sections, a method to produce real-time 3D PA images could drastically influence the landscape of PA imaging applications. The entirety of this work describes our approach to design a 3D PA imaging system. This work outlines the calibration and characterization of a 3D PA imaging system with a sparse, staring detection scheme through three separate, but related, projects. The early work sought to calibrate the shift-variant system response, which was deemed imperative to produce PA images via a system utilizing a relatively limited number of transducers. From here, more advanced characterization was explored by employing the use of the crosstalk matrix and singular value decomposition technique. The techniques were used in order to quantify system performance with regards to spatially-dependent object space sensitivity as well as the objects that could be represented by our imaging system. The SVD results were later extended and provided the foundation for image reconstruction by directly solving for an estimate of the PA sources using a linear system model. This reconstruction technique, coupled with technological system improvements (both hardware and software), provided the basis to produce real-time 3D PA images.

The focus of Chapter 2 is aimed towards the calibration and characterization of the object space for our PA imaging system. The chapter discusses the synthesis of a point-like source in 3D and subsequently utilizes the PA source to characterize the object space by the transducer sensitivity, source broadening, and time-of-flight.

The work in Chapter 3 introduces a technique to experimentally measure the imaging operator for a PA system. From that foundation, two techniques are computed to quantify the PA system performance: the crosstalk matrix and singular value decomposition.

In Chapter 4, the SVD results are explored for imaging operators composed of different transducer counts and measurement space sampling rates. A mathematical criterion is introduced in Chapter 4 in which the matrix rank of an imaging operator can be determined explicitly. Quantifying an imaging operator's associated matrix rank (the number of linearly independent rows) is then applied to reconstruct images. After performing SVD on an experimental imaging operator, the concept was extended to assess the capability of different PA systems to complete an imaging task. Objects included both simulated and experimental point, line, and multi-point simulated objects as well as a point-like experimental object. In a PA system without noise, each of the singular vectors prior to the matrix rank contributes to image reconstruction. However, in an experimental PA system, part of the basis of singular vectors is produced because of the measured noise. It is more difficult to precisely determine the degree to which singular vectors change depending on system noise.

It is understood that this approach to PAI will produce images of relatively poor quality in comparison to other techniques. It should be stressed that the goal of the research was to develop an approach that focused on PAI that was inherently 3D and captured a PA image in a single laser pulse. From here, the work will be extended to increase transducer counts and improve image quality.

## 1.8 References

1. J. C. Hebden, S. R. Arridge, and D. T. Delpy , " Optical imaging in medicine .1. Experimental techniques," *Phys. Med. Biol.* **42**, 825-840 (1997).
2. A. P. Gibson, J. C. Hebden, and S. R. Arridge , " Recent advances in diffuse optical imaging," *Phys. Med. Biol.* **50**, R1-R43 (2005).

3. F. Vasefi, B. Kaminska, G. H. Chapman, and J. J. L. Carson , " Image contrast enhancement in angular domain optical imaging of turbid media," *Optics Express* **16**, 21492-21504 (2008).
4. F. Vasefi, B. Kaminska, P. K. Y. Chan, and G. H. Chapman , " Multi-spectral angular domain optical imaging in biological tissues using diode laser sources," *Optics Express* **16**, 14456-14468 (2008).
5. F. Vasefi, M. Belton, B. Kaminska, G. H. Chapman, and J. J. L. Carson , " Angular domain fluorescence imaging for small animal research," *J. Biomed. Opt.* **15**, 016023 (2010).
6. C. Balas , " Review of biomedical optical imaging-a powerful, non-invasive, non-ionizing technology for improving in vivo diagnosis," *Meas Sci Technol* **20**, 104020 (2009).
7. V. Ntziachristos, J. Ripoll, L. H. V. Wang, and R. Weissleder , " Looking and listening to light: the evolution of whole-body photonic imaging," *Nat. Biotechnol.* **23**, 313-320 (2005).
8. E. E. Graves, R. Weissleder, and V. Ntziachristos , " Fluorescence molecular imaging of small animal tumor models," *Curr. Mol. Med.* **4**, 419-430 (2004).
9. R. K. K. Wang , " Signal degradation by coherence tomography multiple scattering in optical of dense tissue: a Monte Carlo study towards optical clearing of biotissues," *Phys. Med. Biol.* **47**, 2281-2299 (2002).
10. M. Xu and L. V. Wang , " Photoacoustic imaging in biomedicine," *Rev. Sci. Instrum.* **77**, (2006).
11. T. Lu, J. Jiang, Y. Su, R. K. Wang, F. Zhang, and J. Yao, "Photoacoustic imaging: Its current status and future development" in *4th International Conference on Photonics and Imaging in Biology and Medicine, September 03,2005 - September 06* ( SPIE), National Natural Science Foundation of China; SPIE Russia Chapter; Int. Laser Center of M.V. Lomoson Moscow State Univ.; Bio-optics and Laser Medicine Comm. of Chinese Optics Soc.; Science and Techn. Garden of Tianjin University, China.
12. D. Xing and L. Xiang, *Photoacoustic and Thermoacoustic Imaging for Biomedical Applications*, (2008).
13. G. J. Diebold and T. Sun , " Properties of Photoacoustic Waves in One-Dimension, 2-Dimension, and 3-Dimension," *Acustica* **80**, 339-351 (1994).
14. S. Manohar, A. Kharine, J. C. G. van Hespén, W. Steenbergen, and T. G. van Leeuwen , " Photoacoustic mammography laboratory prototype: imaging of breast tissue phantoms," *J. Biomed. Opt.* **9**, 1172-1181 (2004).

15. D. Piras, W. Xia, W. Steenbergen, T. G. van Leeuwen, and S. Manohar , " Photoacoustic Imaging of the Breast Using the Twente Photoacoustic Mammoscope: Present Status and Future Perspectives," *Ieee Journal of Selected Topics in Quantum Electronics* **16**, 730-739 (2010).
16. F. Ye, S. Yang, and D. Xing , " Three-dimensional photoacoustic imaging system in line confocal mode for breast cancer detection," *Appl. Phys. Lett.* **97**, 213702 (2010).
17. T. Bowen , " Radiation-Induced Thermoacoustic Soft-Tissue Imaging," *Ieee Transactions on Sonics and Ultrasonics* **29**, 187-187 (1982).
18. C. G. A. Hoelen, F. F. M. de Mul, R. Pongers, and A. Dekker , " Three-dimensional photoacoustic imaging of blood vessels in tissue," *Opt. Lett.* **23**, 648-650 (1998).
19. C. G. A. Hoelen and De Mul, Frits F. M. , " Image reconstruction for photoacoustic scanning of tissue structures," *Appl. Opt.* **39**, 5872-5883 (2000).
20. R. Esenaliev, I. Larina, K. Larin, M. Motamedi, A. Karabutov, and A. Oraevsky , " Laser optoacoustic technique for real-time measurement of thermal damage in tissues," *Thermal Treatment of Tissue with Image Guidance, Proceedings of* **3594**, 98-109 (1999).
21. X. D. Wang, Y. J. Pang, G. Ku, G. Stoica, and L. H. V. Wang , " Three-dimensional laser-induced photoacoustic tomography of mouse brain with the skin and skull intact," *Opt. Lett.* **28**, 1739-1741 (2003).
22. K. H. Song, G. Stoica, and L. V. Wang , " In vivo three-dimensional photoacoustic tomography of a whole mouse head," *Opt. Lett.* **31**, 2453-2455 (2006).
23. D. Razansky, C. Vinegoni, and V. Ntziachristos , " Multispectral photoacoustic imaging of fluorochromes in small animals," *Opt. Lett.* **32**, 2891-2893 (2007).
24. Y. W. Wang, X. Y. Xie, X. D. Wang, G. Ku, K. L. Gill, D. P. O'Neal, G. Stoica, and L. V. Wang , " Photoacoustic tomography of a nanoshell contrast agent in the in vivo rat brain," *Nano Letters* **4**, 1689-1692 (2004).
25. X. Yang and L. V. Wang , " Photoacoustic tomography of a rat cerebral cortex with a ring-based ultrasonic virtual point detector," *J. Biomed. Opt.* **12**, (2007).
26. R. G. M. Kolkman, W. Steenbergen, and T. G. van Leeuwen , " In vivo photoacoustic imaging of blood vessels with a pulsed laser diode," *Lasers in Medical Science* **21**, 134-139 (2006).
27. J. C. Chato , " A Survey of Thermal Conductivity and Diffusivity Data on Biological Materials," *Mech. Eng.* **89**, 59-& (1967).



28. S. A. Ermilov, T. Khamapirad, A. Conjusteau, M. H. Leonard, R. Lacewell, K. Mehta, T. Miller, and A. A. Oraevsky , " Laser optoacoustic imaging system for detection of breast cancer," *J. Biomed. Opt.* **14**, 024007 (2009).
29. G. J. Diebold, T. Sun, and M. I. Khan , " Photoacoustic monopole radiation in one, two, and three dimensions," *Phys. Rev. Lett.* **67**, 3384-3387 (1991).
30. M. I. Khan and G. J. Diebold , " The photoacoustic effect generated by laser irradiation of an isotropic solid cylinder," *Ultrasonics* **34**, 19-24 (1996).
31. M. I. Khan and G. J. Diebold , " The Photoacoustic Effect Generated by an Isotropic Solid Sphere," *Ultrasonics* **33**, 265-269 (1995).
32. B. T. Cox, S. R. Arridge, and P. C. Beard , " Gradient-based quantitative photoacoustic image reconstruction for molecular imaging - art. no. 64371T," *Photons Plus Ultrasound: Imaging and Sensing 2007* **6437**, T4371-T4371 (2007).
33. B. T. Cox, S. R. Arridge, and P. C. Beard , " Quantitative photoacoustic image reconstruction for molecular imaging - art. no. 60861M," *Photons Plus Ultrasound: Imaging and Sensing 2006* **6086**, M861-M861 (2006).
34. B. T. Cox, S. R. Arridge, K. P. Kostli, and P. C. Beard , " Two-dimensional quantitative photoacoustic image reconstruction of absorption distributions in scattering media by use of a simple iterative method," *Appl. Opt.* **45**, 1866-1875 (2006).
35. B. T. Cox, S. R. Arridge, K. P. Kostli, and P. C. Beard , " Quantitative photoacoustic imaging: fitting a model of light transport to the initial pressure distribution," *Photons Plus Ultrasound: Imaging and Sensing 2005* **5697**, 49-55 (2005).
36. B. T. Cox, J. G. Laufer, and P. C. Beard , " The challenges for quantitative photoacoustic imaging," *Photons Plus Ultrasound: Imaging and Sensing 2009* **7177**, (2009).
37. J. Laufer, B. Cox, E. Zhang, and P. Beard , " Quantitative determination of chromophore concentrations from 2D photoacoustic images using a nonlinear model-based inversion scheme," *Appl. Opt.* **49**, 1219-1233 (2010).
38. J. Laufer, E. Zhang, and P. Beard , " Quantitative in vivo measurements of blood oxygen saturation using multiwavelength photoacoustic imaging - art. no. 64371Z," *Photons Plus Ultrasound: Imaging and Sensing 2007* **6437**, Z4371-Z4371 (2007).
39. V. G. Andreev, A. A. Karabutov, and A. A. Oraevsky , " Detection of ultrawide-band ultrasound pulses in optoacoustic tomography," *Ieee Transactions on Ultrasonics Ferroelectrics and Frequency Control* **50**, 1383-1390 (2003).

40. M. H. Xu and L. V. Wang , " Universal back-projection algorithm for photoacoustic computed tomography," *Photons Plus Ultrasound: Imaging and Sensing 2005* **5697**, 251-254 (2005).
41. M. Xu and L. V. Wang , " Universal back-projection algorithm for photoacoustic computed tomography (vol 71, art no 016706, 2005)," *Physical Review E* **75**, 059903 (2007).
42. A. Buehler, A. Rosenthal, T. Jetzfellner, A. Dima, D. Razansky, and V. Ntziachristos , " Model-based optoacoustic inversions with incomplete projection data," *Med. Phys.* **38**, 1694-1704 (2011).
43. C. Huang, A. A. Oraevsky, and M. A. Anastasio , " Investigation of limited-view image reconstruction in optoacoustic tomography employing a priori structural information," *Image Reconstruction from Incomplete Data Vi* **7800**, 780004 (2010).
44. G. Paltauf, R. Nuster, M. Haltmeier, and P. Burgholzer , " Experimental evaluation of reconstruction algorithms for limited view photoacoustic tomography with line detectors," *Inverse Problems* **23**, S81-S94 (2007).
45. G. Paltauf, R. Nuster, P. Burgholzer, and M. Haltmeier , " Three-dimensional photoacoustic tomography using acoustic line detectors - art. no. 64370N," *Photons Plus Ultrasound: Imaging and Sensing 2007* **6437**, N4370-N4370 (2007).
46. Y. Sheu, C. Chou, B. Hsieh, and P. Li , " Application of limited-view image reconstruction method to intravascular photoacoustic tomography," *Photons Plus Ultrasound: Imaging and Sensing 2010* **7564**, 75640B (2010).
47. C. Tao and X. Liu , " Reconstruction of high quality photoacoustic tomography with a limited-view scanning," *Optics Express* **18**, 2760-2766 (2010).
48. Y. Xu, L. V. Wang, G. Ambartsoumian, and P. Kuchment , " Reconstructions in limited-view thermoacoustic tomography," *Med. Phys.* **31**, 724-733 (2004).
49. Yang Diwu and Xing Da , " Limited-view scanning photoacoustic imaging based on algebraic reconstruction techniques - art. no. 60470I," *Fourth International Conference on Photonics and Imaging in Biology and Medicine, Pts 1 and 2* **6047**, I470-I470 (2006).
50. G. Paltauf, J. A. Viator, S. A. Prael, and S. L. Jacques , " Iterative reconstruction algorithm for optoacoustic imaging," *J. Acoust. Soc. Am.* **112**, 1536-1544 (2002).
51. P. Ephrat, M. Roumeliotis, F. S. Prato, and J. J. L. Carson , " Four-dimensional photoacoustic imaging of moving targets," *Optics Express* **16**, 21570-21581 (2008).

52. P. Ephrat, L. Keenliside, A. Seabrook, F. S. Prato, and J. J. L. Carson , " Three-dimensional photoacoustic imaging by sparsearray detection and iterative image reconstruction," *J. Biomed. Opt.* **13**, 054052 (2008).
53. P. Ephrat, G. C. Albert, M. B. Roumeliotis, M. Belton, F. S. Prato, and J. J. L. Carson , " Localization of spherical lesions in tumor-mimicking phantoms by 3D sparse array photoacoustic imaging," *Med. Phys.* **37**, 1619-1628 (2010).
54. R. A. Kruger, D. R. Reinecke, and G. A. Kruger , " Thermoacoustic computed tomography-technical considerations," *Med. Phys.* **26**, 1832-1837 (1999).
55. M. Haltmeier, O. Scherzer, and G. Zangerl , " A Reconstruction Algorithm for Photoacoustic Imaging Based on the Nonuniform FFT," *IEEE Trans. Med. Imaging* **28**, 1727-1735 (2009).
56. K. P. Kostli and P. C. Beard , " Two-dimensional photoacoustic imaging by use of Fourier-transform image reconstruction and a detector with an anisotropic response," *Appl. Opt.* **42**, 1899-1908 (2003).
57. K. P. Kostli, D. Frauchiger, J. J. Niederhauser, G. Paltauf, H. P. Weber, and M. Frenz , " Optoacoustic imaging using a three-dimensional reconstruction algorithm," *IEEE Journal on Selected Topics in Quantum Electronics* **7**, 918-923 (2001).
58. K. P. Kostli, M. Frenz, H. Bebie, and H. P. Weber , " Temporal backward projection of optoacoustic pressure transients using Fourier transform methods," *Phys. Med. Biol.* **46**, 1863-1872 (2001).
59. S. Manohar, A. Kharine, J. C. G. van Hespén, W. Steenbergen, and T. G. van Leeuwen , " The Twente Photoacoustic Mammoscope: system overview and performance," *Phys. Med. Biol.* **50**, 2543-2557 (2005).
60. H. B. Jiang, Z. Yuan, and X. J. Gu , " Spatially varying optical and acoustic property reconstruction using finite-element-based photoacoustic tomography," *Journal of the Optical Society of America A-Optics Image Science and Vision* **23**, 878-888 (2006).
61. Z. Yuan, H. Z. Zhao, C. F. Wu, Q. Z. Zhang, and H. B. Jiang , " Finite-element-based photoacoustic tomography: phantom and chicken bone experiments," *Appl. Opt.* **45**, 3177-3183 (2006).
62. Z. Yuan and H. Jiang , " Three-dimensional finite-element-based photoacoustic tomography: Reconstruction algorithm and simulations," *Med. Phys.* **34**, 538-546 (2007).
63. P. Burgholzer, J. Bauer-Marschallinger, H. Gruen, M. Haltmeier, and G. Paltauf , " Temporal back-projection algorithms for photoacoustic tomography with integrating line detectors," *Inverse Problems* **23**, S65-S80 (2007).

64. P. Burgholzer, G. J. Matt, M. Haltmeier, and G. Paltauf , " Exact and approximative imaging methods for photoacoustic tomography using an arbitrary detection surface," *Physical Review E* **75**, 046706 (2007).
65. Z. Guo, C. Li, L. Song, and L. V. Wang , " Compressed sensing in photoacoustic tomography in vivo," *J. Biomed. Opt.* **15**, 021311 (2010).
66. J. Provost and F. Lesage , " The Application of Compressed Sensing for Photo-Acoustic Tomography," *IEEE Trans. Med. Imaging* **28**, 585-594 (2009).
67. D. Modgil, M. A. Anastasio, and P. J. La Riviere , " Photoacoustic image reconstruction in an attenuating medium using singular-value decomposition," *Photons Plus Ultrasound: Imaging and Sensing 2009* **7177**, 71771B (2009).
68. X. Wang, D. L. Chamberland, and D. A. Jamadar , " Noninvasive photoacoustic tomography of human peripheral joints toward diagnosis of inflammatory arthritis," *Opt. Lett.* **32**, 3002-3004 (2007).
69. M. Li, J. Oh, X. Xie, G. Ku, W. Wang, C. Li, G. Lungu, G. Stoica, and L. V. Wang , " Simultaneous molecular and hypoxia imaging of brain tumors in vivo using spectroscopic photoacoustic tomography," *Proc IEEE* **96**, 481-489 (2008).
70. Y. Lao, D. Xing, S. Yang, and L. Xiang , " Noninvasive photoacoustic imaging of the developing vasculature during early tumor growth," *Phys. Med. Biol.* **53**, 4203-4212 (2008).
71. R. J. Zemp, L. A. Song, R. Bitton, K. K. Shung, and L. H. V. Wang , " Realtime photoacoustic microscopy in vivo with a 30-MHz ultrasound array transducer," *Optics Express* **16**, 7915-7928 (2008).
72. J. T. Oh, M. L. Li, H. F. Zhang, K. Maslov, G. Stoica, and L. H. V. Wang , " Three-dimensional imaging of skin melanoma in vivo by dual-wavelength photoacoustic microscopy," *J. Biomed. Opt.* **11**, (2006).
73. B. Rao, L. Li, K. Maslov, and L. H. Wang , " Hybrid-scanning optical-resolution photoacoustic microscopy for in vivo vasculature imaging," *Opt. Lett.* **35**, 1521-1523 (2010).
74. S. Hu, K. Maslov, V. Tsytsarev, and L. V. Wang , " Functional transcranial brain imaging by optical-resolution photoacoustic microscopy," *J. Biomed. Opt.* **14**, (2009).
75. E. W. Stein, K. Maslov, and L. H. V. Wang , " Noninvasive, in vivo imaging of blood-oxygenation dynamics within the mouse brain using photoacoustic microscopy," *J. Biomed. Opt.* **14**, (2009).

76. H. F. Zhang, K. Maslov, G. Stoica, and L. H. V. Wang , " Functional photoacoustic microscopy for high-resolution and noninvasive in vivo imaging," *Nat. Biotechnol.* **24**, 848-851 (2006).
77. H. F. Zhang, K. Maslov, G. Stoica, and L. H. V. Wang , " Imaging acute thermal burns by photoacoustic microscopy," *J. Biomed. Opt.* **11**, (2006).
78. S. L. Jiao, Z. X. Xie, H. F. Zhang, and C. A. Puliafito , " Simultaneous multimodal imaging with integrated photoacoustic microscopy and optical coherence tomography," *Opt. Lett.* **34**, 2961-2963 (2009).
79. J. Laufer, E. Zhang, G. Raivich, and P. Beard , " Three-dimensional noninvasive imaging of the vasculature in the mouse brain using a high resolution photoacoustic scanner," *Appl. Opt.* **48**, D299-D306 (2009).
80. E. Z. Zhang, J. G. Laufer, R. B. Pedley, and P. C. Beard , " In vivo high-resolution 3D photoacoustic imaging of superficial vascular anatomy," *Phys. Med. Biol.* **54**, 1035-1046 (2009).
81. E. Zhang, J. Laufer, and P. Beard , " Backward-mode multiwavelength photoacoustic scanner using a planar Fabry-Perot polymer film ultrasound sensor for high-resolution three-dimensional imaging of biological tissues," *Appl. Opt.* **47**, 561-577 (2008).
82. X. D. Wang, D. L. Chamberland, P. L. Carson, J. B. Fowlkes, R. O. Bude, D. A. Jamadar, and B. J. Roessler , " Imaging of joints with laser-based photoacoustic tomography: An animal study," *Med. Phys.* **33**, 2691-2697 (2006).
83. G. Paltauf, R. Nuster, and P. Burgholzer , " Characterization of integrating ultrasound detectors for photoacoustic tomography," *J. Appl. Phys.* **105**, (2009).
84. R. I. Siphanto, K. K. Thumma, R. G. M. Kolkman, T. G. van Leeuwen, F. F. M. de Mul, J. W. van Neck, L. N. A. van Adrichem, and W. Steenbergen , " Serial noninvasive photoacoustic imaging of neovascularization in tumor angiogenesis," *Optics Express* **13**, 89-95 (2005).
85. R. J. Zemp, L. Song, R. Bitton, K. K. Shung, and L. V. Wang , " Realtime Photoacoustic Microscopy of Murine Cardiovascular Dynamics," *Optics Express* **16**, 18551-18556 (2008).
86. J. J. Niederhauser, M. Jaeger, R. Lemor, P. Weber, and M. Frenz , " Combined ultrasound and optoacoustic system for real-time high-contrast vascular imaging in vivo," *IEEE Trans. Med. Imaging* **24**, 436-440 (2005).
87. J. Gamelin, A. Maurudis, A. Aguirre, F. Huang, P. Guo, L. V. Wang, and Q. Zhu , " A real-time photoacoustic tomography system for small animals," *Optics Express* **17**, 10489-10498 (2009).

88. V. P. Zharov, E. I. Galanzha, E. V. Shashkov, J. Kim, N. G. Khlebtsov, and V. V. Tuchin , " Photoacoustic flow cytometry: principle and application for real-time detection of circulating single nanoparticles, pathogens, and contrast dyes in vivo," J. Biomed. Opt. **12**, 051503 (2007).
89. L. Song, K. Maslov, R. Bitton, K. K. Shung, and L. V. Wang , " Fast 3-D dark-field reflection-mode photoacoustic microscopy in vivo with a 30-MHz ultrasound linear array," J. Biomed. Opt. **13**, 054028 (2008).
90. R. A. Kruger, W. L. Kiser Jr, D. R. Reinecke, and G. A. Kruger , " Thermoacoustic computed tomography using a conventional linear transducer array," Med. Phys. **30**, 856-860 (2003).
91. R. Kruger, D. Reinecke, G. Kruger, M. Thornton, P. Picot, T. Morgan, K. Stantz, and C. Mistretta , " HYPR-spectral photoacoustic CT for preclinical imaging," Photons Plus Ultrasound: Imaging and Sensing 2009 **7177**, 71770F (2009).
92. X. Yang, M. Li, and L. V. Wang , " Ring-based ultrasonic virtual point detector with applications to photoacoustic tomography," Appl. Phys. Lett. **90**, 251103 (2007).
93. H. H. Barrett and H. Gifford, "Cone-beam tomography with discrete data sets" in *Second International Meeting on Fully Three-Dimensional Image Reconstruction in Radiology and Nuclear Medicine* , Phys. Med. Biol. **39**, 451-76 (1994).
94. J. Qi and R. H. Huesman , " Wavelet crosstalk matrix and its application to assessment of shift-variant imaging systems," IEEE Trans. Nucl. Sci. **51**, 123-129 (2004).
95. V. V. Selivanov and R. Lecomte , " Fast PET image reconstruction based on SVD decomposition of the system matrix," IEEE Trans. Nucl. Sci. **48**, 761-767 (2001).

## Chapter 2:

### *Development and characterization of an omnidirectional photoacoustic point source for calibration of a staring 3D photoacoustic imaging system*

This chapter is based on a research paper published in the August 2009 issue of Optics Express. Brief citation as follows: **M. Roumeliotis**, P. Ephrat, J. Patrick, J.J.L. Carson. "Development and characterization of an omni-directional photoacoustic point source for calibration of a staring 3D photoacoustic imaging system", Optics Express **17**(17), pp. 15228-15238, 2009.

This chapter includes the technique employed to design a photoacoustic source that emitted signal uniformly in all directions. The photoacoustic source was used to characterize the array response and produce calibration maps to describe transducer sensitivity, full-width-half-maximum, and time-of-flight.

## 2.1 Introduction

### *2.1.1 Background*

Photoacoustic imaging (PAI) is a hybrid modality capable of providing contrast similar to that of direct optical imaging techniques but with increased penetration depth in turbid media by encoding the optical information as acoustic waves [1,2]. The technique utilizes a pulsed laser to diffusely illuminate optically absorbing objects in the turbid medium. For example, in biological systems, the absorbing objects may include blood vessels and areas of neovasculature embedded within the surrounding tissue (i.e. the turbid medium). Provided the laser pulse is sufficiently brief, thermal confinement criteria are met and cause the optically absorbing objects to most efficiently emit the

absorbed optical energy as a transient bipolar pressure wave [3]. Information related to the location, size, shape, and optical properties of the absorbing objects is present in the pressure waves [4]. The pressure signals acquired over a number of transducers can be processed by a reconstruction algorithm such that images of the optically absorbing objects can be produced [5–8].

There are a number of challenges linked to accurate image reconstruction of objects. Features of the pressure signals vary depending on the position and physical dimensions of the object [3] as well as the optical absorption characteristics. However, these same features of the pressure signals are also affected by the frequency response and angular acceptance of the ultrasound transducers. Furthermore, due to the interaction of propagating pressure waves with ultrasound transducers of finite dimension, the resultant pressure signals can be broadened and arrive at earlier or later times. Therefore, without detailed information of the system response, all algorithms will reconstruct images of objects that have misregistration artifacts and errors in the size, shape and contrast of the objects.

Characterization of photoacoustic imaging system response has been estimated through several approaches. Most relevant to photoacoustic system calibration are techniques to calibrate conventional ultrasound imaging systems because the angular acceptance of ultrasound transducers is inherent to both imaging modalities. This includes a strategy developed by Foster et al., which characterized the signal produced by a transmitting element at varying angles off the acoustic transmission axis [9]. Wang et al. [10,11] have implemented ring-shaped ultrasonic transducers which act as virtual point detectors. These virtual point detectors can be used to detect photoacoustic signals in the same way as a real point detector. Therefore, uniform sensitivity to photoacoustic signals throughout the imaging field of view can be assumed during image reconstruction. Kruger et al. [12] have measured the system response by constructing a point source by pulsed illumination of a spot-coated 0.1 mm polyethylene fibre. As the source was translated through the object space, the axial response of the system was measured. In a similar strategy, our lab [13] implemented the use of a point source



created by pulsed illumination down an optical fibre to an absorbing tip to characterize the response of a detector array. By translating the source incrementally in the three coordinate directions the response of the array was characterized throughout the entire object space. System response was mapped for each voxel-transducer pair which could later be incorporated into the reconstruction algorithm. Other imaging modalities, including SPECT and PET, have been characterized using similar techniques to obtain the system response [14,15].

### ***2.1.2 Objective and approach***

We have previously reported on a method to fabricate a point source at the tip of an optical fibre [13,16]. Limited success was achieved, leaving opportunity for an improved point source to more accurately characterize the system response. From our earlier results, it appeared as though physical imperfections due to manual construction of the fibre tip caused significant azimuthal signal non-uniformity. As well, predictable, but highly directional emission characteristics were observed in the zenith direction. For a transducer array that has significant coverage over a large solid angle (e.g. hemispherical array described in [17]), calibration of the system response required that we develop a point source with omnidirectional emission character.

Our approach was to construct a fibre optic PA point source where the coated tip was replaced with a liquid medium having optically absorbing and scattering properties. As light is directed into an optically absorbing liquid, the shape of the beam is maintained in a directional path as no scattering component is present. The photons are then absorbed along the directional path which subsequently produces a directional acoustic wave. If a scattering component is then added to the absorbing liquid, the distribution of light in the medium begins to result in a spherical-like shape. When the scattering component becomes too large, a region of high back-scatter is produced near the photon injection site causing the absorption of the photons primarily to occur in a directional pattern at the surface of the liquid. Therefore, it was our goal to develop a liquid with an appropriate balance of both scattering and absorption components which would produce a

photoacoustic point source. Ideally, the point source would emit a uniform acoustic wave in both the azimuthal and zenith orientations. The source could later be used to characterize response parameters for signal amplitude, time-of-flight, and width.

## 2.2 Methods

### 2.2.1 *The photoacoustic imaging system*

A schematic of the photoacoustic system is shown in Fig. 2.1(a). The imaging system utilized 15 ultrasound transducers (model V304, 1" Ø, 2.25 MHz with fractional bandwidth of 65%, *Panametrics-NDT*, Waltham, Massachusetts) in a staring hemispherical arrangement. Transducers were mounted on 5 custom-built frame columns, each supporting 3 transducers at zenith angles of 22.5°, 45°, and 67.5°. The design of the frames ensured that the directional sensitivity of all 15 transducer overlapped in a object space of approximately 25x25x25 mm near the geometric center of the array. The 5 columns were spread azimuthally by 72° to provide uniform coverage over 360°. The container surrounding the transducers was filled with water to provide an acoustic coupling medium. Laser illumination ("Surelite OPO Plus", OPO-coupled Nd:YAG, *Continuum*, Santa Clara, California) was directed to a bifurcated fibre (400 µm diameter) such that half the light was directed to a photodiode (to measure pulse-to-pulse variation) and the other half to an optical fibre immersed in the liquid, where the light could be scattered and absorbed. Prior to acquiring acoustic signals, the fibre optic was soaked in the liquid solution for 20 minutes to allow any staining of the fibre to be consistent through experimental iterations. The pulse duration was 6 ns at a repetition rate of 10 Hz with a maximum output of approximately 100 mJ/pulse. All experiments were performed at 675 nm. Each transducer element was electrically connected to a dedicated channel on a preamplifier card (custom built). The analog signals were acquired in parallel, converted to digital signals, and sent to a personal computer for analysis. The data acquisition system was custom built and sampled with 14-bit resolution at a frequency of 50 MHz. Figure 2.1(a) and Fig. 2.1(b) illustrate the systems used to characterize the PA

point source as well as a representative time trace shown in Fig. 2.1(c) indicating the metrics used to fully describe wave parameters.

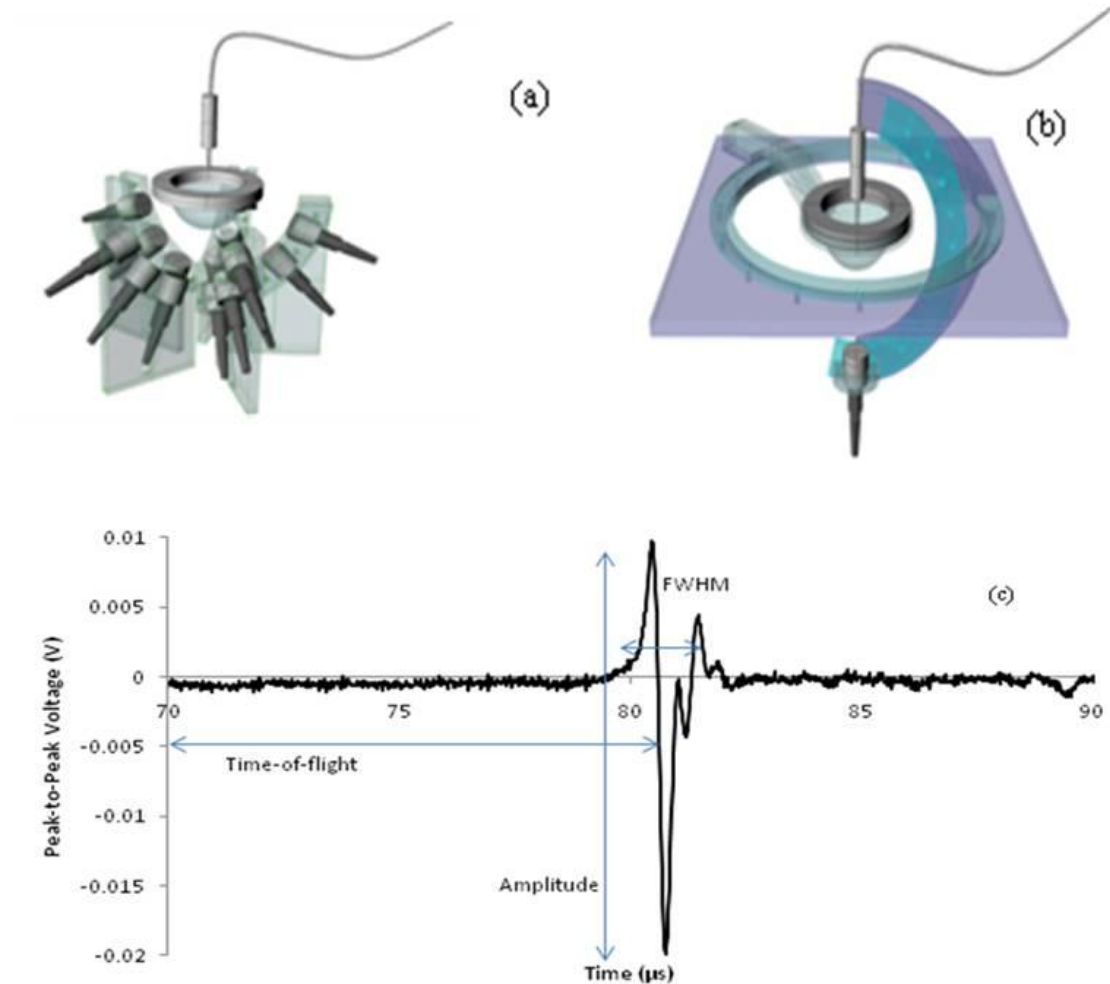


**Figure 2.1:** (a). Isometric view of the hemispherical PA imaging array illustrating the transducer arrangement, placement of the liquid reservoir, and the optical fibre PA source. (b). Isometric view of the system for detailed PA source characterization illustrating one transducer, the transducer arm, the liquid reservoir and the optical fibre. The transducer arm was capable of rotation in  $15^\circ$  increments in the zenith direction and  $22.5^\circ$  increments in the azimuthal direction. (c). Example of raw data acquired on a single acoustic transducer. Signal time-of-flight, amplitude, and FWHM are labeled.

### ***2.2.2 Source uniformity characterization***

The fibre optic cable was mounted to the stage of a  $xyz$ -scanning gantry and translated to a position where the fibre tip was equidistant from each of the 15

transducers. The fibre tip was immersed entirely in a homogeneous mixture of water, methylene blue, and Intralipid™ (MB<sup>+</sup>/IL) held within a reservoir at the geometric center of the array as shown in Fig. 2.1(a). The container was constructed from a supporting ring from which a bag formed from standard kitchen wrap was suspended. Methylene blue was added to the reservoir from a 1 mM stock solution. Four different reservoir solutions were tested at methylene blue concentrations of 50, 100, 150, and 200 μM. A separate auxiliary solution of MB<sup>+</sup>/IL was made for each of the corresponding reservoir concentrations. As the auxiliary solution was added to the reservoir solution, the concentration of methylene blue was maintained while the scatter percentage was increased by 0.01%. The reservoir Intralipid™ concentration was systematically increased from 0 to 0.11% in 0.01% increments. At each condition, the PA signal was sampled for five laser pulses and averaged. The peak-to-peak distance representative of the PA signal amplitude recorded at each transducer was extracted from each averaged time series. The experiment was performed 3 times, each time with fresh solutions.

### ***2.2.3 Source directionality characterization***

Using a separate system for calibration, the directionality of the emission from the liquid PA source was measured with a single transducer at locations equidistant to the PA source in the azimuthal and zenith directions (Fig. 2.1(b)). In a manner similar to the experiments with the array, the fibre tip was immersed in a MB<sup>+</sup>/IL solution (200 μM MB<sup>+</sup> and 0.09% Intralipid™). At this solution concentration, the absorption and scattering coefficient were approximately 37 cm<sup>-1</sup> and 4 cm<sup>-1</sup>, respectively. The arm holding the transducer had the capability to rotate in 15° increments in the zenith direction and 22.5° increments in the azimuthal direction. With the fibre stationary at a position equidistant from all possible transducer locations, the single transducer was rotated every 45° in the azimuth and 15°, 45°, and 75° in the zenith. At each transducer position, the peak-to-peak value of the PA signal was obtained exactly as described above for the array experiment. The experiment was repeated 3 times, each time with fresh solutions.

### ***2.2.4 System calibration scan***

Using a MB<sup>+</sup>/IL solution of identical composition to the solution used for the source directionality characterization experiments, a calibration scan was performed using the liquid PA point source. The fibre tip of the PA source was incrementally translated through a cubic volume of 40x40x40 mm<sup>3</sup>. The center point of the cube was coincident with the point equidistant from all 15 transducers. The source was translated in 8 mm increments in the *x*, *y*, and *z*-directions providing a total of 216 test positions. At each test position, the PA signal was sampled for 10 laser pulses and averaged. The PA signal was recorded simultaneously on all 15 transducers and later analyzed to map signal amplitude, width, and time-of-flight for each position of the source in the object space (see Fig. 2.1(c)).

## **2.3 Results**

### ***2.3.1 Source uniformity characterization***

Figure 2.2 shows the results of the source uniformity characterization. Figure 2.2(a) illustrates the change in signal amplitude (peak-to-peak) as a function of the Intralipid™ percentage. For each combination of MB<sup>+</sup> and IL, the average signal amplitude (represented by symbols) was computed using all 15 transducers. Error bars show the standard deviation computed over all three trials (45 total measurements). Each curve represents the result for a specific value of MB<sup>+</sup> concentration. Figure 2.2(b) shows the coefficient of variation from the data corresponding to Fig. 2.2(a) as a function of Intralipid™ percentage. The coefficient of variation was found by computing the ratio of the standard deviation to the mean value of each data point in Fig. 2.2(a). This indicated which of the PA sources statistically produced the most uniform signal. As was the case in Fig. 2.2(a), each curve represents a different methylene blue concentration.

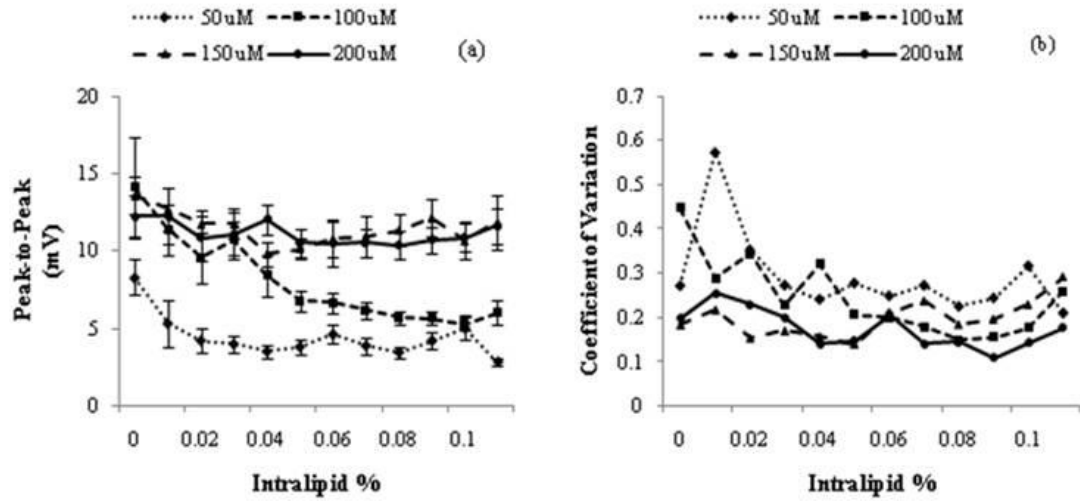


**Figure 2.2:** (a). Peak-to-peak PA signal amplitude as a function of absorption ( $\text{MB}^+$ , top legend) and scatter (Intralipid™) for a liquid PA point source. Error bars represent  $\pm$  one standard deviation. (b) Coefficient of variation for data corresponding to (a).

### 2.3.2 Source directionality characterization

Figure 2.3 shows the results of the directionality characterization in both the zenith and azimuthal orientations of the 200  $\mu\text{M}$   $\text{MB}^+$ /0.09% IL photoacoustic source. Each amplitude measurement was averaged over 5 laser pulses and subsequently averaged with each of the 3 experimental iterations. Error bars show the standard deviation for a given trial averaged over the 3 iterations. Each curve indicates a particular zenith elevation while each point on a curve indicates a distinct azimuthal position.

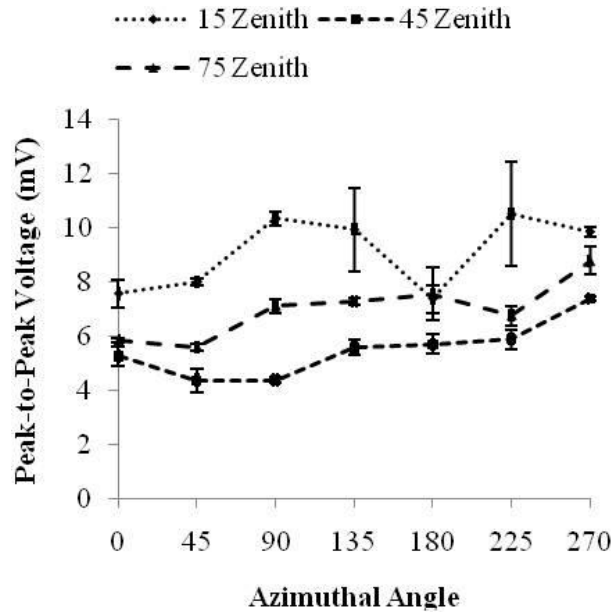


**Figure 2.3:** Curves illustrating signal amplitude as a function of azimuthal position for varying zenith orientations. Error bars represent  $\pm$  one standard deviation.

### 2.3.3 System calibration scan

Figures 2.4(a), 2.4(b), and 2.4(c) illustrate visually the characterization of signal amplitude, width, and time-of-flight, respectively, for each transducer at each position in the calibration volume. PA signals were analyzed as described in Fig. 2.1(c). Each column in Fig. 2.4 represents a particular transducer which corresponds to the transducer labeled in Fig. 2.4(i). Within a column, each of the 6 planar images illustrates an x-y plane at a different depth in the object space.

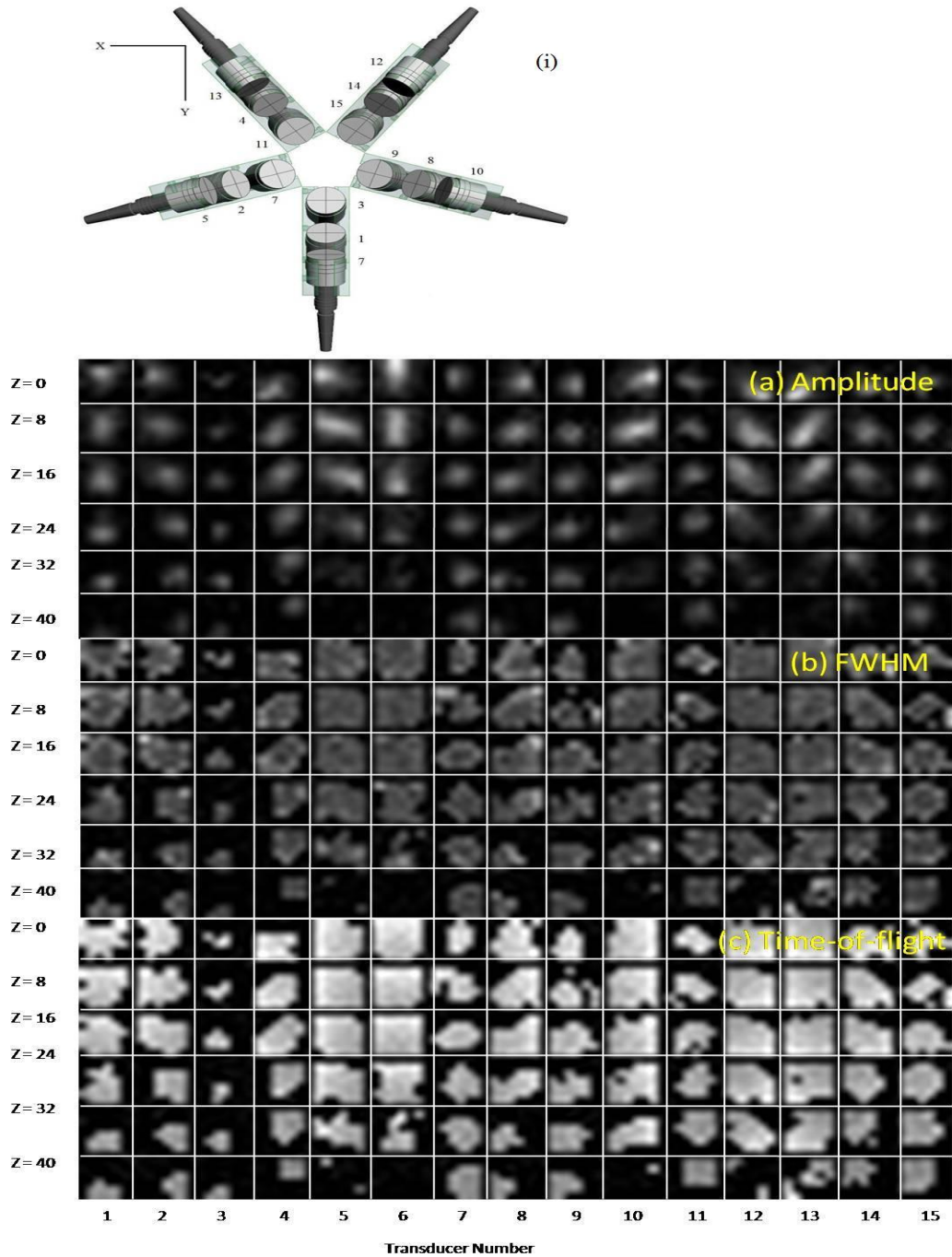


**Figure 2.4:** (i) Transducer arrangement correlating transducer number to the columns in Figs. 2.4(a)-(c). Calibration maps of the metrics describing the PA signal detected by each transducer at each position within the calibration volume. (a) Signal amplitude - the magnitude of the peak-to-peak voltage acquired (b) Signal width - the FWHM of the signal, and (c) Signal time-of-flight - a measure of the arrival time after laser trigger. The grey scale in Fig. 2.4(a)-(c) indicates an increase in PA wave amplitude, FWHM, and time-of-flight, respectively.



## 2.4 Discussion

### *2.4.1 Overview of basic findings*

Photoacoustic imaging system characterization is important when directional sensitivity and/or the finite dimensions of acoustic transducers affect the detected PA signals. System characterization is essential if the variation in these properties differ among elements within the PA transducer array. The methodology developed and tested here promises to be useful for characterizing the system response of PA imaging systems, especially those that form an aperture with large solid angle. Furthermore, transducer-specific responses at multiple locations within the object space provide information vital to the accurate reconstruction of photoacoustic images. The straightforward process of scanning an optical fibre within a reservoir of suitably designed liquid allows tuning of the resultant PA source and can be used to perform calibration scans tailored to PA transducer arrays that are optimized for a different spatial scales, e.g.  $< 50 \mu\text{m}$  diameter fibre optic cable for a PA microscopy setup versus a larger diameter fibre for macroscopic ( $\sim 1 \text{ mm}$ ) imaging setups. It is important to note that any attempt to scale a spherical source to the fibre diameter would need to accurately define important physical system parameters such as absorption coefficient, scattering coefficient, anisotropy in optical scatter, as well as the optical injection pattern (estimated by the fibre's numerical aperture). Modeling of the resulting optical distribution could then be estimated accurately by Monte Carlo simulations. In general, however, it is expected that the effective penetration depth of the light should be roughly half the diameter of the fibre to achieve an optical distribution that is approximately spherical. More specifically, the inverse of the total attenuation coefficient should be equal to half the diameter of optical fibre. This is of particular importance when tuning a PA source for systems beyond that used in this experiment.

### ***2.4.2 MB<sup>+</sup>/IL as a PA source***

The motivation for the selection of the MB<sup>+</sup> concentration used to calibrate the transducer array was based on the observation that a plateau in signal strength was approached regardless of the concentration provided in the MB<sup>+</sup>/IL solution. This trend is evident in Fig. 2.2(a) in which the MB<sup>+</sup>/IL solutions of 150  $\mu\text{M}$  and 200  $\mu\text{M}$  provided PA signals with similar peak-to-peak signal amplitudes over much of the concentration range for Intralipid<sup>TM</sup>. It is intuitive to correlate signal amplitude with MB<sup>+</sup> concentration. The absorption coefficient of the liquid increases as the concentration of the MB<sup>+</sup> increases, resulting in larger peak-to-peak signal amplitudes. However, increasing the concentration of MB<sup>+</sup> will ultimately reduce the penetration depth of light into the liquid, reducing the effective dimensions of the source and the associated width of the PA signal. To conserve energy, the total area under the curve remains constant as the number of photons delivered to the system to create the acoustic signal is constant for each pulse. The transducers used in the experiments have a limited bandwidth. It is for this reason that the signal amplitude recorded by the transducers is not as straightforward as is determined by exclusively considering the absorption coefficient of the source. For a centre frequency of 2.25 MHz, the response peak occurs when an object is approximately 400-500  $\mu\text{m}$ . As the effective penetration depth of the source is decreased beyond these dimensions, the reduction in amplitude due to frequency response begins to compete with the increase in pressure wave amplitude due to the increased absorption. If the dimensions of the source were restricted further, eventually the transducer would not produce any signal as the frequency of the pressure wave would be outside the transducer's bandwidth. The selection of the optimal liquid was then made by comparing the coefficient of variation for each liquid combination. The coefficient of variation, shown in Fig. 2.2(b), permits selecting the MB<sup>+</sup>/IL solution with the least signal variability among experimental iterations.

### ***2.4.3 Variation in PA signal intensity as a function of zenith and azimuth***

Although the initial characterization experiment to determine the optimal (i.e. lowest coefficient of variation) combination of absorption and scatter used the entire transducer array, the measurements were dependent on variations in sensitivity between transducers. This likely was present as a systematic error in the results presented in Fig. 2.2. To overcome this potential issue related to interpretation of the results, a PA source directionality characterization was completed with a single transducer mounted on a rotatable arm that permitted sensing of the PA signal from a variety of azimuthal and zenith positions at constant distance. This approach eliminated transducer-to-transducer variability as a contributing factor to signal fluctuations. We observed reasonable PA signal uniformity in the azimuthal direction and systematic decline in PA signal intensity as the zenith elevation angle increased. This was in contrast to our previously published work with a coated fibre-based PA source in which azimuthal signal uniformity was poor [13]. The decline in PA signal strength as a function of zenith, suggested that the light emitted from the fibre did not scatter and absorb as a perfect sphere. It is possible the fibre staining (described in section 2.1) could have created a region of high  $\text{MB}^+$  concentration very close to the fibre tip. This would effectively create a gradient of  $\text{MB}^+$  concentration immediately below the surface of the fibre which could account for the zenith non-uniformity. Further detailed characterization of the liquid PA source with respect to the ratio of  $\text{MB}^+/\text{IL}$  through experiment and perhaps Monte Carlo simulation might provide insight. The experimental results obtained with the liquid sources suggested that it may be better suited to transducer calibration procedures than coated optical fibres [13].

### ***2.4.4 Calibration maps***

The calibration maps shown in Fig. 2.4 visually illustrate the relative signal amplitude, width, and time-of-flight for many calibration locations within the object

space for every transducer. Figure 2.4(a), showing the signal amplitude at each calibration location, clearly indicates the directionality of each transducer. For example, transducer 12 and 13 (columns 12 and 13) stare at the object space from an orientation off the acoustic axis. These results correlate well with the actual physical orientation of the transducers indicating the calibration map is accurately reporting signal sensitivity. Of interest is the extreme sensitivity reduction outside the axial line-of-sight for all transducers. This implied that signal generated and transmitted from a photoacoustic source off the acoustic axis (approximately  $\pm 15$  mm) could be easily concealed in the background noise. This suggests that the large 25 mm diameter transducers used to populate the transducer array confined the effective object space to a spherical volume  $30 \times 30 \times 30$  mm<sup>3</sup> by the overlap of the calibration sensitivity maps. Figure 2.4(b) illustrates the behavior of the signal FWHM at each calibration location. The difference in FWHM is generally small from position to position. However, the outer edges of the object space tend to broaden the acoustic signal as it sweeps over the face of the transducer as opposed to directly impinging the transducer when the signal propagates on the acoustic axis. While visibly difficult to discern, this trend is generally evident in the FWHM patterns in that they tend to show larger signals at the periphery of a given z-slice. As well, the complexity of the FWHM patterns indicates any modeling to predict the FWHM of a PA signal would be very difficult. Shown in Fig. 2.4(c) is the time-of-flight map. Perhaps the most important information garnered from the time-of-flight response is the presence of dark spots at a variety of locations in the object space. Typically these positions were found in regions which corresponded to low signal amplitude (as seen in Fig. 2.4(a)). Likely, signals were masked in the noise and went undetected at those particular calibration positions because of the reduced amplitudes off the acoustic axis of a transducer.

### ***2.4.5 Impact of calibration maps on image reconstruction***

While the calibration scan did not specifically touch each voxel in the reconstructed object space, the points absent from the scan were computed by linearly interpolating nearest neighbours. These values can be applied to the iterative

reconstruction algorithm to modify the signal parameters attained when collecting image data. While this particular calibration scan has not been used to reconstruct new objects, previous scans have been applied to the reconstruction algorithm with success. The previous scans were implemented using sources of lower quality and still provided reasonable success [17].

#### ***2.4.6 Advantages/Disadvantages of approach***

In general, the liquid PA calibration source has proven to have a number of intrinsic advantages. Primarily, the inherent nature of the light propagation through a homogenous liquid is symmetric about the long axis of the optical fibre therefore leads to consistent PA signal emission in any azimuthal orientation. In comparison, manually constructed sources demonstrate azimuthal variability as a difficult obstacle to overcome as any physical imperfection in the source geometry translates to inconsistent acoustic sources. A second advantage of the liquid source is the ability for the user to tune the optical absorption and scatter coefficients very easily. This allows an experimenter the capability to affect the photoacoustic emission properties in a repeatable and simple manner. A significant shortcoming of the MB<sup>+</sup>/IL source was observed when the fibre optic was immediately placed within the liquid bath. Signal strength was initially much greater than the signal strength recorded after allowing the fibre to soak in the reservoir for approximately 20 minutes. Likely, this was observed due to MB<sup>+</sup> staining of the fibre tip. While the experiments were always conducted after the soaking process, there was no certain length of time in which the signal would not reduce further. To that end, the signals produced were relatively small in magnitude compared to what might be considered ideal. The signal amplitude was adequate when the source was positioned directly on the acoustic axis but would more easily be masked by the background noise when off-axis as the signal-to-noise ratio (SNR) was not as great as was seen in other omnidirectional sources.

### ***2.4.7 Future work***

Improvements could be made on the photoacoustic source as well as the calibration process. Reasonably comprehensive experiments were conducted on a variety of different absorption and scattering combinations for the MB<sup>+</sup>/IL solution. The spherical-like shape of the source can be inferred from the signals detected by the hemispherical array of transducers. However, theoretical predictions attesting to the behavior of the source were not made. Monte Carlo simulations could be produced on light injected to a system of known scattering and absorption coefficients with known fibre specifications (numerical aperture and core diameter). As well, the current liquid solution seemingly stains the fibre optic after being immersed for a period of time. The liquid responsible for the absorption coefficient (in this case, methylene blue) could be replaced by a source with less significant staining or the fibre could be replaced by a fibre of different material, such as plastic. The calibration itself could be improved to provide enhanced coverage of the object space. Specifically, the distance between successive steps in all planes could be reduced if the scanning system had the potential for greater speed. A calibration scan of 216 source positions takes approximately 1 hour to complete. Even doubling the number of calibration steps in each orientation (i.e. reducing step size from 8 mm to 4 mm) requires the calibration to have 1331 source positions if the object space is maintained.

## **2.5 Conclusion**

A liquid-based photoacoustic point source was developed and used to characterize signal amplitude, width, and time-of-flight for each voxel-transducer pair. The liquid source resulted in uniform signals via a liquid photoacoustic source in which scattering components provided the spherical light distribution in the liquid. A combination of MB<sup>+</sup> at 200  $\mu$ M and IL at 0.09% proved to be the liquid solution with least variability in signal strength. Because the liquid source is inherently uniform in the azimuthal orientation, this

source showed immediate improvement compared to previous iterations of an attempt to create an omni-directional photoacoustic source. Despite the promise seen in the signal consistency, the magnitude was typically much lower than that of previously used sources which allowed the signal to go undetected more rapidly. A calibration scan was completed with the liquid photoacoustic source in an object space of  $40 \times 40 \times 40 \text{ mm}^3$  where signal amplitude, width, and time-of-flight were recorded. Ultimately, the source provided the photoacoustic system with supplementary information to be applied to the reconstruction algorithm in an effort to produce images of greater accuracy.

## 2.6 References

1. T. Lu, J. Jiang, Y. Su, R. K. Wang, F. Zhang, and J. Yao, "Photoacoustic imaging: Its current status and future development," in *4th International Conference on Photonics and Imaging in Biology and Medicine*, (SPIE, 2006), **6047**.
2. M. Xu, and L. V. Wang, "Photoacoustic imaging in biomedicine," *Rev. Sci. Instrum.* **77**(4), 041101 (2006).
3. G. J. Diebold, T. Sun, and M. I. Khan, "Photoacoustic monopole radiation in one, two, and three dimensions," *Phys. Rev. Lett.* **67**(24), 3384–3387 (1991).
4. G. Paltauf, J. A. Viator, S. A. Prahl, and S. L. Jacques, "Iterative reconstruction algorithm for optoacoustic imaging," *J. Acoust. Soc. Am.* **112**(4), 1536–1544 (2002).
5. P. Liu, "The P-transform and photoacoustic image reconstruction," *Phys. Med. Biol.* **43**(3), 667–674 (1998).
6. C. G. A. Hoelen, and F. F. M. de Mul, "Image reconstruction for photoacoustic scanning of tissue structures," *Appl. Opt.* **39**(31), 5872–5883 (2000).

7. D. Frauchiger, K. P. Kostli, G. Paltauf, M. Frenz, and H. P. Weber, "Optoacoustic tomography using a two dimensional optical pressure transducer and two different reconstruction algorithms," in *Hybrid and Novel Imaging and New Optical Instrumentation for Biomedical Applications*, (SPIE, 2001), **4434**, pp. 74–80.
8. M. Xu, and L. V. Wang, "RF-induced thermoacoustic tomography," in *Proceedings of the 2002 IEEE Engineering in Medicine and Biology 24th Annual Conference and the 2002 Fall Meeting of the Biomedical Engineering Society (BMES / EMBS)*, (Institute of Electrical and Electronics Engineers Inc, 2002), pp. 1211–1212.
9. D. H. Turnbull, and F. S. Foster, "Fabrication and characterization of transducer elements in two-dimensional arrays for medical ultrasound imaging," *IEEE Trans. Ultrason. Ferroelectr. Freq. Control* **39**(4), 464–475 (1992).
10. X. Yang, and L. V. Wang, "Photoacoustic tomography of a rat cerebral cortex with a ring-based ultrasonic virtual point detector," *J. Biomed. Opt.* **12**(6), 060507 (2007).
11. C. Li, and L. V. Wang, "High-numerical-aperture-based virtual point detectors for photoacoustic tomography," *Appl. Phys. Lett.* **93**(3), 033902 (2008).
12. R. A. Kruger, W. L. Kiser, Jr., D. R. Reinecke, and G. A. Kruger, "Thermoacoustic computed tomography using a conventional linear transducer array," *Med. Phys.* **30**(5), 856–860 (2003).
13. P. Ephrat, and J. J. L. Carson, "Measurement of photoacoustic detector sensitivity distribution by robotic source placement," in *9th Conference on Photons Plus Ultrasound: Imaging and Sensing 2008*, (SPIE, 2008), **6856**.
14. F. van der Have, B. Vastenhouw, M. Rentmeester, and F. J. Beekman, "System calibration and statistical image reconstruction for ultra-high resolution stationary pinhole SPECT," *IEEE Trans. Med. Imaging* **27**(7), 960–971 (2008).



15. Y. Pawitan, S. Kohlmyer, T. Lewellen, and F. O'Sullivan, "PET system calibration and attenuation correction," in *Part 1 (of 3)*, (IEEE, 1996), pp. 1300–1304.
  
16. M. Roumeliotis, P. Ephrat, and J. J. L. Carson, "Development of an omni-directional photoacoustic source for the characterization of a hemispherical sparse detector array," in *Photons Plus Ultrasound: Imaging and Sensing 2009: The Tenth Conference on Biomedical Thermoacoustics, Optoacoustics and Acousto-optics* (SPIE 2009) **7177**, 71772F.
  
17. P. Ephrat, M. Roumeliotis, F. S. Prato, and J. J. L. Carson, "Four-dimensional photoacoustic imaging of moving targets," *Opt. Express* **16**(26), 21570–21581 (2008).

## Chapter 3:

### *Analysis of a photoacoustic imaging system by the crosstalk matrix and singular value decomposition*

This chapter is based on a research paper published in the May 2010 issue of Optics Express. Brief citation as follows: **M. Roumeliotis**, R.Z. Stodilka, M.A. Anastasio, G. Chaudhary, H. Al-Aabed, E. Ng, A. Immucci, J.J.L. Carson. “Analysis of a photoacoustic imaging system by the crosstalk matrix and singular value decomposition”, Optics Express **18**(11), pp. 11406-11417, May 2010.

This chapter includes the methodology used to acquire an experimental imaging operator of a photoacoustic imaging system using the photoacoustic source developed in Chapter 2. The crosstalk matrix and singular value decomposition are used to further characterize the imaging system’s object space. This includes object space aliasing, sensitivity, as well as the number of singular vectors contributing to image reconstruction.

## 3.1 Introduction

### *3.1.1 Background*

Photoacoustic imaging (PAI) is a non-ionizing imaging modality that produces images based on the preferential absorption of optical energy in an absorber by means of the photoacoustic effect. The technique provides images of objects in turbid media with contrast similar to direct optical imaging techniques, but with increased resolution and penetration depth by encoding the optical information as acoustic waves [1,2]. PAI employs the use of a pulsed laser to diffusely irradiate a volume of interest. The optical energy is deposited rapidly allowing the thermal confinement condition to be met, which facilitates the thermo-elastic expansion of the absorbing structure leading to an outwardly

propagating transient bipolar pressure wave [3]. Information is contained within the pressure wave regarding the location, size, shape, and optical properties of the absorbing objects [4]. Using the time-domain measurements acquired by acoustic transducers, an image of the distribution of optical absorbers inside the target volume can be inferred using an image reconstruction algorithm [5-10].

Typical metrics utilized to guide imaging system optimization tasks include sensitivity, resolution, and contrast. However, the characterization process can be extended beyond classic metrics by implementing techniques that generate higher level information. This includes the singular value decomposition (SVD) technique and the crosstalk matrix to extract additional system information. The SVD technique produces information concerning the geometry and sensitivity to objects that can be resolved by the system via decomposition of the imaging operator into a set of matrices that are representative of these systems qualities [11,12]. Understanding the geometry of objects that can be sensed by an imaging system is of particular importance when the imaging system acquires a limited number of data projections as system limitations will inevitably be significant when reconstructing images, as is the case with a staring, sparse-array PAI system recently described by our group [13-15]. The crosstalk matrix generates information that describes the spatially dependent sensitivity and aliasing (defined as the inability to distinguish expansion coefficients from each other) of an imaging system. These metrics are important to understanding system resolution in shift-variant imaging systems [16]. In broad terms, the application of the SVD technique and crosstalk matrix to any photoacoustic imaging system can provide a method to comprehensively understand properties of the imaging operator. Consequently, the results can be used to guide improvement and performance by optimization of transducer orientation and bandwidth as well as the number of data projections required to accurately reconstruct objects of relevant geometry.

### ***3.1.2 Singular value decomposition***

Singular value decomposition provides a significant portion of the work in this chapter. For details, please refer to section 1.5.3.

### ***3.1.3 The crosstalk matrix***

The crosstalk matrix is used in this chapter as a technique to quantify particular features of our imaging system. For details, please refer to section 1.5.2

### ***3.1.4 Objective***

We have previously reported on a method to calibrate a 3D photoacoustic imaging system by way of the translation of a point source through the object space [15]. This calibration process recorded the response of each transducer in terms of the amplitude, duration, and time-of-arrival of each received pressure wave. Due to technological limitations, the sparseness of the calibration scan was a significant shortcoming in obtaining a comprehensive system response. To more accurately implement the singular value decomposition technique and the crosstalk matrix, it was vital that our calibration process be improved in order to acquire the system response at a step-size approaching the resolution limit of the imaging system. According to Oraevsky et al. [17], the theoretical resolution limit due to transducer bandwidth in our PA system is approximately 500  $\mu\text{m}$ . However, as shown in previous works, the practical resolution of our system is closer to 1-2 mm [13]. In concurrence with this estimated resolution, it was our objective to acquire a calibration scan with a step-size on the order of the system resolution that spans a volume that approximately corresponds to the transducer sensitivity ( $25 \times 25 \times 25 \text{ mm}^3$ ). The imaging operator derived from the calibration scan could then be used to comprehensively understand the performance and limitations of our system by SVD and crosstalk matrix analysis.

### ***3.1.5 Approach***

Our approach was to produce a dense calibration scan by means of improving the point source scanning technique published in previous work [15]. While the previous calibration scan was sparse (in relation to the system resolution), the new methodology was utilized to provide a dense system response on the order of the system resolution. Improvements were made to the data acquisition rate and point source translation interval to reduce the net time required to acquire the data from a particular location in object space. After a dense calibration scan was acquired, singular value decomposition and crosstalk analysis were performed on the imaging operator that provided information to characterize our photoacoustic imaging system with regards to the spatially dependent sensitivity, aliasing, as well as the geometry and orientation of objects that can be distinguished. As well, a de-noised imaging operator was constructed in order to compare the experimental imaging operator to a de-noised imaging operator containing the same shift-variant response as the experimental system but with greatly reduced noise.

## **3.2 Methods**

### ***3.2.1 Photoacoustic imaging system***

The imaging system utilized 15 ultrasound transducers (model V304, 1" diameter, 2.25 MHz with fractional bandwidth of 65%, *Panametrics-NDT*, Waltham, Massachusetts) in a staring hemispherical arrangement. Transducers were mounted on 5 custom-built frames, each supporting 3 transducers at zenith angles of 22.5°, 45°, and 67.5°. The frames were designed such that the sensitivity of all 15 transducers were intended to overlap in a specified object space of approximately 25x25x25 mm<sup>3</sup> near the geometric center of the array. Laser illumination ("Surelite OPO Plus", OPO-coupled Nd:YAG, *Continuum*, Santa Clara, California) was directed to a bifurcated fibre (400 µm

diameter) such that half of each laser pulse was guided to a photodiode (to measure pulse-to-pulse variation) and the other half to an optical fibre immersed in the liquid (where the photoacoustic signal was generated) for a total of 16 channels collecting data (15 transducers, 1 photodiode). The pulse duration was 6 ns at a repetition rate of 10 Hz with a maximum laser output of approximately 100 mJ/pulse. Note that only a small fraction of the pulse was accepted by the fibre due to its small core size relative to the beam diameter (~1.5 cm). All calibration scans were done at 675 nm. Each transducer was electrically connected to a dedicated channel on a preamplifier card (custom built). The analog signals were acquired in parallel, converted to digital signals, and sent to a personal computer for analysis. The custom built data acquisition system sampled with 14-bit resolution at a frequency of 50 MHz. The PA system (with PA point source and optical fibre) is shown in Fig. 3.1(a) while a representative PA time series acquired during an experiment from a single transducer is shown in Fig. 3.1(b).

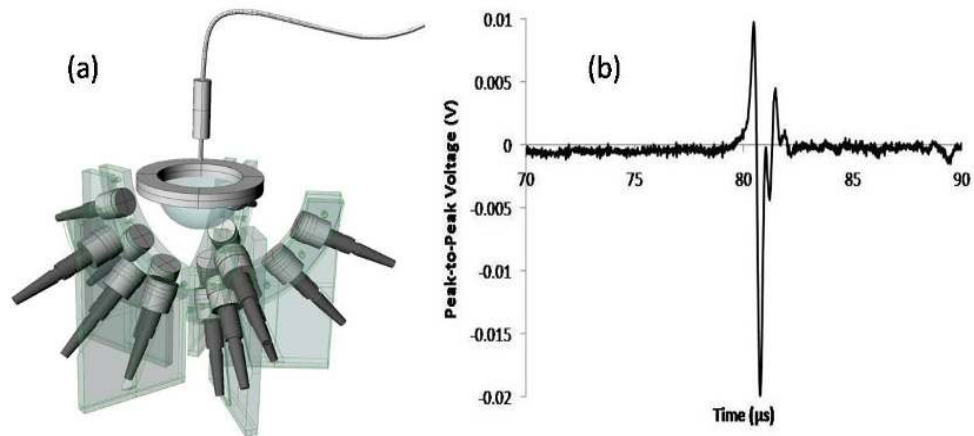


**Figure 3.1:** (a) Isometric view of the hemispherical PA imaging array illustrating the transducer arrangement, placement of the liquid reservoir, and the optical fibre PA source. (b) Example of raw data acquired on a single acoustic transducer.

### 3.2.2 System calibration scan

In order to acquire calibration scans with step-size on the order of the system resolution, a number of improvements were made to the scan procedure in comparison to

our previous work [15]. First, the linear slides responsible for translating the optical fibre through the absorbing liquid were replaced with a SCARA robot (Model E2C351S - UL, Epson), which could translate the source between data points faster and more reliably to reduce translation time. Second, the data acquisition cards were updated with USB 2.0 connections to relay data to the PC in a much shorter interval. With the upgrades, each scan point required approximately 15 seconds to complete. Subsequently, two calibration scans were performed with different object spaces and step-sizes. The first scan was completed with a  $16 \times 16 \times 16 \text{ mm}^3$  object space and 2 mm step-size for a total of 512 data points. The second scan was performed on an object space of  $30 \times 30 \times 30 \text{ mm}^3$  and 3 mm step-size for a total of 1000 data points. At each test position in the scan, the PA signal was averaged over 10 pulses and recorded simultaneously on all 15 transducers. After the calibration scan, the time series data for each transducer and grid location was analyzed off-line to obtain the imaging operator corresponding to each scan. Analysis included extracting the time series of a particular transducer and grid point, rectifying the time series, and then smoothing the time series using a moving average with a bin size of 40 points. Each time series was copied to the matrix representative of the imaging operator. Each row contained the concatenated time series for all 15 transducers corresponding to a position in object space. Therefore, the imaging operator had rows corresponding to the number of calibration grid points in object space and columns corresponding to the number of time points used to sample object space multiplied by the number of transducers used to collect the data. A de-noised imaging operator was constructed by removing the noise from the transducer responses prior to analysis. De-noising was performed by estimating the peak size, peak width and time of flight from the smoothed time series data. The peak size was found by locating the maximum in the time series data and the peak width estimated by differencing the location of the time points, which corresponded to half the value of the peak size. The time of flight was recorded as the temporal location of the peak. The parameters were then used to compute a synthetic time series consisting of zeros everywhere, except for the points representing the peak width centered upon the time of flight. These specific points were filled with a scaled and inverted parabola representative of the smoothed experimental time series. The inverted parabola is representative of the basis function used in the back projection

model of the reconstruction algorithm from our previous work, which closely resembles the velocity potential of the bipolar pressure signal. In this approach, the characteristic information of the bipolar wave is retained (amplitude, FWHM, time-of-flight). In order to backproject accurately, the velocity potential is used in order to retain this information and not cancel signal placed in voxels because of the negative lobe in the bipolar wave. The interference effects potentially present in an imaging task are still accurately measured in the forward model of the solution. The de-noised imaging operator was then constructed from these de-noised time series using the same method described above. The de-noised imaging operator then contained the same shift-variant response as the experimental imaging operator but with greatly reduced noise.

### ***3.2.3 Singular value decomposition and singular vector correlation***

Singular value decomposition of both imaging operators was performed in MATLAB® via the built-in singular value decomposition function (svds, MATLAB version 7.8.0). The orientation (positive or negative) of the resulting singular vectors is not necessarily the same between imaging operators and is relatively unimportant when interpreting the physical meaning of the singular vectors. The inner product of the experimental singular vectors and de-noised singular vectors in matrix  $\mathbf{V}^T$  was computed after the SVD of both imaging operators. Because singular vectors parallel and orthogonal to each other were expected to result in a value of one and zero, respectively, we interpreted the inner product result as a correlation between the two singular vectors.

### ***3.2.4 The crosstalk matrix***

The experimental voxel crosstalk matrix was computed by multiplying the transpose of the experimental imaging operator by the experimental imaging operator.



## 3.3 Results

### 3.3.1 Crosstalk sensitivity and aliasing

After the crosstalk matrix was calculated for the large volume scan, the main-diagonal was reshaped to represent the location of each voxel in object space (to facilitate straightforward visualization of the data) and was plotted in Fig. 3.2. The map in Fig. 3.2 visually illustrates the sensitivity of the transducer arrangement to signals originating from each voxel location in object space for the  $30 \times 30 \times 30 \text{ mm}^3$  scan ( $10 \times 10 \times 10$  voxels).

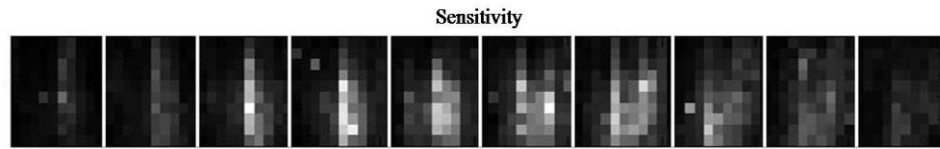


**Figure 3.2:** Displays sensitivity of the PA system at each location in object space acquired from the main-diagonal of the crosstalk matrix corresponding to the  $30 \times 30 \times 30 \text{ mm}^3$ . Both x and y axes represent voxel number in the y and z directions, respectively. Accordingly, each x-plane in object space is  $10 \times 10$  voxels. Grey scale represents normalized magnitudes from 0 (black) to 1 (white).

Figures 3.3(a) and 3.3(b) represent aliasing of signal originating at the center of the object space to all other voxel locations for the small and large scan, respectively. The voxel highlighted in Figs. 3.3(a) and 3.3(b) corresponds to the same location in object space (i.e. center point of object space). Figure 3.3(c) shows aliasing effects from a selected corner voxel to illustrate the shift-variant response of the PA system. The y-z plane in Figs. 3.3(b) and 3.3(c) is  $30 \times 30 \text{ mm}^2$  and is  $16 \times 16 \text{ mm}^2$  in Fig. 3.3(a). The aliasing information was retrieved by reshaping the rows of the crosstalk matrix (in the same manner as described for Fig. 3.2). For example, aliasing in the center voxel is visualized by plotting row 455 of the crosstalk matrix for the large scan.

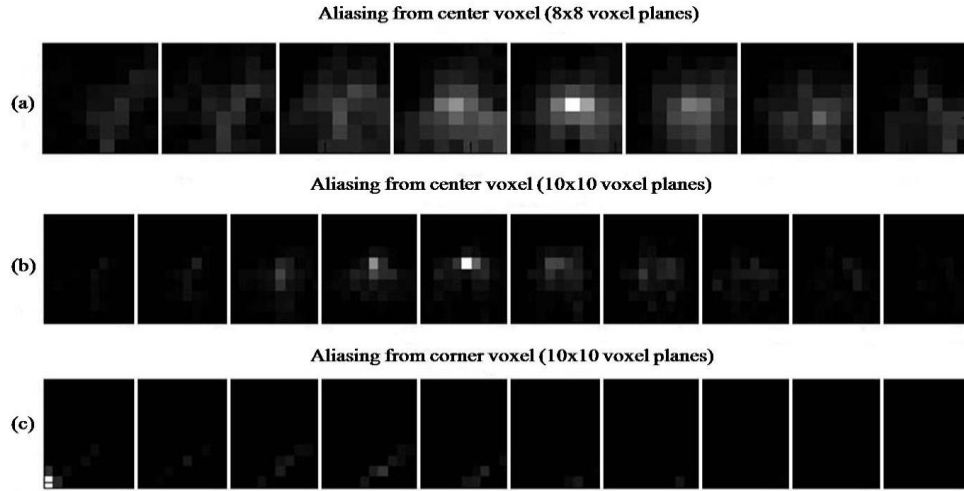


**Figure 3.3:** (a) Illustrates aliasing from the center voxel for the  $16 \times 16 \times 16 \text{ mm}^3$  scan (each x-plane is  $8 \times 8$  voxels) while (b) shows aliasing from the same position for the  $30 \times 30 \times 30 \text{ mm}^3$  scan (each x-plane is  $10 \times 10$  voxels). (c) Shows representative aliasing plots from a voxel located at the corner of the object space for the  $30 \times 30 \times 30 \text{ mm}^3$  scan (each x-plane is  $10 \times 10$  voxels).

### 3.3.2 Singular value decomposition: Singular vectors

The decomposition of the imaging operator yields a set of orthonormal singular vectors that describes both the projection and object space of the PA system. An additional imaging operator was produced to better understand the results of the SVD. A de-noised imaging operator was produced by modifying the experimental imaging operator according to the strategy outlined in section 2.2. The signals acquired at each voxel in object space were replaced with a parabola of the same peak, width, and time of flight as the experimental signals as well as zeros in all other temporal recordings in order to examine the effects of noise on the SVD of the imaging operator. Column vectors of matrix  $\mathbf{V}^T$  were organized in the same manner as the data in Fig. 3.2 in order to aid in visualization of the results. The data corresponding to the experimental imaging operator for the  $30 \times 30 \times 30 \text{ mm}^3$  scan are displayed in Fig. 3.4(a). The de-noised imaging operator derived from the experimental imaging operator is shown in Fig. 3.4(b). The center plane of object space was then plotted in both the de-noised and experimental decompositions.

The normalized singular vectors of the de-noised and experimental imaging operators were multiplied and summed in order to correlate the similarity of each corresponding set of singular vectors. The absolute value of the product is presented as the correlation. The results of the correlation are shown in Fig. 3.5(a). Four additional imaging operators were constructed with systematic noise added to the de-noised imaging operator at values of  $\frac{1}{4}$ ,  $\frac{1}{2}$ , 2, and 5 times the average system noise of the experimental imaging operator. The singular vectors of each imaging operator were again computed and projected onto the de-noised imaging operator values and resulted in data similar (but not shown) to that displayed in Fig. 3.5(a). In an ideal system, each set of singular vectors would correlate with a value of 1 while the multiplication of a singular vector with another singular vector in the basis would yield a value of 0 as the singular vectors would be orthogonal. The data in Fig. 3.5(a), as well as the correlation data not shown for the four additional imaging operators, were reordered and displayed in Fig. 3.5(b) to illustrate the correlation of singular vectors in descending order.

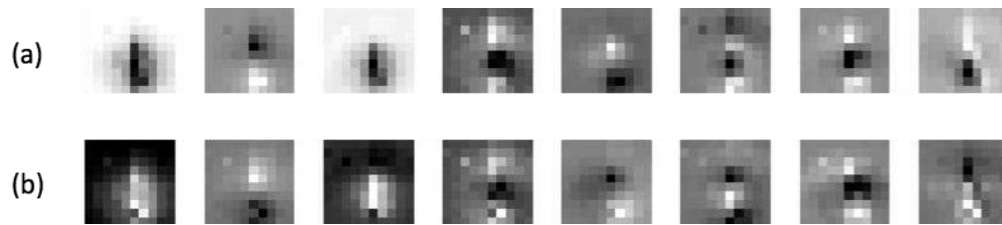


**Figure 3.4:** (a) and (b) Displays the center y-z plane of the first 8 singular vectors acquired via experiment and de-noised, respectively. The field-of-view for each singular vector is  $30 \times 30 \text{ mm}^2$ . The singular vector number reads from left to right with the leftmost image representing singular vector 1.

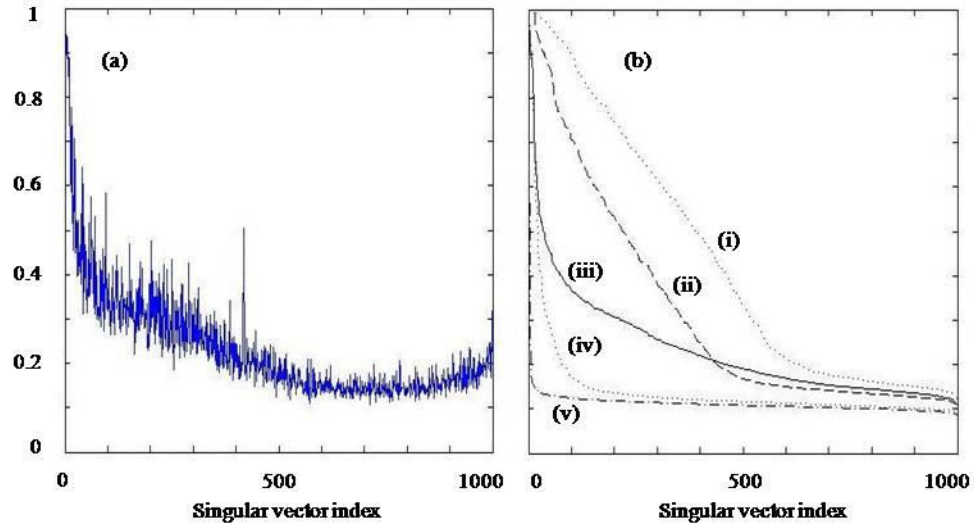


**Figure 3.5:** (a) Displays the correlation among the set of 1000 corresponding singular vectors in the de-noised and experimental matrices,  $\mathbf{V}^T$ . (b) Shows the same computation as in (a) but in descending order for an imaging operator with (i)  $\frac{1}{4}$  the intrinsic system noise, (ii)  $\frac{1}{2}$  the intrinsic system noise, (iii) the experimental imaging operator, (iv) 2 times the intrinsic system noise, and (v) 5 times the intrinsic noise. The singular vector index changed with the order as the true singular vector number (corresponding to the matrix  $\mathbf{V}^T$ ) was unknown after the initial projection operations were completed. The vertical axis in both (a) and (b) is shared.

## 3.4 Discussion

### 3.4.1 Crosstalk sensitivity and aliasing

As was demonstrated in an earlier publication [15], the sensitivity of the transducer array lacked uniformity through the object space specified by the field-of-view of the transducer array. Results presented in the previous publication illustrated only individual transducer sensitivities, which provided only minor insight into the overall system sensitivity (cumulative sensitivity) to object space when interpreted together. Furthermore, in the previous work, the individual transducer sensitivities were incorporated into the image reconstruction process to correct for potential non-uniformity in image contrast that might arise due to non-uniform transducer sensitivity to object space. Here, the cumulative sensitivity was obtained directly by means of the main

diagonal elements of the crosstalk matrix (Fig. 3.2) and confirmed the non-uniform sensitivity of the transducer array to object space. Although the cumulative sensitivity is not used for reconstruction purposes, it provides insight into the overall performance of the transducer array and can be used for optimization purposes (see below).

Figures 3.3(a) and 3.3(b) illustrate the aliasing from a similar location in object space. Because the step-size and volume of the defined object space is significantly different, the span of the aliasing effects appear more pronounced in Fig. 3.3(a). However, the span of aliasing measured as the FWHM of the highlighted voxel is similar in both maps. The aliasing in  $x$ ,  $y$ , and  $z$  is approximately equal for Figs. 3.3(a) and 3.3(b), respectively. In general, the aliasing contributions in object space are not isotropic because the PA system is shift-variant, which is evident when comparing aliasing from a centre voxel (Fig. 3.3(b)) to a corner voxel (Fig. 3.3(c)). If we recall the process for calculating the crosstalk matrix, there are two independent contributions that lead to aliasing in object space. The signal from one voxel into another is influenced by both the extent of the overlapping temporal region among the two voxels as well as the shape of the expansion functions generated by the two voxels in the overlapping temporal region. For example, measured data generated from voxels in object space may possess a relatively small temporal overlap but could still contain large aliasing effects if the shape of the expansion functions in the overlapping region contains a relatively large area under the curve. This would result in a high crosstalk among voxels with relatively small temporal overlap. In our previous work, the backward model used during image reconstruction to compute the distribution of sources in object space accounted for the non-uniformity in transducer sensitivity, but assumed a symmetric expansion function. Accordingly, the aliasing effects expected in reconstructed images will not precisely correspond to that displayed in the crosstalk matrix.

Because of the shift-variant nature of the PA system, it is inaccurate to obtain global estimates of resolution and contrast via the crosstalk calculation. However, general behaviors of the system performance can be visualized and qualitative characterizations can be made. Qualitative metrics computed from the crosstalk matrix could potentially

be used to change the placement of transducers in the array to reduce aliasing and enhance system performance. The aliasing effects computed via the crosstalk matrix are inherent to this PA system based on the frequency response of the transducers used as well as the relative position of the object space to the transducer arrangement. Opting for transducers of higher centre frequency would limit the aliasing effects seen but would fundamentally change the system performance in other, negative ways, such as reducing the penetration depth of the acoustic waves. To reduce aliasing effects to a practical limit, a greater number of transducers need be introduced to diminish the consequences of aliased signal.

### ***3.4.2 Singular value decomposition***

Recall the method for producing the de-noised imaging operator. Only the system noise was reduced after acquiring the imaging operator. It is clear that a strong correlation should exist between singular vectors of the same order when comparing the de-noised and experimental imaging operator provided the system noise has a minor effect on the imaging operator. In the case where the noise has a small effect on the geometry of the singular vector, it is expected that the correlation between the two singular vectors approaches one. However, when the system noise is significant, the correlation among singular vectors will be reduced considerably. In a mathematical context, the correlation between differing singular vectors should be zero because the basis of decomposed singular vectors is orthonormal. However, this relationship is not seen in practice due to system noise. The SVD of the imaging operator presents the singular vectors in ascending order of the corresponding singular value in matrix  $\mathbf{S}$ . Therefore, there is potential for the system noise in the experimental imaging operator to impact the order of the decomposed singular vectors such that comparison of singular vectors of the same order will not necessarily represent a comparison of singular vectors of corresponding geometry. At some threshold, the impact of system noise is too significant for the system to accurately resolve the geometry of the singular vector and consequently the affected singular vector contributes no useful information when attempting to recover an object.

The correlation of the experimental singular vectors to the singular vectors obtained from the de-noised imaging operator is shown in Fig. 3.5(a). As expected, the lower order singular vector pairs had a high correlation (as high as 0.98 for the first pair of singular vectors), but the correlation dropped quickly as the order of the singular vector increased. Although the purpose of the plot was to gain insight into the number of measurable singular vectors, selection of a threshold correlation that delineated the number of measurable singular vectors was not obvious. For example, the distribution of correlation values appeared to have at least two components with points of inflection at indices 100 and 600. To better understand the sensitivity of the correlation distribution to measurable singular vectors, we compared the experimental findings to correlation values obtained from pairs of singular vectors, where defined amounts of noise were introduced into the imaging operator (i.e. de-noised imaging operator and the de-noised imaging operator with noise added back). The correlation distributions were reordered in descending order and displayed in Fig. 3.5(b) to facilitate interpretation. Curves (i) and (ii) in Fig. 3.5(b) were derived from imaging operators with less system noise (1/4 and 1/2, respectively) than the experimental imaging operator and consequently had a broader correlation distribution. Curves (iv) and (v) in Fig. 3.5(b), generated with 2 and 5 times the experimental noise, respectively, displayed a narrow correlation distribution. Taken together, the curves suggested that a correlation of 0.2 represented a reasonable threshold for delineating the number of measurable singular vectors due to the presence of a clearly defined inflection point below this correlation value for curves (i, ii, iv, and v). Therefore, we concluded that approximately 400 measurable singular vectors were present for the experimental imaging operator (using a 0.2 correlation threshold in Fig. 3.5(a)).

Although it is generally the goal of any imaging system to resolve as many singular vectors as possible, it should be emphasized that not all imaging tasks necessarily require a large number of measurable singular vectors to resolve objects in the field of view. This is illustrated by considering two canonical examples. (i) If the PA system is to macroscopically localize a spherical tumor mass in soft tissue, it may suffice to have a system that resolves a small number of singular vectors (perhaps several

hundred) since the task is to reconstruct a single object of low morphological complexity within the field of view of the imaging system. (ii) A more complicated PA imaging task such as delineating microvasculature within a small animal may require many measurable singular vectors (perhaps several thousand) since many objects of complex morphology will be present in the field of view.

### ***3.4.3 Computation considerations***

It is important to note a practical shortcoming concerning the computation of both the crosstalk matrix and singular value decomposition. That is, the computation required to compute the associated matrices can be lengthy. The computation of the crosstalk matrix using the imaging operators was not intensive (because of the relatively small temporal domain, voxel number, and transducer count) while the computation of the SVD matrices with 1000 singular values required 53 minutes (Dell T7400 workstation: Dual Intel® Xeon® X5472 3.00 GHz, 8 GB Ram, Windows Vista-64). However, this could be a limiting factor for other PA systems that utilize a larger temporal domain, voxel number, and transducer count. It should be stressed that these computations need only be completed once to extract the required information.

### ***3.4.4 Imaging considerations***

In order to determine whether or not an imaging task fails or succeeds, an object described by the cubic voxel expansion function should be projected onto the set of computed singular vectors in the matrix  $\mathbf{V}^T$ . The fidelity with which the image is produced indicates the capability of the imaging system to fundamentally capture the information contained in the object. However, whether or not the task succeeds or fails is necessarily subjective based on the required task of the imaging system.

The link between crosstalk and SVD is important. While it is the SVD matrices that are directly responsible for producing an image from a measured set of data, it is the



crosstalk matrix that provides insight in addressing why an imaging task failed or succeeded. It is the expansion coefficients describing an object that must be resolved in order to accurately capture the information when performing an imaging task. The capability of the system to do this is intrinsically contained within the SVD matrices; however, it is the crosstalk matrix that actually quantifies the spatially-dependent overlap of expansion coefficients (aliasing). If an imaging system subjectively fails an imaging task, the aliasing contribution extracted from the crosstalk matrix can be assessed and the imaging system can be improved where necessary.

### **3.5 Conclusion**

A technique was developed to acquire a data set that described an imaging operator for a PAI system. Two scans were completed. The first contained a step size of 2 mm within an object space of  $16 \times 16 \times 16 \text{ mm}^3$ . The second was completed at a step size of 3 mm within an object space of  $30 \times 30 \times 30 \text{ mm}^3$ . Utilizing these data, computations to produce a voxel-based crosstalk matrix were made in order to characterize the spatially dependent sensitivity and aliasing. The lack of uniformity in the sensitivity confirmed the findings of our previous work. Singular value decomposition analysis was performed on the imaging operator to provide insight into the system's sensitivity to objects of complex geometry. As well, insight was provided regarding the sensitivity of the imaging operator to noise. Ultimately, both techniques provided information that could be used to understand any PA system and could provide a means to improve future iterations of the imaging hardware.

### **3.6 References**

1. M. Xu, and L. V. Wang, "Photoacoustic imaging in biomedicine," *Rev. Sci. Instrum.* **77**(4), 041101 (2006).

2. T. Lu, J. Jiang, Y. Su, R. K. Wang, F. Zhang, and J. Yao, Photoacoustic imaging: Its current status and future development” in *4th International Conference on Photonics and Imaging in Biology and Medicine, September 03,2005 - September 06* (SPIE), National Natural Science Foundation of China; SPIE Russia Chapter; Int. Laser Center of M.V. Lomonosov Moscow State Univ.; Bio-optics and Laser Medicine Comm. of Chinese Optics Soc.; Science and Techn. Garden of Tianjin University, China.
3. G. J. Diebold, T. Sun, and M. I. Khan, “Photoacoustic monopole radiation in one, two, and three dimensions,” *Phys. Rev. Lett.* **67**(24), 3384–3387 (1991).
4. G. Paltauf, J. A. Viator, S. A. Prah, and S. L. Jacques, “Iterative reconstruction algorithm for optoacoustic imaging,” *J. Acoust. Soc. Am.* **112**(4), 1536–1544 (2002).
5. P. Liu, “The P-transform and photoacoustic image reconstruction,” *Phys. Med. Biol.* **43**(3), 667–674 (1998).
6. C. G. A. Hoelen, and F. F. de Mul, “Image reconstruction for photoacoustic scanning of tissue structures,” *Appl. Opt.* **39**(31), 5872–5883 (2000).
7. D. Frauchiger, K. P. Kostli, G. Paltauf, M. Frenz, and H. P. Weber, Optoacoustic tomography using a two dimensional optical pressure transducer and two different reconstruction algorithms” in *Hybrid and Novel Imaging and New Optical Instrumentation for Biomedical Applications, June 18,2001 - June 21* (SPIE), 74–80.
8. M. Xu, and L. V. Wang, “RF-induced thermoacoustic tomography” in *Proceedings of the 2002 IEEE Engineering in Medicine and Biology 24th Annual Conference and the 2002 Fall Meeting of the Biomedical Engineering Society (BMES / EMBS), October 23,2002 - October 26* (Institute of Electrical and Electronics Engineers Inc), 1211–1212.

9. K. P. Kostli, D. Frauchiger, J. J. Niederhauser, G. Paltauf, H. P. Weber, and M. Frenz, "Optoacoustic imaging using a three-dimensional reconstruction algorithm," *IEEE J. Sel. Top. Quantum Electron.* **7**(6), 918–923 (2001).
10. P. Ephrat, L. Keenliside, A. Seabrook, F. S. Prato, and J. J. L. Carson, "Three-dimensional photoacoustic imaging by sparse-array detection and iterative image reconstruction," *J. Biomed. Opt.* **13**(5), 054052 (2008).
11. D. Modgil, M. A. Anastasio, and P. J. La Riviere, "Photoacoustic image reconstruction in an attenuating medium using singular value decomposition" in *Photons Plus Ultrasound: Imaging and Sensing 2009* (SPIE – The International Society for Optical Engineering), 71771B (7 pp.).
12. D. W. Wilson, and H. H. Barrett, "Decomposition of images and objects into measurement and null components," *Opt. Express* **2**(6), 254–260 (1998).
13. P. Ephrat, and J. J. L. Carson, "Measurement of photoacoustic detector sensitivity distribution by robotic source placement" in *9th Conference on Photons Plus Ultrasound: Imaging and Sensing 2008, January 20, 2008 - January 23* (SPIE), Society of Photo-Optical Instrumentation Engineers (SPIE).
14. P. Ephrat, M. Roumeliotis, F. S. Prato, and J. J. Carson, "Four-dimensional photoacoustic imaging of moving targets," *Opt. Express* **16**(26), 21570–21581 (2008).
15. M. Roumeliotis, P. Ephrat, J. Patrick, and J. J. L. Carson, "Development and characterization of an omnidirectional photoacoustic point source for calibration of a staring 3D photoacoustic imaging system," *Opt. Express* **17**(17), 15228–15238 (2009).
16. H. H. Barrett, J. L. Denny, R. F. Wagner, and K. J. Myers, "Objective assessment of image quality. II. Fisher information, Fourier crosstalk, and figures of merit for task performance," *J. Opt. Soc. Am. A* **12**(5), 834–852 (1995).

17. A. A. Oraevsky, V. G. Andreev, A. A. Karabutov, and R. O. Esenaliev, Two-dimensional opto-acoustic tomography transducer array and image reconstruction algorithm,” Proc SPIE Int Soc Opt Eng **3601**, 256–267 (1999).

## Chapter 4:

### *Singular value decomposition analysis of a photoacoustic imaging system and 3D imaging at 0.7 fps*

This chapter is based on a research paper published in the June 2011 issue of Optics Express. Brief citation as follows: **M. Roumeliotis**, R.Z. Stodilka, E. Ng, J.J.L. Carson. “Estimate of effective singular values for a photoacoustic imaging system of varying transducer arrangement and sampling rate”, Optics Express **19**(14), pp. 13405-13417, June 2011.

This chapter includes the criterion by which matrix rank was identified in an imaging operator analyzed by singular value decomposition. The results are then used to execute a regularized pseudoinverse solution to the linear system model. This approach is utilized in order to perform image reconstruction on both simulated and experimental objects. In the experimental case, the software process is streamlined such that the imaging task can be performed in real-time, at a 0.7 fps.

## 4.1 Introduction

### *4.1.1 Background*

Photoacoustic imaging (PAI) is a dual imaging modality that makes use of the contrast inherent to optical imaging techniques as well as the penetration depth and resolution of ultrasound techniques [1]. This is accomplished through illumination of optically absorbing objects with non-ionizing radiation generated from a pulsed laser. The optical energy is deposited rapidly, satisfying thermal and stress confinement conditions, which facilitates thermo-elastic expansion of the absorbing structure leading to an outwardly propagating transient bipolar pressure wave [2]. Characteristic information of the absorbing structures, including location, size, shape, and optical

properties, is encoded in the propagating pressure waves [3]. Using time-domain measurements, photoacoustic images can be produced using a variety of reconstruction algorithms [4-9].

In an earlier publication, we introduced a technique that experimentally measured a matrix that represented the imaging operator for a photoacoustic imaging system [10]. Metrics intended to aid in the analysis of the imaging operator were then computed to provide information related to system performance. Among the techniques used was singular value decomposition (SVD). In a general context, the SVD technique provides information regarding the geometry of objects that can be accurately captured by an arrangement of transducers from a specified object space. This information is especially important when collecting a small number of data projections since the limited data will inevitably reduce the complexity of objects that can be accurately represented. This is the case with the staring, sparse-array PAI system described by our group [11-13].

While the previous work was important in introducing the process of experimentally acquiring the imaging operator, it did not address detail with respect to the number of object space singular vectors that can be reliably recovered and the impact these singular vectors directly have on image quality. This is vitally important as these singular vectors strictly determine the complexity of objects that can fundamentally be represented by a reconstruction algorithm, irrespective of the specific merits of the reconstruction technique. As well, the acquisition of an experimental imaging operator enables reconstruction of PA images to be computed directly by solving a linear system model, which translates time-dependent pressure measurements to an estimate of the object. In this paper, we examine the consequence of both variable transducer count and measurement space temporal sampling rate on the capability of the PA imaging system to reconstruct arbitrary objects in the object space. As well, a specific arrangement of transducers and measurement space temporal sampling rate is utilized to perform real-time imaging of a point source as it is translated through object space. In order to produce accurate and fast PA images, it is critical the effect of both transducer count and temporal sampling rate are understood in order to capture an imaging operator with only the

precisely required information. It is these parameters that directly determine the number of elements in the imaging operator. As a consequence, improper sampling of the object space can lead not only to infidelity in image reconstruction but also increased computation speed.

### ***4.1.2 Singular value decomposition***

Singular value decomposition provides a significant portion of the work in this chapter. For details, please refer to section 1.5.3.

### ***4.1.3 Estimate of effective singular values***

Upon decomposing the imaging operator, the vectors provided in  $\mathbf{V}^T$  are linearly independent. However, by examining the associated magnitude of the singular values in matrix  $\mathbf{S}$ , it is clear not all vectors contribute equally to the overall system response. In fact, some do not effectively contribute at all to the reconstruction of an object [14]. It is the matrix rank (number of linearly independent rows) of the imaging operator that indicates the singular vectors that contribute usefully to image reconstruction. A number of techniques have been proposed to determine the rank of a matrix in the context of a real imaging operator [15-17]. Konstantinides et al. used a statistical model based on the signal-to-noise ratio of a measured imaging operator. The technique proved to be very accurate in determining the rank of the matrix.

As referenced in [15], a single criterion can be used to evaluate the effective rank of the imaging operator. Mathematically represented by:

$$\alpha_t \gg \alpha_{t+1} \quad (4.1)$$

where  $\alpha$  represents the magnitude of the singular value and  $t$  is the effective rank of the matrix. While this threshold is seemingly subjective, it can be evaluated more precisely by stating the rank of the matrix is estimated to be equal to  $t$ , if:

$$\frac{\alpha_t}{\alpha_{t+1}} = \max\left(\frac{\alpha_j}{\alpha_{j+1}}\right), j = 1, 2, \dots, M \quad (4.2)$$

Via the results of [15-17], it is clear that in an experimental imaging operator the singular values in  $\mathbf{S}$  become exceedingly small when the remaining columns of  $\mathbf{V}^T$  do not contribute useful information about object space.

An estimate of the effective number of singular vectors that contribute usefully to image reconstruction is critical when the image reconstruction is performed by solving directly for the vector  $\mathbf{f}$ . In this paper, the SVD of the imaging operator,  $\mathbf{H}$ , was computed and utilized to compute a regularized pseudoinverse solution. The regularized solution utilized only the singular values and associated singular vectors that were identified as corresponding to useful information as described above.

#### ***4.1.4 Experimental objective***

We previously reported on a method to acquire a matrix that represented the imaging operator of a 3D photoacoustic imaging system [10,13]. At each point in object space, the amplitude, duration, and time of flight of the pressure wave were recorded for each transducer. This provided the foundation of the imaging operator, which described the system response to a point source for each transducer at each location in object space. Due to technological limitations, the previous calibration scan did not optimally cover the entire object space at a step-size on the order of the system resolution. It was necessary to improve the data acquisition rate in order to facilitate a calibration scan with many more points in object space. In our present study, we have augmented the PA system to now include a total of 30 transducers.

Once the dense calibration scan was acquired, subsets of the transducer arrangement could be generated. The imaging operators contained the full set of 30 transducers or subsets with 25, 20, 15, 10 or 5 transducers. Similar subsets of the experimental imaging operator were created with different measurement space temporal sampling rates with a constant count of 15 transducers. The SVD of each imaging



operator was subsequently computed. Different imaging operators were compiled from the same calibration scan in order to eliminate variability between scans. This approach had the added benefit that any variation in matrix rank was due solely to the arrangement, number of transducers, or sensitivity of the transducers contributing to each imaging operator.

## 4.2 Methods

### *4.2.1 Photoacoustic imaging system*

The imaging system was consistent with the experimental setup referred to in our earlier publication [10]. Data acquisition was accomplished with 2 custom-built 16-channel preamplifier cards electronically connected to 4 custom-built 8-channel data acquisition cards held within the same chassis. A total of 32 channels collected data (30 transducers, 1 photodiode, 1 channel was unused). Data acquisition, transfer to the PC, image reconstruction and display was controlled with a custom application developed within National Instruments Labview<sup>TM</sup> v8.5. The imaging system utilized a total of 30 ultrasound transducers (model V304, 1" diameter, 2.25 MHz with fractional bandwidth of 65%, *Panametrics-NDT*, Waltham, Massachusetts) in a staring hemispherical arrangement. Transducers were mounted on custom frames, each supporting 3 transducers at evenly spaced azimuthal angles ( $36^\circ$  between columns). Fifteen (15) of the transducers were mounted on frames with zenith angles of  $22.5^\circ$ ,  $45^\circ$ , and  $67.5^\circ$ . The remaining 15 transducers were mounted on frames placed azimuthally between the original frames, at zenith angles of  $33.75^\circ$ ,  $56.25^\circ$ , and  $78.75^\circ$ . A schematic of the transducer array is shown in Fig. 4.1(a).

### *4.2.2 System calibration scan*

As in section 4.2.1, the calibration arrangement was developed in an earlier publication and is cited here for reference [10]. The calibration scan was completed with

a  $30 \times 30 \times 30 \text{ mm}^3$  object space and 1.5 mm step-size for a total of 8,000 voxel locations. It was originally intended to complete scans of varying voxel count and step-size. However, calibration scans exceeding 8,000 voxels represented the practical limit of our experimental methodology. For the experimental image reconstruction, a second scan of dimension  $16 \times 16 \times 7 \text{ mm}^3$  was produced with 30 transducers at a measurement space temporal sampling rate of 10 MHz.

### ***4.2.3 Singular value decomposition***

The processed photoacoustic time series were compiled to produce a matrix representative of the imaging operator. For a given voxel, the time series recorded by each transducer were concatenated to produce one row in the matrix. Therefore, a single imaging operator contained rows equal to the number of voxels in the scan (8,000) and columns equal to the number of transducers multiplied by the number of time points used to record the photoacoustic data.

Singular value decomposition of both imaging operators was performed in MATLAB® (The Mathworks™, Inc., version 7.8.0, Natick, Massachusetts) via the built-in singular value decomposition function (svds). A technical limitation was reached with large imaging operators. Specifically, as the size of the matrix approached 10 GB, decomposition by SVD in MATLAB failed due to the available memory in the workstation. As a work-around, we employed a 10-point average to reduce the dimensions of the measurement space by 10-fold. Imaging operators acquired at this temporal sampling rate (5 MHz) were used to compare the change in matrix rank as the transducer count was varied. Afterward, one particular arrangement of 15 transducers was selected and an n-point average was applied to examine the effects of measurement space temporal sampling rate on the matrix rank.

### ***4.2.4 Regularized pseudoinverse image reconstruction***

Image reconstruction was performed by solving directly for the vector  $\mathbf{f}$ . The SVD component matrices were used to represent the imaging operator in solving for the vector  $\mathbf{f}$ . The built-in MATLAB function (`pinv`) was used to compute the pseudoinverse of the matrix  $\mathbf{S}$ , referred to as  $\mathbf{S}^+$ . Due to noise and a relatively high condition number associated with the imaging operator, regularization of the singular values was necessary. Truncated regularization was performed corresponding to singular values with indices greater than 90 percent of the computed matrix rank being set to zero when computing  $\mathbf{S}^+$ . The pseudoinverse was then multiplied by the data set measured experimentally in  $\mathbf{g}$ , yielding an estimate of the object  $\mathbf{f}$ .

A second reconstruction technique was used for basis of comparison on a single system setup (30 transducers, 5 MHz). This technique was an iterative algebraic reconstruction technique, which estimated the image by computing the difference between the data set,  $\mathbf{g}$ , and the right side of Eq. (1.18), which was then added to a master of the image. While this model is computationally expensive, it was deemed instructive to show the results of the simulated data sets being reconstructed via another approach.

#### ***4.2.5 Real-time photoacoustic imaging***

The robot used to perform the calibration scan was also used to translate the optical fiber (photoacoustic point-like source) through the object space of the PA imaging system at a speed of 0.40 mm/s during an imaging experiment. One image of the point-like source was captured every 1.4 s. The interval time represented a practical limit related to the laser pulse duration (9 ns), the data acquisition time (100  $\mu$ s), the time taken to trigger and transfer 32 channels of data from the 4 DAQ cards to the PC (~1.2 s), and the time taken to perform the matrix multiplication, archive the data to disk, and display the data to PC screen (~0.2 s). Three slices of the 3D image data ( $xy$ ,  $xz$  and  $yz$ ) were displayed on the workstation after every image reconstruction and before the next laser pulse. Repeated laser pulses resulted in a 3D photoacoustic movie (i.e. real-time 4D photoacoustic imaging).

## 4.3 Results

### *4.3.1 Estimate of matrix rank*

The PA system is shown in Fig. 4.1(a) while an unfolded representation of the transducer arrangement shown in Fig. 4.1(b). The schematic shown in Fig. 4.1(b) was used to describe the varying transducer arrays for which matrix rank was computed. Each plane (P1 through P6) of Fig. 4.1(b) represents the transducers at the same zenith elevation. The results of the matrix rank estimate (based on Eq. (4.2)) are summarized in Fig. 4.1(c). The raw data - a semi-logarithmic plot of the magnitude of the singular values versus singular value index for each of the transducer arrangements - is shown in Fig. 4.1(d). It is evident in Fig. 4.1(d) that an abrupt decline in singular value magnitude is present in each of the six curves.

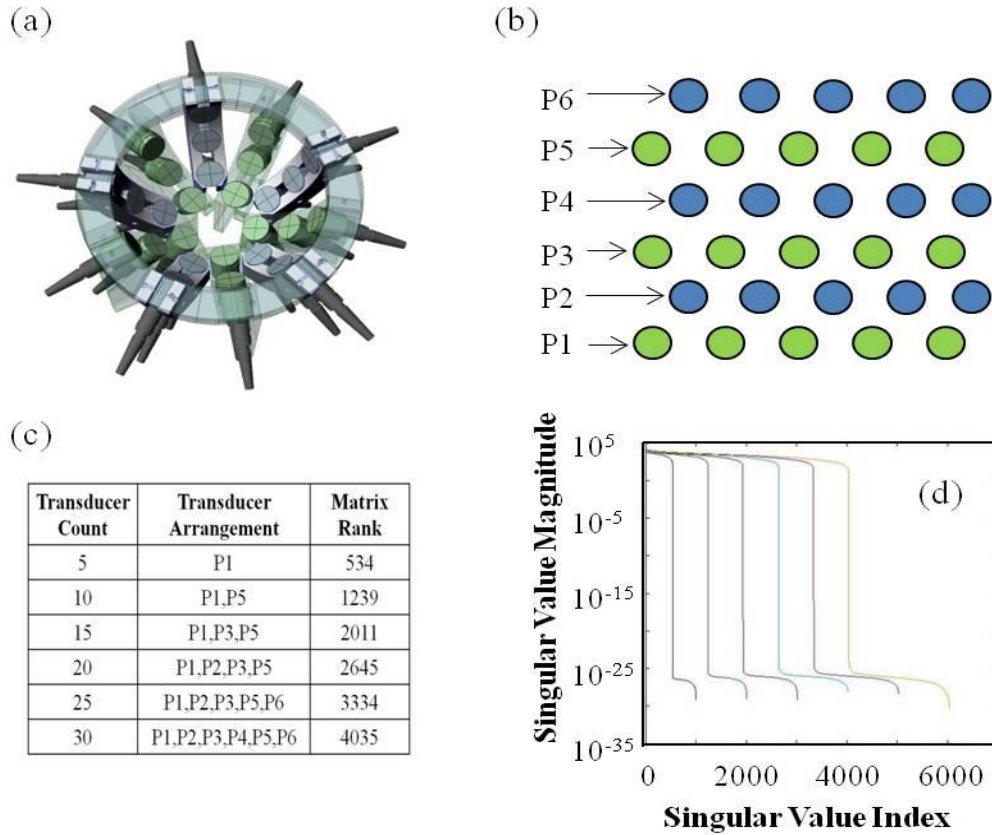


**Figure 4.1:** (a) Isometric view of the hemispherical PA imaging array illustrating the transducer arrangement. Columns with transducers lightly shaded in green correspond to zenith angles of 22.5°, 45°, and 67.5° while columns with transducers lightly shaded blue correspond to zenith angles of 33.75°, 56.25°, and 78.75°. (b) Represents an unfolded schematic of (a) whereby each plane of 5 transducers is referenced P1 through P6, with P1 representing the bottom-most row and P6 the top-most row. (c) Summarizes the results of the estimate of effective matrix rank on the 6 different transducer arrangements. (d) Semi-logarithmic plot of the magnitude of the singular values versus singular value index for each of the 6 transducer arrangements. Left-most curve corresponds to the 5 transducer imaging operator while right-most to the 30 transducer imaging operator with intermediate curves representing increasing transducer count from left to right.

The results shown in Fig. 4.1(c) and 4.1(d) are summarized and plotted in Fig. 4.2(a). An analysis similar to that shown in Fig. 4.1(d) was performed to estimate the matrix rank on imaging operators with variable measurement space temporal sampling rate (raw data not shown). Imaging operators were produced with measurement space temporal sampling rates of 25, 12.5, 10, 5, 2.5, 1.25, 1 and 0.5 MHz, all with the 15 transducer arrangement according to the setup described in Fig. 4.1(c). The matrix rank

was then estimated for each of the 8 temporal sampling rates and plotted in Fig. 4.2(b). Three (3) distinct regions are outlined in Fig. 4.2(b) by the dotted lines. Area (i) is the region where the system is undersampled (according to the Nyquist criterion and an estimate of the system resolution). Area (ii) corresponds to the sampling regime that meets the Nyquist criterion and where the object space dimension is greater than the measurement space dimension. Finally, area (iii) describes a region where the Nyquist criterion is met and the measurement space dimension exceeds the object space dimension. To further clarify the effective matrix rank estimate in Fig. 4.2(b), linear regression analysis was performed on the data contained within region (ii). A clear linear trend is shown in both plots with both coefficients of determination greater than or equal to 0.999. While this trend was expected, it is confirmed here experimentally for a photoacoustic imaging system with low transducer count. To emphasize the non-linear behavior of the matrix rank in region (i) and (iii), Fig. 4.2(c) shows a plot of the residual errors for each temporal sampling rate. Residual error was computed by comparing the expected matrix rank (based on the slope in Fig. 4.2(b)) to the measured matrix rank (estimated using Eq. (4.2)). Finally, sample singular vectors are plotted in Fig. 4.2(d) for the imaging operator of 30 transducers and 5 MHz temporal sampling rate. Each image depicts the centre plane of singular vector 1, 10, 3632, and 4036 for image (i) through (iv), respectively. Images (i) and (ii) were selected to show discernable geometry in the singular vectors at low orders, while (iii) corresponds to the singular vector at 90% of the matrix rank, and (iv) shows the vector at one index beyond the matrix rank.

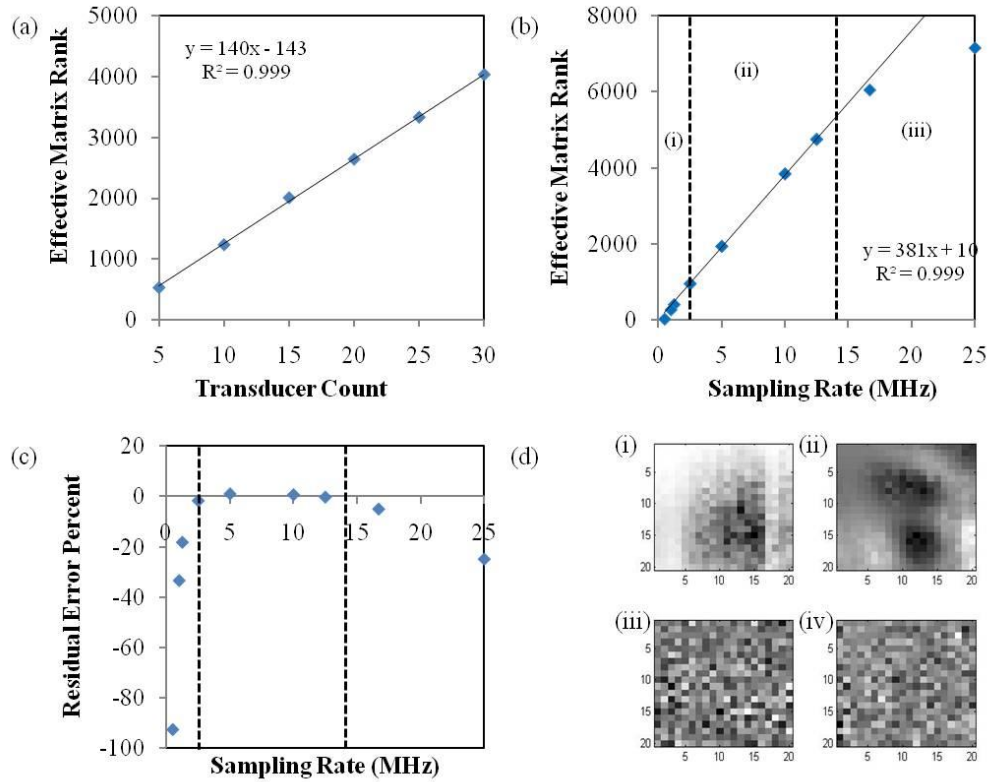


**Figure 4.2:** (a) Displays the estimated matrix rank for variable transducer count and arrangements. (b) Displays the estimated matrix rank for variable measurement space temporal sampling rates. Linear regression for (b) was performed only on the 4 data points contained within region (ii). The line is shown throughout the entire figure to show the expected value of the matrix rank. (c) Compares the expected matrix rank to the measured rank and is plotted as a percent error to highlight the deviation from linearity in regions (i) and (iii). (d) Provides a visual interpretation of the geometry associated with selected singular vectors for the imaging operator corresponding to the 30 transducer, 5 MHz temporal sampling rate. Images (i) through (iv) correspond to singular vectors of index 1, 10, 3632, and 4036.

### 4.3.2 Image reconstruction of objects with different transducer count

Three (3) separate objects were created and used as phantoms to be reconstructed using the technique outlined in Section 4.2.4. A point, line, and multi-point source were created using experimental data acquired during the calibration scan and the linear superposition principle. However, in order to avoid reconstructing data directly from the imaging operator, realistic system noise (normally distributed) was added to the data set,

$\mathbf{g}$ , to produce unique data. These time-dependent pressure measurements were then multiplied by the pseudoinverse obtained from component matrices ( $\mathbf{U}^T$ ,  $\mathbf{S}^+$ ,  $\mathbf{V}$ ) for each transducer count. Figure 4.3 shows the centre  $z$ -plane of the image reconstruction of each of the sources as a function of transducer count. The second column from the right shows the results of the iterative reconstruction technique applied to each of the 3 object types. A phantom of the objects is displayed in the right-most column.

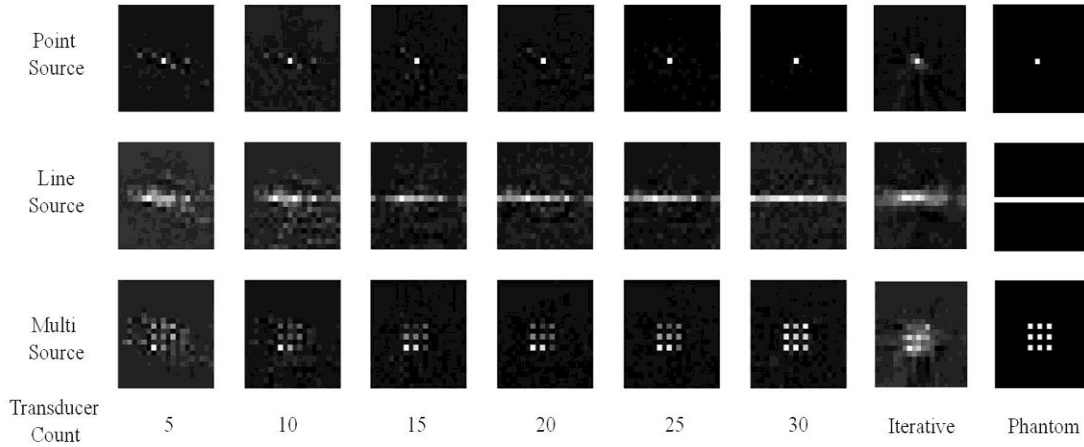


**Figure 4.3:** Reconstruction of a simulated point, line, and multi-point source for each of the 6 transducer arrangements. The iterative technique was implemented on the system with 30 transducers and 5 MHz temporal sampling rate (shown in the column second from right). Ideal image based on phantom is shown in the right-most column.

### ***4.3.3 Image reconstruction of objects with different measurement space temporal sampling rate***

The same objects used in Section 4.3.2 were again used as the experimental objects to reconstruct by the pseudoinverse of imaging operators (15 transducers) with variable measurement space temporal sampling rate. The result of the image reconstruction for each of the 8 temporal sampling rates (and phantom) is shown in Fig. 4.4.



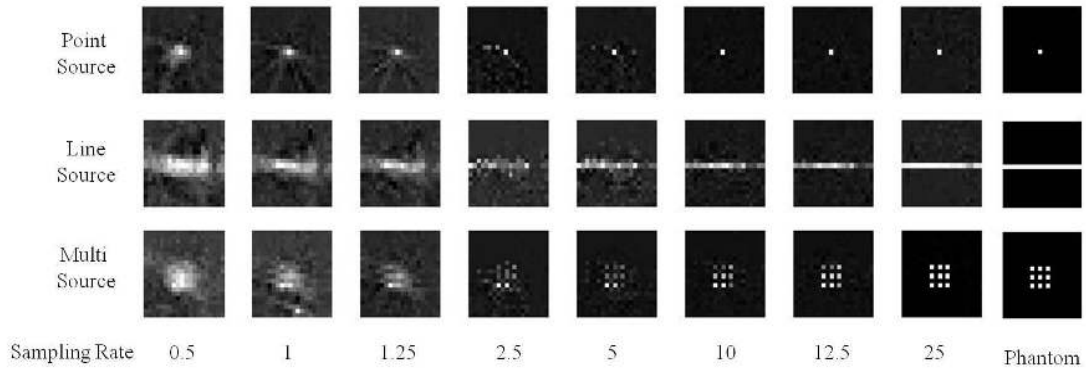


**Figure 4.4:** Reconstruction of a simulated point, line, and multi-point source for each of the 8 measurement space temporal sampling rates (MHz).

#### ***4.3.4 Image reconstruction of a point source in real-time (1.4 seconds per frame)***

The photoacoustic point-like source was imaged in 3D at 1.4 seconds intervals. Visual display of the point source is shown in Fig. 4.5 with each of the three orthogonal planes represented to illustrate the 3D nature of the image reconstruction process. The source had a starting position (10 mm, 11 mm, 4 mm) and was translated to position (6 mm, 11 mm, 4 mm).

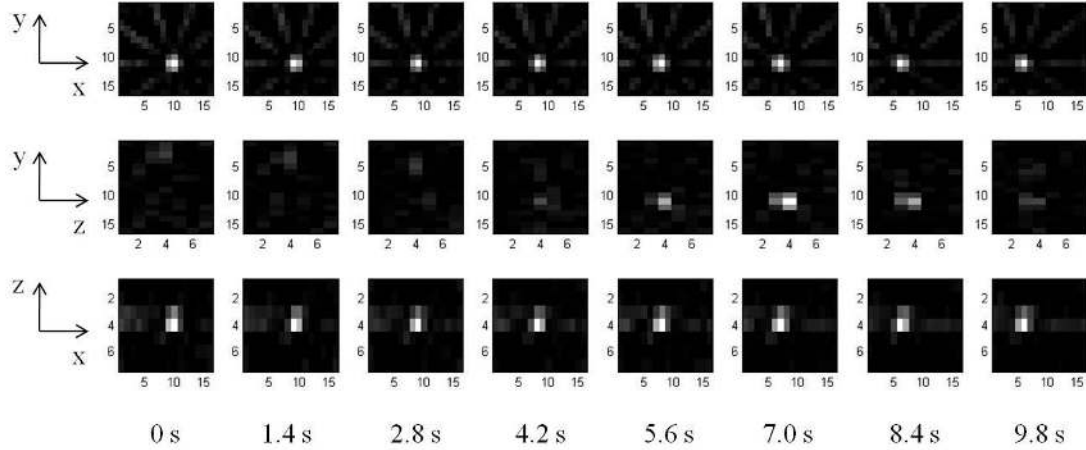


**Figure 4.5:** 4D real-time photoacoustic imaging experiment where data acquisition and image reconstruction were performed in real time. Images were captured from a photoacoustic point-like source translated in the negative  $x$ -direction at a velocity of 0.40 mm/s. The interval between 3D photoacoustic images was 1.4 s and rate-limited by the data acquisition transfer speed, computational, and data storage overhead. The first row shows an  $xy$ -plane ( $z = 4$  mm). The second row shows the same reconstruction in a  $zy$ -plane ( $x = 7$  mm) and the third row displays an  $xz$ -plane ( $y = 11$  mm). Each column represents the 3D image data acquired at a specific point in time (indicated along bottom).

## 4.4 Discussion

### 4.4.1 Estimate of matrix rank

The criterion in Eq. (4.2) worked well at producing a reliable estimate of the matrix rank. The ratio between consecutive singular values at the index of the matrix rank threshold was much greater than any other consecutive singular values. For example, the 30 transducer imaging operator had a maximum ratio of approximately 12 orders of magnitude while the ratio of any other 2 sequential singular values was never greater than 2 orders of magnitude. This was also seen in each of the 8 imaging operators with variable measurement space temporal sampling rate examined. Using Eq. (4.2), the effective matrix rank of the imaging operators obtained from a collection of transducer arrays of differing transducer count very closely followed a linear trend, as expected. In both Fig. 4.2(a) and 4.2(b), the slope estimated by the linear regression indicates the increase in matrix rank per change in transducer count and temporal sampling rate,

respectively. While this is an important parameter, it does not translate directly to an improvement in image quality that would result from such an increase in singular vector count, as this would be dependent on the object being captured by the imaging system.

The results acquired by varying the measurement space temporal sampling rate were unexpected at the onset. The same linear increase in matrix rank was found as the temporal sampling rate increased. However, the linear trend was only observed in region (ii) of Fig. 4.2(b) for temporal sampling rates from 2.5 MHz to 12.5 MHz. As estimated in a previous publication, the approximate resolution of the system is on the order of 1-2 mm [18]. According to Oraevsky et al. [19], the minimum temporal sampling rate required to capture information at a spatial scale of 1 mm is approximately 2.25 MHz. The two temporal sampling rates directly above (2.5 MHz) and below (1.25 MHz) this threshold identified the position at which the matrix rank deviated from the linear trend. Figure 4.2(c) shows this abrupt deviation from linearity, which is not explicitly clear by simply interpreting Fig. 4.2(b).

When the measurement space dimension exceeded the object space dimension, as was the case for region (iii), the limit on the maximum number of resolvable singular vectors became 8000 rather than the measurement space dimension. Accordingly, this places a limit on the effective matrix rank. Again, this deviation from linearity is depicted clearly in Fig. 4.2(c).

Below the sampling rate required to maintain system resolution, it is perhaps intuitive that the matrix rank would decrease. However, in region (ii) the presence of a linear trend is less intuitive. Although the Nyquist sampling criterion is rigorously met in region (ii), there is an averaging of the information contained in the signal recorded in the imaging operator. While fundamentally the point source is still adequately resolved at lower temporal sampling rates (but still above the Nyquist criterion), dynamic range is decreased since fewer measurement points are used to describe object space at each grid point. In this context, a greater dynamic range signifies an increase in the number of bits used to describe the intensity of a voxel. When the temporal sampling rate is increased,

the effective number of bits of used to represent each voxel is increased. Similar behavior is observed when applying a backprojection algorithm to the raw measurement data. As the degree of oversampling increases, a greater number of measurement points contribute to each voxel resulting in greater dynamic range.

The singular vectors plotted in Fig. 4.2(d) are shown in order to aid in the visualization of the vector content in a representative imaging operator. Coherent geometry is clear in images (i) and (ii), corresponding to singular vector indices 1 and 10. While a pattern is not discernable in images (iii) and (iv), it does not indicate that the vectors are void of information. First, only the centre plane is shown making it difficult to visualize geometry that could be coherent out of the plane. But more importantly, the practical limit of the voxel step-size makes it difficult to capture and observe the high frequency content that may actually reside in the higher order vectors. While image (iv) is beyond the matrix rank and consequently shows a singular vector in the null space, it is not clear how this impacts the limits of image reconstruction for this PA system.

The matrix rank is essential to applying generalized matrix inverse (GMI) reconstruction algorithms as it precisely indicates the object space singular vectors that contribute to resolving the unknown object. This has been investigated in other imaging modalities such as Single Photon Emission Computed Tomography (SPECT), indicating predictably that image quality is not improved when incorporating the use of singular vectors beyond the threshold outlined in Eq. (4.2) [17]. While the remaining object space singular vectors that exist in the null space of the imaging operator are linearly independent of the vectors above the threshold, the system cannot produce any object that is a combination of these vectors unless the reconstruction algorithm employs a priori information about the object (as can be achieved with iterative reconstruction methods [20]). However, even singular vectors within the limits of the matrix rank can be attributed to noise when the imaging operator is acquired experimentally. In these experimental imaging operators, if all vectors were included in the reconstruction up to the matrix rank, the noise in the experimental data set became correlated to the vectors within the threshold of the matrix rank.

#### ***4.4.2 Image reconstruction of objects with different transducer count***

For the reconstruction of a point, line, and multi-point objects shown in Fig. 4.3, the image fidelity increased as the transducer count increased. The reconstruction of the point source with 5 transducers was not a reliable reproduction of the phantom object. However, the task was still adequately completed if using the FWHM criterion. That is, no other voxel in the image exceeded 50% intensity of the voxel containing the point source. Yet, the same was not true for objects of increasing complexity. Both the line and multi-point source were not adequately reconstructed by the lower transducer count systems due to view aliasing. It should be noted that, for example, the strong artifacts seen in the 5 transducer count reconstructions were actually still present in the 30 transducer count reconstructions but were much less significant due to the acquisition of a greater number of projections. As illustrated by reconstruction of the different object types, the number of singular vectors required to successfully construct an image was task specific. As object complexity increased, the matrix rank required to produce an accurate image of the object had to be increased as well.

Reconstruction utilizing the iterative reconstruction technique resulted in images of relatively poor quality. This was performed only for the imaging system with 30 transducers and 5 MHz temporal sampling rate. The computation time required to complete the task was approximately 74 seconds. It was thought this technique may produce higher quality images in comparison to the pseudoinverse technique. However, this technique utilizes only the raw imaging operator and it is expected that the effects of noise are significant in comparison to a reconstruction technique that regularizes the pseudoinverse. As well, the reconstruction time is prohibitive with respect to a system oriented towards real-time imaging.

### ***4.4.3 Image reconstruction of objects with different measurement space temporal sampling rate***

Below the Nyquist threshold, the point source did not reconstruct well. Although the location of the point source was correctly reconstructed, the images were corrupted with streaking and ray aliasing artifacts. Likewise, objects of greater complexity (i.e. line and grid of point sources) did not reconstruct with good fidelity. However, the reconstruction quality improved for all three object types as the temporal sampling rate increased. The best reconstruction performance was achieved for the highest temporal sampling rate of 25 MHz for an array of 15 transducers. For all three object types, a distinct transition in reconstruction quality was made at the threshold between regions (i) and (ii) of Fig. 4.2(b). Below the Nyquist threshold, the images did not accurately depict the object. This was observed most clearly in the case of the point source that exhibited streaking artifacts in each of the three images belonging to region (i). Similar results were observed in the reconstruction of the array of point sources. However, the artifacts were less obvious as the streaking originated from many points, obscuring the overall effect from any particular point source in the grid. Certainly, in all three object types, reliable estimates of the object were not made until the temporal sampling rate exceeded the Nyquist threshold. This corresponded to a matrix rank of approximately 2000 or more.

### ***4.4.4 Real-time imaging of a photoacoustic point-like source***

The reconstruction of the point-like source was performed successfully at a period of 1.4 seconds per frame. While the object was not complex, Fig. 4.5 demonstrates that photoacoustic signal acquisition, transfer, image reconstruction and display can be performed successfully on experimental objects. It should be noted that the images shown in Fig. 4.5 have not been modified through any means such as thresholding. Each 3D image was reconstructed from data captured after a single laser pulse. Therefore, each 3D image effectively represented a snap shot of the point source during a 9 ns time interval (the pulse length of the laser). This unprecedented capability should provide a

path toward new applications such as 3D photoacoustic lifetime imaging and 3D tracking of moving targets (e.g. extensions of the 2D techniques described by Ashkenazi [21] and Su [22], respectively).

It is acknowledged that the voxel count is relatively low compared to other imaging systems or iterations of photoacoustic imaging that claim real-time 3D imaging. This work is intended to provide a foundation and proof of principle towards larger imaging volumes and voxel counts; parameters that are scaled straightforwardly provided computational system limitations are not surpassed. Additionally, while the voxel count is relatively low, the images are nevertheless 3D in nature. The imaging process is fundamentally different from that reported in other PA imaging schemes. It is therefore deemed important to explore real-time imaging in such a schematic, regardless of voxel count and imaging volume dimension.

Of course, the experimental object in this work is extremely simple. Attempting to image objects of greater experimental complexity may reveal shortcomings in the approach outlined in this work. Potential sources of complications can be found not only in the method for experimental acquisition of the imaging operator but also in the treatment of the time series, which formed the imaging operator. First, the imaging operator was acquired by scanning a point-like source through the imaging volume in a liquid bath and water. The speed of sound remains relatively constant during this experiment but could change significantly when attempting to image an object *in vivo* where this parameter is likely to vary through the object. These problems are not specific to this image reconstruction method, though, and are encountered in all methods of photoacoustic imaging reconstruction (backprojection, delay-and-sum, etc.). Second, the time series composing the imaging operator were manipulated such that inverted parabolas replaced the actual pulse acquired during experiment. This was done in order to retain the characteristic information in the PA wave but served to eliminate interference effects that could contribute to improperly zeroing of sources during reconstruction due to the bipolar nature of the PA wave. In more complex objects, this could be the source of inaccuracies in reconstruction.

#### ***4.4.5 Implications to previous work***

For larger matrices, the image reconstruction with the pseudoinverse significantly reduces the image reconstruction time when off-line image reconstruction is tolerable. In previous 4D photoacoustic imaging experiments, where iterative image reconstruction was utilized the image reconstruction time per frame was several minutes [12]. With knowledge of the imaging operator and a one-time computation of the pseudoinverse, the image reconstruction is now reduced to, at most, a couple seconds per frame.

#### ***4.4.6 Technical Considerations for faster 3D frame rates***

Real-time imaging and display encompasses both the data acquisition time as well as the reconstruction of an image from the data acquired. Until now, the time limiting process was image reconstruction because iterative reconstruction techniques were utilized that spanned minutes to produce an image. Solving directly for the image vector has improved the reconstruction time to approximately 0.05 s and the data transfer speed has become the rate limiting process. For our current system, the data transfer rate permits 5120 points from 32 channels to be transferred in approximately 1.2 s. In order to reduce this time, modifications to the acquisition process can be made. First, since only 2000 of the total 5120 points per channel are used in the imaging operator, implementing a delay between the laser pulse and the start of data capture would provide a reduction in data transfer time from 1.2 s to 0.47 s. Second, improvements could be made to transfer the data from each card in parallel. With the current system, this would provide an additional 4-fold decrease in transfer time. Separately, the transfer process could be entirely changed to utilize a proprietary parallel data bus at 50 MHz that could reduce the transfer times to ~1.5 ms. With the improvements suggested, both acquisition and image reconstruction could be completed in under 0.1 s.



The utilization of a solution to Eq. (1.18) to perform image reconstruction is a significant transition towards 3D photoacoustic imaging where the data is captured and images are reconstructed in real time (e.g. Fig. 4.5). Because the pseudoinverse of the imaging operator can be computed before data acquisition, only matrix multiplication of the pseudoinverse to the measured data set is required to produce the image. Even with no software optimization, for a matrix size of  $1792 \times 6000$ , the matrix multiplication typically required approximately 0.05 seconds in MATLAB. This computation time could be reduced with GPU hardware acceleration. Therefore, real-time 3D photoacoustic imaging at the laser repetition rate (10 Hz) should be achievable using pseudoinverse image reconstruction with a known imaging operator and improved computational capabilities.

## 4.5 Conclusion

Our PAI system was modified to contain 30 transducers arranged in a hemispherical geometry. An imaging operator was experimentally acquired with a step-size of 1.5 mm within an object space of  $30 \times 30 \times 30 \text{ mm}^3$ . By decomposing the imaging operator and analyzing the magnitude of the singular values, the effective matrix rank of the imaging operator was estimated. The results clearly show a linear increase in the effective matrix rank as both the transducer count and measurement space temporal sampling rate were increased. Image reconstruction of a variety of objects was performed by computing the pseudoinverse of each decomposed imaging operator and multiplying it with the measured data set of each phantom object. As expected, image fidelity was greater in cases with more transducers and increased temporal sampling rate. Image reconstruction was also performed in a period of 1.4 s per frame on a moving point-like source to demonstrate real-time acquisition, reconstruction and display of 3D photoacoustic images. Extension of the real-time 3D photoacoustic imaging to a frame rate of 10Hz should be easily achieved with straightforward improvements to data transfer time and computation speed.

## 4.6 References

1. L. H. V. Wang , " Ultrasound-mediated biophotonic imaging: A review of acousto-optical tomography and photo-acoustic tomography," *Dis. Markers* **19**, 123-138 (2003).
2. G. J. Diebold, T. Sun, and M. I. Khan , " Photoacoustic monopole radiation in one, two, and three dimensions," *Phys. Rev. Lett.* **67**, 3384-3387 (1991).
3. R. A. Kruger, D. R. Reinecke, and G. A. Kruger , " Thermoacoustic computed tomography-technical considerations," *Med. Phys.* **26**, 1832-1837 (1999).
4. D. Frauchiger, K. P. Kostli, G. Paltauf, M. Frenz, and H. P. Weber, "Optoacoustic tomography using a two dimensional optical pressure transducer and two different reconstruction algorithms" in *Hybrid and Novel Imaging and New Optical Instrumentation for Biomedical Applications, June 18,2001 - June 21* ( SPIE), 74-80.
5. M. Frenz, K. P. Kostli, G. Paltauf, H. Schmidt-Kloiber, and H. P. Weber, "Reconstruction technique for optoacoustic imaging" in *Biomedical Optoacoustics II, January 23, 2001 - January 24* ( SPIE), 130-137.
6. C. G. A. Hoelen and De Mul, Frits F. M. , " Image reconstruction for photoacoustic scanning of tissue structures," *Appl. Opt.* **39**, 5872-5883 (2000).
7. K. P. Kostli, D. Frauchiger, J. J. Niederhauser, G. Paltauf, H. P. Weber, and M. Frenz , " Optoacoustic imaging using a three-dimensional reconstruction algorithm," *IEEE Journal on Selected Topics in Quantum Electronics* **7**, 918-923 (2001).
8. G. Paltauf, J. A. Viator, S. A. Prah, and S. L. Jacques , " Iterative reconstruction algorithm for optoacoustic imaging," *J. Acoust. Soc. Am.* **112**, 1536-1544 (2002).
9. M. H. Xu and L. V. Wang , " Universal back-projection algorithm for photoacoustic computed tomography," *Photons Plus Ultrasound: Imaging and Sensing 2005* **5697**, 251-254 (2005).
10. M. Roumeliotis, R. Z. Stodilka, M. A. Anastasio, G. Chaudhary, H. Al-Abed, E. Ng, A. Immucci, and J. J. L. Carson , " Analysis of a photoacoustic imaging system by the crosstalk matrix and singular value decomposition," *Optics Express* **18**, 11406-11417 (2010).
11. P. Ephrat, L. Keenliside, A. Seabrook, F. S. Prato, and J. J. L. Carson , " Three-dimensional photoacoustic imaging by sparsearray detection and iterative image reconstruction," *J. Biomed. Opt.* **13**, 054052 (2008).
12. P. Ephrat, M. Roumeliotis, F. S. Prato, and J. J. Carson , " Four-dimensional photoacoustic imaging of moving targets," *Opt. Express* **16**, 21570-21581 (2008).

13. M. Roumeliotis, P. Ephrat, J. Patrick, and J. J. L. Carson , " Development and characterization of an omnidirectional photoacoustic point source for calibration of a staring 3D photoacoustic imaging system," *Optics Express* **17**, 15228-15238 (2009).
14. D. W. Wilson and H. H. Barrett , " Decomposition of images and objects into measurement and null components," *Optics Express* **2**, 254-260 (1998).
15. K. Konstantinides and K. Yao , " Statistical analysis of effective singular values in matrix rank determination," *IEEE Transactions on Acoustics, Speech, and Signal Processing* **36**, 757-763 (1988).
16. K. Konstantinides , " Threshold Bounds in Svd and a New Iterative Algorithm for Order Selection in Ar Models," *Ieee Transactions on Signal Processing* **39**, 1218-1221 (1991).
17. D. J. Kadrmas, E. C. Frey, and B. M. W. Tsui , " An SVD investigation of modeling scatter in multiple energy windows for improved SPECT images," *IEEE Trans. Nucl. Sci.* **43**, 2275-2284 (1996).
18. P. Ephrat and J. J. L. Carson, "Measurement of photoacoustic detector sensitivity distribution by robotic source placement" in *9th Conference on Photons Plus Ultrasound: Imaging and Sensing 2008, January 20,2008 - January 23 ( SPIE)*, Society of Photo-Optical Instrumentation Engineers (SPIE).
19. A. A. Oraevsky, V. G. Andreev, A. A. Karabutov, and R. O. Esenaliev , " Two-dimensional opto-acoustic tomography transducer array and image reconstruction algorithm," *Proc SPIE Int Soc Opt Eng* **3601**, 256-267 (1999).
20. J. Provost and F. Lesage , " The Application of Compressed Sensing for Photo-Acoustic Tomography," *IEEE Trans. Med. Imaging* **28**, 585-594 (2009).
21. S. Ashkenazi , " Photoacoustic lifetime imaging of dissolved oxygen using methylene blue," *J. Biomed. Opt.* **15**, (2010).
22. J. Su, A. Karpouk, B. Wang, and S. Emelianov , " Photoacoustic imaging of clinical metal needles in tissue," *J. Biomed. Opt.* **15**, (2010).

# Chapter 5:

## *Discussion and future work*

This chapter concludes the dissertation. The content links the studies discussed in Chapters 2 through 4 and provides insights to future research and development related to them.

### **5.1 Technology Development**

This system has undergone substantial technological advancement from the early work to the current state of the system. However, advancements can still be made to improve the quality of the system to optimize performance. This includes not only image fidelity, but also data acquisition and reconstruction time. This section discusses these ideas in the context of improvements to be made to the PAI system.

#### ***5.1.1 Calibration protocol***

Improvements made to the calibration procedure developed in Chapter 2 could vastly improve system performance as related to image quality. The motivation for using a liquid-based photoacoustic point source stemmed from the inherent behaviour of the liquid to produce a uniform PA wave in the azimuth direction. Earlier PA sources developed displayed significant deviation in PA wave magnitude over the azimuth due to polishing imperfections in the fibre. That said, the variability in PA wave magnitude in the zenith direction is still a concern, despite a marked improvement from previous design iterations developed in our group's earlier work. The development of a source that emits PA waves of greater uniformity will improve the fidelity to the linear model when constructing the imaging operator. This will be especially important for sources detected by the transducers in the upper rows of the hemisphere, as they are most impacted by the reduction in signal strength at increasing zenith elevations.

The calibration procedure is performed in a solution with acoustic properties similar to water. This approach could be modified such that the calibration is done in a defined object space with properties more closely mimicking tissue. The PA waves recorded on transducers are not adapted to the changes that would be seen true of imaging tasks performed in real tissue. That is, the amplitude, FWHM, and time-of-flight of the waves emanating from a particular voxel may change if the imaging task is done in a medium with different acoustic properties. While these changes are expected to be minimal, it could become significant as imaging depths are increased. To this point, the temperature at which the calibration procedure is performed should be regulated to match the expected imaging task. Currently, the scan is performed with both the source and water tank at room temperature. The speed of sound will vary if the source is expected to be *in vivo* applications (mouse, human, etc.).

Beam inhomogeneity during the procedure has also produced inaccuracies in the results. In the current approach, the fibre collects light directly from the beam as it exits the laser aperture, which is considered relatively inhomogeneous in energy distribution. Therefore, the pulse-to-pulse variation in energy delivered to the point source can be influential on the recorded PA waves. While the photodiode was implemented to sample this variation, the fibre itself is bifurcated such that the light collected that is directed to the photodiode is separate from the light that is directed to the PA source. A beam homogenizing system has recently been implemented using a micro lens array to produce a beam with greater uniformity that is collected by the fibre.

The approach to acquiring an experimental imaging operator itself can be modified if a simulated imaging operator can be modeled in a more accurate and simple technique. If analytical modeling of transducer behaviour is performed, these data could be used in producing a simulated imaging operator. In this context, it would be useful to address not only for potential accuracy improvement in the reconstruction approach but also reconstruction simulations could be made in order to evaluate potential system designs before physical realizations of the system are constructed. At this time, however,

it is unknown whether the experimental or simulated approach to PAI will be more accurate.

### ***5.1.2 System improvements***

As described in Chapter 4, the current achievable frame rate is approximately 0.7 fps. This is limited largely by the rate of data acquisition and to a lesser extent, the image reconstruction computation time. In order to advance the frame rate, improvements in both data acquisition rate and image reconstruction time must be made.

Currently, the data acquisition electronics typically record 5120 data points to sample the entire object space. However, many of these data points do not contain useful information because they originate from a position outside the defined object space. This is due to the distance between each of the transducers and the centre of the hemisphere. Therefore, a time delay could be introduced such that the data acquisition system only acquires data from the region defined by the object space. Currently, a maximum of 2000 out of the possible 5120 data points are used in the construction of the imaging operator. Even in the largest object space used, that would reduce the data acquisition time by a factor of approximately 2.5. Of course, in object spaces of smaller dimension (possible for some imaging tasks), the number of data points used could be even smaller, resulting in an even greater reduction in data acquisition time.

After the data has been transferred to the PC for image reconstruction, there is an intermediate step, which requires the processing of the data set such that it is in the same format as the data that composes the imaging operator. This is done using custom-built software that is called during the Labview™ sequence. Presumably, this same processing could be done with built-in Labview™ techniques. While the increase may be relatively minor in comparison to the data acquisition and image reconstruction times, it is nevertheless an improvement that could reduce the overall sequence time by tens of milliseconds.

Data acquisition is performed in a serial manner from each of the 4 electronic boards (containing 8 channels). If parallel communication was taken advantage, an increase in transfer rate by a factor of 4 could be expected. As well, image reconstruction can take up to 100 ms with the existing imaging operators by utilizing MATLAB® to perform the matrix multiplication. Utilizing higher speed processing (GPUs), this could be reduced significantly as well. It is difficult to comment on the degree to which this could improve reconstruction time as many factors influence the matrix multiplication. This includes the number of non-zero entries in the imaging operator,  $\mathbf{H}$ , and data set,  $\mathbf{g}$ , making it difficult to predict any precise reduction in computation time. However, other operations performed in MATLAB® utilizing GPU processing techniques have reduced the computation time by a factor of anywhere between approximately 2 and 40.

System noise can contribute significantly to image reconstruction problems as it propagates from sampled data to the imaging operator. In order to understand system limitations and the consequence of noise on image reconstruction, objective assessment of these features will need to be performed. With quantified understanding of noise on system performance, improvements can be made as well as limitations more comprehensively understood.

## **5.2 Characterization Technique Improvements**

Both the crosstalk matrix and singular value decomposition described in Chapter 3 could provide additional information than was reported in the original experiments. While some of this information does not directly relate to the task of real-time imaging, it is still important to mention as performance metrics can be derived from already-acquired information.

### ***5.2.1 The crosstalk matrix***

In Chapter 3, the crosstalk matrix was introduced as a method to quantify the shift-variant nature of system sensitivity and aliasing. This information provides a relative value of both sensitivity and aliasing for each individual voxel in the object space. However, the values reported in Chapter 3 only showed representative aliasing quantities (centre and corner voxels) and were limited to describing any corrective measures that could be implemented from the computed the system sensitivity. Calibration scans could be done with much finer resolution than were performed in order to more accurately quantify the shift-variant spatial resolution of the PA imaging system. Because the aliasing values indicate the relative magnitude of indistinguishable signal between 2 voxels, standard FWHM criteria could be used as a metric to provide the shift-variant resolution maps. This will serve to provide a better understanding of fundamental system performance for an imaging system that is designed to undertake a particular imaging task.

### ***5.2.2 Singular value decomposition***

During image reconstruction, a relatively arbitrary number of singular vectors were used to reconstruct the experimental point source in Chapter 4. While this worked well as a proof of principle, more precise testing could be done in order to improve the quality of a reconstructed object. Once the pseudoinverse of an imaging operator is computed, regularization could be done for a variable number of singular vectors. Image reconstruction could be performed on a point source at the centre of the object space, where the point spread function (PSF) is evaluated. This would provide an empirical estimate of the matrix rank, as it would be expected that at a particular threshold, image quality would not improve or even worsen. Unfortunately, the results will vary depending on the calibration scan parameters; measurement space sampling rate, voxel count, transducers used to measure the object space, and system noise. However, this would provide specific criterion by which image reconstruction efficiency could be maximized



for a particular system design. As well, image reconstruction time could improve if only the optimal numbers of singular vectors are used.

## **5.3 Applications**

Generally, any imaging task performed using this 3D PA imaging system will make full use of the temporal resolution of the system. However, it is important to note a fundamental behaviour of the real-time imaging associated with this system. That a single real-time frame is capturing a snap-shot over time periods only related to the duration of the laser pulse. As the technology develops and frame rates improve, the images will still represent information generated over a time scale on the order of 5 to 10 ns. Therefore, imaging tasks can be developed to visualize process occurring on this time scale as well as macroscopic object tracking.

### ***5.3.1 Contrast tracking***

Contrast tracking is an important imaging task and has been developed for other optical and non-optical imaging modalities. As contrast can often be used to provide a surrogate marker for physiological features, it is a natural direction to pursue for PA imaging technology. Gold nanoparticles are an appealing contrast agent for PA imaging because of their strong biocompatibility and potential for therapeutic treatment of cancer. However, it has proven a challenge to monitor the nanoparticles non-invasively once injected into tissue. PA tomography has recently been used as a method to monitor the location of gold nanoparticles in a mouse abdomen [1]. While the study showed very good localization of the nanoparticles in mouse, the data was collected using a PAT system that required mechanical scanning and, consequently, relatively long imaging time periods. This concept could be expanded upon using our 3D PA imaging system to produce accurate localization of the nanoparticles at depths of approximately 2 cm.

### ***5.3.2 Object tracking***

Sentinel lymph node biopsy has become the standard care for patients diagnosed with breast cancer. Typically, biopsy of the lymph node is performed to directly drain the tumour area. Currently, US guidance is the primary method of guiding targeted needle biopsies. Research performed by Erpelding et al. has introduced a technique to dye the lymph nodes with indocyanine green and track them using PA imaging technology [2]. More recently, the same group modified a clinical US system to handle light delivery, allowing for hand-held scanning and tracking of the needle biopsy process [3]. The PA imaging frame rate was 1 Hz, but only captured 2D images. A similar experiment could be performed with our 3D PA imaging system with the system described in this dissertation, or 3D hand-held systems also being developed by our group.

## **5.4 Recommendations**

As outlined in section 5.1 and 5.2, many improvements could be made to the imaging approach for this PA system. In this section, changes and improvements of high priority are outlined in order to provide direction to the imminent future of the PA system based on the current system weaknesses.

### ***5.4.1 Weaknesses***

Improvement of the data acquisition electronics and reconstruction software are of paramount importance at this point in the development of the PA system. Both these features are currently the time-limiting factor in the imaging process but with straightforward improvements, imaging at the repetition rate of the laser can be easily achieved. This will advance the current state of the technology towards true 3D real-time imaging.

The current state of the photoacoustic point source used for calibration is another crucial drawback. Improvements to the source are vital in accurately representing the imaging operator of the PA system. The non-uniformity that is associated with this generation of the photoacoustic point source will be the foundation of many problems in representing objects during image reconstruction. As such, improvements and new iterations of the point source should be explored in order to improve the quality of image reconstruction.

A greater understanding of the regularization process and associated reconstruction quality is required in order to maximize the information garnered during the imaging process. This was only explored briefly in Chapter 4 in order to generate the experimental image of a point source at 0.7 fps. A systematic study of image quality can be performed through higher resolution calibration scans (smaller step-size) with different regularization criteria.

Both the crosstalk matrix and singular value decomposition techniques employed in Chapter 3 and 4 were only used at a cursory level. Essentially, little work was performed beyond experimentally computing the associated matrices and implementing them directly into our image reconstruction approach. Higher level information can be extracted and quantified that will more directly link these techniques to performance metrics. However, our work was simply a first step in acquiring these techniques experimentally as applied to image reconstruction. It is acknowledged that the techniques themselves are not novel, but first applied in the context of PA imaging. Significant work would be required to fully understand the content of the imaging operator as it pertains to these techniques (and others) and could be addressed in follow-up papers.

It should be noted that the crosstalk and SVD techniques experimentally acquired in this work are not intended, as yet, to be a final step towards realizing PA imaging via this matrix reconstruction technique and can appear unnecessarily complicated at the onset. Metrics that are more easily understood could be used to describe the imaging system in order to circumvent utilization of these techniques. However, because the

system developed in this work is under constant revision, more common metrics (resolution, contrast, etc.) have little meaning as the system is being developed at a more fundamental level. As the system approach is validated and advances to a more stable state with minor incremental improvements between iterations, these common metrics should be evaluated and addressed.

The hemispherical array utilized in this work is certainly not the only realization of sparse arrays that could be implemented to perform 3D PAI. This approach was selected as it maximizes views on a three-dimensional surface directed towards a specified imaging volume. However, other sparse arrays could be employed and assessed for image reconstruction performance. As mentioned in section 5.1.1, modeling of imaging operators for other array geometries could be performed to provide performance insight prior to construction of the array. As the work advances, this may be necessary in selecting array geometry to maximize image reconstruction performance with particular applications in mind. More rigorous methods, as outlined by Turnbull et al. [4], could be used to outline the design of a sparse array. This would provide objective criteria by which to design a sparse array.

## **5.5 Conclusions**

Through the duration of this dissertation, a novel approach to 3D photoacoustic imaging was developed. This technique implemented the use of a staring, sparse, transducer array to collect PA measurements produced from a single laser pulse. In a series of studies, the system performance was calibrated and characterized, providing the foundation for an image reconstruction approach to be implemented in PA imaging for the first time. As a result, real-time 3D PA images were produced at 0.7 fps.

In Chapter 2, a calibration procedure was developed by using a point-like PA source to characterize the response of the transducer array at each voxel in the object space. The PA source was developed using a combination of both methylene blue and

Intralipid™ to absorb and scatter the incident photons in a manner that produced a spherical absorption pattern. This PA source was then raster scanned through the object space and at each voxel, the PA measurement was recorded simultaneously by each of the transducers in the hemispherical array. From this, data was extracted in order to correct for the shift-variant response of the PA system during the image reconstruction process. This included the signal amplitude, FWHM, and time-of-flight.

Later, an imaging operator was compiled using the foundation developed in Chapter 2. The imaging operator describes the system response to a PA point source at each voxel in the object space. This allowed for further characterization of our PA system by the crosstalk matrix and singular value decomposition. The crosstalk matrix allowed quantification of the cumulative system sensitivity as well as aliasing between two voxels in the object space. Singular value decomposition was used as a tool to describe the complexity of objects that can be represented by our imaging system; vitally important for a system that only sparsely samples the object space.

In Chapter 4, a transition to performing image reconstruction by solving a linear system model was implemented. In this work, the behaviour of our imaging system as characterized by singular value decomposition was first assessed in order to perform image reconstruction with the appropriate pseudoinverse matrix. Afterwards, image reconstruction was performed on both simulated and experimental objects in order to validate the procedure. The entire imaging sequence computation time, from laser pulse to image display, requires approximately 1.4 seconds.

This technology, while still developing, can be used for a variety of applications taking advantage of the high temporal resolution and inherently 3D nature of the imaging process. Most directly, this will certainly involve real-time tracking of an optically absorbing object.

## 5.6 References

1. Q. Zhang, N. Iwakuma, P. Sharma, B. M. Moudgil, C. Wu, J. McNeill, H. Jiang, and S. R. Grobmyer , " Gold nanoparticles as a contrast agent for in vivo tumor imaging with photoacoustic tomography," *Nanotechnology* **20**, 395102 (2009).
2. T. N. Erpelding, C. Kim, M. Pramanik, L. Jankovic, K. Maslov, Z. Guo, J. A. Margenthaler, M. D. Pashley, and L. V. Wang , " Sentinel Lymph Nodes in the Rat: Noninvasive Photoacoustic and US Imaging with a Clinical US System," *Radiology* **256**, 102-110 (2010).
3. C. Kim, T. N. Erpelding, K. Maslov, L. Jankovic, W. J. Akers, L. Song, S. Achilefu, J. A. Margenthaler, M. D. Pashley, and L. V. Wang , " Handheld array-based photoacoustic probe for guiding needle biopsy of sentinel lymph nodes," *J. Biomed. Opt.* **15**, 046010 (2010).
4. D.H. Turnbull and F.S. Foster, "Beam Steering with pulsed two-dimensional transducer arrays," *IEE Trans. Ultrason. Ferroelect. Freq. Contr.* **38**(4), 320-333 (1991).

# **Appendix 1:**

## ***A1 - Analysis of a photoacoustic imaging system by singular value decomposition***

This appendix contains the manuscript that was published in March 2010, according to the conference standards established for *Photonics West*, organized by *SPIE* in San Francisco, USA. Brief citation as follows: M. Roumeliotis, G. Chaudhary, M.A. Anastasio, R.Z. Stodilka, A. Immucci, E. Ng, J.J.L. Carson. "Analysis of a photoacoustic imaging system by singular value decomposition" *SPIE Annual Meeting, Symposium on Biomedical Optics (BiOS)*, 7564-113, San Francisco, USA, 2010.

Appendix 1 describes the acquisition of an experimental imaging operator as well as a simulated imaging operator. Both imaging operators were then analyzed through the application of the singular value decomposition technique. Here, object space singular vector geometry was visualized for both experimental and simulated imaging operators. As well, the magnitude of the singular values for the experimental imaging operator was plotted. Results generally indicated the successful acquisition of an imaging operator and subsequent analysis by singular value decomposition was possible.

## **A1.1 Introduction**

### ***A1.1.1 Background***

Photoacoustic (PA) imaging is a technique that can accurately map the location and size of optically absorbing structures inside an object. The technique provides images with contrast similar to direct optical imaging techniques, but with increased penetration depth in turbid media by encoding the optical information as acoustic waves [1-2]. The method utilizes short laser pulses to diffusely illuminate the object. Provided the optical energy is deposited over a sufficiently short period of time, the absorbing structures

undergo thermoelastic expansion and the energy is re-emitted as an outwardly propagating photoacoustic pressure wave with characteristics related to the size and depth of the optical absorber [3]. Back-projection of time-domain measurements at a number of perspectives provides a means to locate and identify the location and size of the optical absorbers inside the object.

Our group has been developing a photoacoustic imaging method that utilizes a sparse array of acoustic detectors to collect signals at a limited number of perspectives. The system utilizes a staring array of detectors combined with parallel data acquisition and an iterative image reconstruction algorithm to produce three-dimensional photoacoustic images using only a single laser pulse [4]. An iterative reconstruction algorithm, first proposed by Paltauf et. al. [5], was employed in combination with the sparse array to account for the limited number of projections. However, this system will inevitably fail to reconstruct objects from the limited data set if the object exceeds a certain complexity due to the limited number of data projections acquired of each object. Therefore, our objective was to apply methodology originally developed for characterizing medical imaging systems to obtain insight into the complexity of objects that could be imaged with the staring, sparse-array photoacoustic imaging system. Our approach was to first obtain a detailed system response to a grid of locations (discretely sampled imaging operator) within object space using a robotically-controlled calibration scan. Then, apply singular value decomposition analysis to obtain the singular values and singular vectors from the imaging operator. These experimental results were then compared to an imaging operator modeled by a photoacoustic imaging system with the same transducer arrangement but with an ideal response to a point source (noiseless, shift-invariant).

### ***A1.1.2 Singular value decomposition***

Singular value decomposition provides a significant portion of the work in this chapter. For details, please refer to section 1.5.3.



## A1.2 Methods

The imaging system utilized 15 ultrasound transducers (model V304, 1"  $\varnothing$ , 2.25 MHz with fractional bandwidth of 65%, *Panametrics-NDT*, Waltham, Massachusetts) in a staring hemispherical arrangement. Transducers were mounted on 5 custom-built frames, each supporting 3 transducers at zenith angles of 22.5°, 45°, and 67.5°. The frames were designed such that the sensitivity of all 15 transducers were intended to overlap in a specified imaging volume of approximately 25x25x25 mm<sup>3</sup> near the geometric center of the array. Laser illumination ("Surelite OPO Plus", OPO-coupled Nd:YAG, *Continuum*, Santa Clara, California) was directed to a bifurcated fiber (400  $\mu$ m diameter) such that half of each laser pulse was guided to a photodiode (to measure pulse-to-pulse variation) and the other half to an optical fiber immersed in the liquid (where the photoacoustic signal was generated) for a total of 16 channels collecting data (15 transducers, 1 photodiode). The pulse duration was 6 ns at a repetition rate of 10 Hz with a maximum laser output of approximately 100 mJ/pulse. Note, that only a small fraction of the pulse was accepted by the fiber due to its small core size relative to the beam diameter (~1.5 cm). All calibration scans were done at 675 nm. Each transducer was electrically connected to a dedicated channel on a preamplifier card (custom built). The analog signals were acquired in parallel, converted to digital signals, and sent to a personal computer for analysis. The custom built data acquisition system sampled with 14-bit resolution at a frequency of 50 MHz. A calibration scan was performed to acquire the response of each transducer at each voxel in object space. The scan was completed with an imaging volume of 30x30x30 mm<sup>3</sup> and 3 mm step-size for a total of 1000 data points. At each test position in the scan, the PA signal was averaged over 10 pulses. After the calibration scan, the averaged time series data for each transducer and grid location was analyzed off-line to obtain the imaging operator corresponding to the scan. The imaging operator has rows corresponding to the number of voxels in object space. Each row in the matrix contains elements equal to the number of points used to sample the object space multiplied by the number of channels collecting data (in this case, 15). The simulated imaging operator was generated by creating data corresponding to a scan of the same dimension. However, the transducer response was considered shift-invariant

and noiseless. Singular value decomposition of both imaging operators was performed in MATLAB via the built-in singular value decomposition function.

## A1.3 Results

The decomposition of the system matrix yields a set of orthonormal singular vectors that describes both the projection and object space of the PA system. An imaging operator was acquired for both the experimental scan and a simulated system. Column vectors of matrix  $\mathbf{V}^T$  were organized by reshaping the vectors such that each entry in the vector visually corresponded to its location in object space. That is, the system contained no noise and a shift-invariant point spread function. The center plane of object space was then plotted in both the simulation and experimental decompositions to aid in visualization. The data corresponding to the experimental imaging operator for the experimental scan is displayed in Fig. A1.1(a). Simulations were produced using an ideal PA system with the same arrangement of transducers and object space as the experimental setup and is displayed in Fig. A1.1(b).

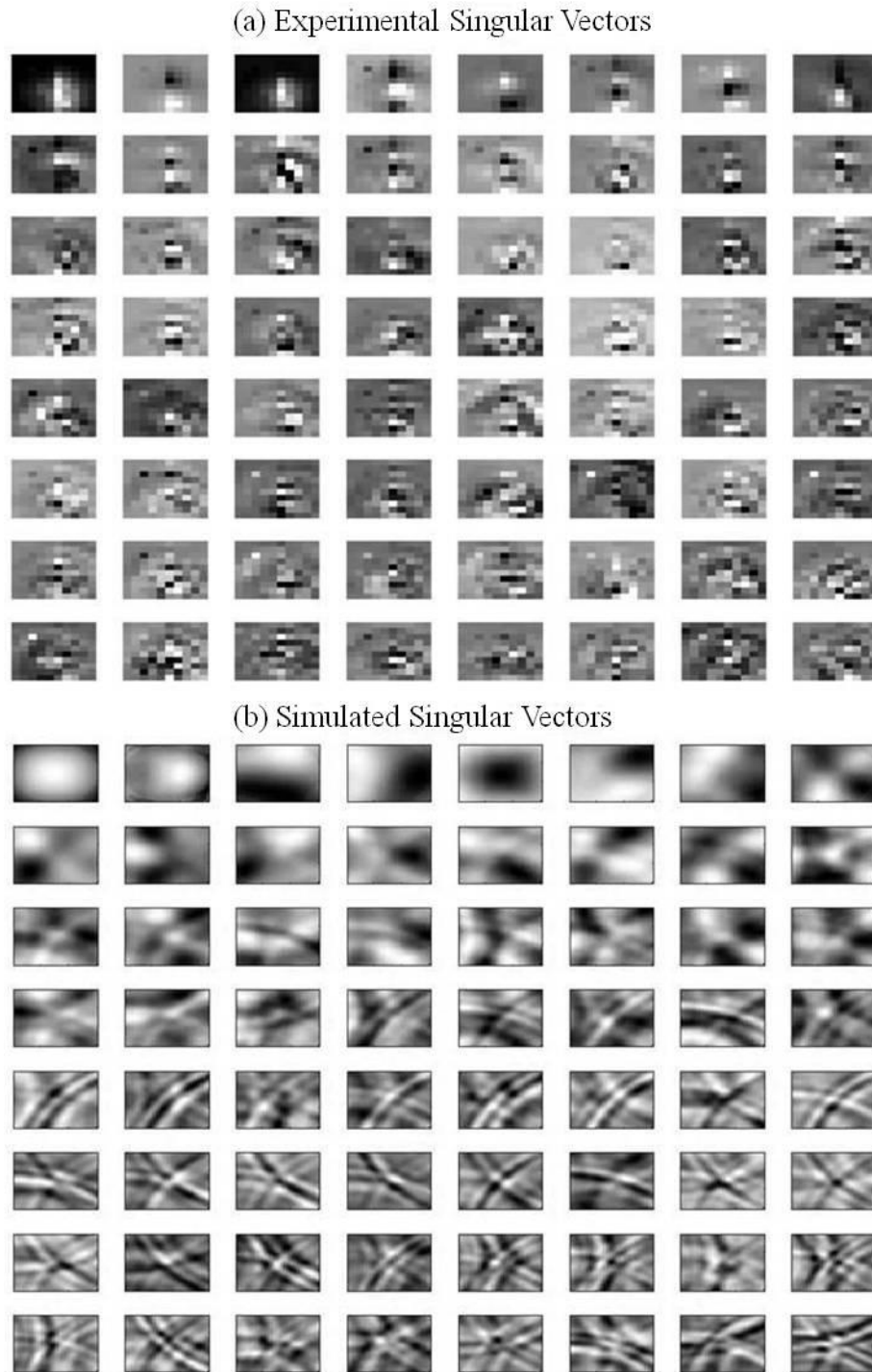


**Figure A1.1:** (a) and (b) Displays the center x-y plane of the first 64 singular vectors acquired via experiment and simulation, respectively. The field-of-view for each singular vector is  $30 \times 30 \text{ mm}^2$ . The singular vector number reads from left to right and top to bottom.

The SVD technique also produces information regarding the sensitivity of a PA system to the particular singular vectors in the matrix  $\mathbf{U}$  and  $\mathbf{V}$ . The sensitivity to a particular singular vector is taken from the main-diagonal of the decomposition matrix,  $\mathbf{S}$ , which is shown in Fig. A1.2. Each of the first 1000 singular values were plotted for experimental scan.

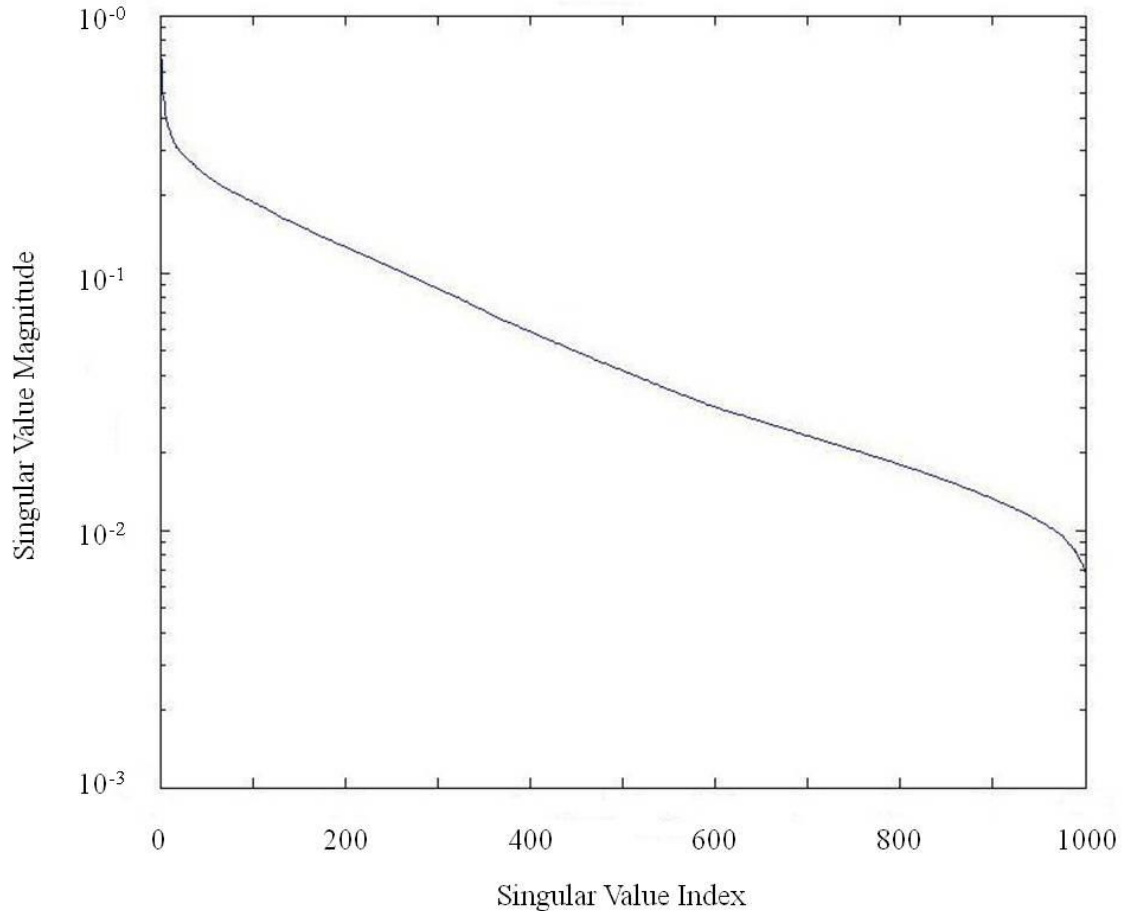


**Figure A1.2:** Plot indicates the magnitude of the first 1000 singular values acquired from the SVD matrix,  $\mathbf{S}$ .

## A1.4 Discussion

Evident in the results of Fig. A1.1 is the discrepancy between the simulated and experimental singular vectors produced by the SVD of both system matrices. Many

factors contribute to the degraded quality of the system singular vectors in the experimental case. These include noise, a shift-variant response, and a PA point source that does not produce a perfectly omni-directional acoustic wave.

A geometric interpretation of the experimental singular vectors does show similar features to the lower order singular vectors generated by the simulation imaging operator. For example, the simulation singular vectors in the first row of Fig. A1.1(b) display relatively simple geometry. More specifically, singular vectors 1 through 4 show clear monopoles and dipoles. These trends are recreated in Fig. A1.1(a) where the representation of these same singular vectors has produced similar geometries. As the singular vectors in Fig. A1.1(b) increase in complexity, so do the singular vectors in Fig. A1.1(a). Since the experimental system has a relatively limited number of voxels over which the system matrix was acquired, any attempt to discern the quality of complex singular vectors becomes difficult. However, the successful reconstruction of simple objects confirmed in experiment [4] indicates the PA system does acquire information from at least a number of singular vectors capable of producing objects of varying geometry. In a broad sense, the SVD analysis of this PA system reveals that drastic improvements needed to be made in order to reconstruct objects of increasing complexity (though any specifications cannot be defined until a particular application is allotted to the PA system). It is simple to suggest the PA point source uniformity or signal-to-noise ratio be improved. However, these are broad qualifications and do not associate with advancements made regarding the fundamental system limitations (ie. transducer count). It is evident from further simulations (not shown), that increasing the number of transducers acquiring data projections significantly alters the geometry, and complexity, of the system singular vectors. It is also obvious from a comparison of simulation and experimental singular vectors that the shift-variant response of the experimental PA system degrades the information shown in Fig. A1.1(a).

The singular values yielded by the SVD analysis (in Fig. A1.2) necessarily show a decrease in the magnitude of the value with increasing singular value index. The magnitude of this value reveals the sensitivity of the PA system to a particular singular

vector. This sensitivity is manifested when the imaging operator is multiplied with the vector representation of an object. If we consider an object described by a vector in the object space, that vector can be projected onto the set of singular vectors in the matrix  $\mathbf{V}^T$ . Subsequently, each singular vector is multiplied by the corresponding singular value (defined by the outer product multiplication) and will explicitly define the image produced by the PA system.

There is a practical limitation to the precision of the results shown in Fig. A1.1(a). Because the calibration scan was limited by the number of voxels within a defined object space, the representation of the singular vectors produced by the SVD analysis are not of sufficient resolution to capture fine detail shown in the simulation singular vectors of Fig. A1.1(b). It then becomes difficult to make conclusions regarding the perceptible geometry of singular vectors that contain complex geometry. As well, it should be noted that not all singular vectors in an experimental system contribute to the reproduction of an object. At a particular threshold, the system noise prevents a singular vector (and all singular vectors afterwards) from contributing to the reconstruction of an object.

## **A1.5 Conclusion**

A technique was developed to acquire a data set that described the imaging operator of our PA system. An experimental scan was completed at a step size of 3 mm with an object space of  $30 \times 30 \times 30 \text{ mm}^3$ . A second imaging operator was simulated using the same system geometry but with ideal transducer response (noiseless, shift-invariant). Singular value decomposition analysis was performed on both imaging operators to provide insight into the system's capability of reconstructing objects as well as the system's sensitivity to those objects. It becomes evident through understanding the results of the singular value decomposition that this PA system only has the capability to reconstruct objects of simple geometry. This technique can broadly be applied to any PA system and can provide rationale guiding future system iterations.

## A1.6 References

1. T. Lu, J. Jiang, Y. Su, R. K. Wang, F. Zhang, and J. Yao, "Photoacoustic imaging: Its current status and future development," in 4th International Conference on Photonics and Imaging in Biology and Medicine, SPIE, (2006).
2. M. Xu and L. V. Wang, "Photoacoustic imaging in biomedicine," *Rev. Sci. Instrum.* 77, 041101 (2006).
3. G. J. Diebold, T. Sun, and M. I. Khan, "Photoacoustic monopole radiation in one, two, and three dimensions," *Phys. Rev. Lett.* 67, 3384-3387, (1991).
4. P. Ephrat, M. Roumeliotis, F. S. Prato, and J. J. Carson, "Four-dimensional photoacoustic imaging of moving targets," *Opt. Express* 16, 21570-21581, (2008).
5. G. Paltauf, J. A. Viator, S. A. Prahl, and S. L. Jacques, "Iterative reconstruction algorithm for photoacoustic imaging," *J. Acoust. Soc. Am.* 112, 1536-1544, (2002).

## **Appendix 2:**

### ***A2 - Estimate of effective singular values of a photoacoustic imaging system by noise characterization***

This appendix contains the manuscript that was published in March 2011, according to the conference standards established for *Photonics West*, organized by *SPIE* in San Francisco, USA. Brief citation as follows: M. Roumeliotis, M.A. Anastasio, J.J.L. Carson. "Estimate of effective singular values of a photoacoustic imaging system by noise characterization" SPIE Annual Meeting, Symposium on Biomedical Optics (BiOS), 7899-65, San Francisco, USA, 2011.

Appendix 2 describes the method by which de-noised and noise-only imaging operators were derived from an experimental imaging operator. By analyzing the magnitudes of the singular values associated with each of the imaging operators, broad conclusions were made regarding the number of effective singular values contributing to the imaging system. As well, visualization of key singular values was shown in order to confirm the expectation that differences were present in singular vectors of the same index.

## **A2.1 Introduction**

### ***A2.1.1 Background***

Photoacoustic (PA) imaging is a technique utilizing the advantages inherent to both optical and ultrasonic imaging modalities [1]. By exposing optically absorbing objects to a short-duration pulsed laser, a fraction of the energy is converted to heat, leading to a slight increase in temperature. The slight temperature increase results in thermoelastic expansion of the absorbing object and an outwardly propagating acoustic wave. Optical information characteristic of the object is contained within the propagating pressure wave [2]. This includes the location, size, shape and optical properties of the



absorbing object. Photoacoustic imaging exploits time-domain pressure measurements to produce photoacoustic images by one of a variety of reconstruction techniques [3-6].

In earlier work, we introduced a technique to experimentally measure the imaging operator of a PA imaging system where an estimate on the number of effective singular vectors was made [7]. However, the work was completed on an experimental imaging system with intrinsic system noise, limiting broad conclusions to the number of effective singular vectors in the imaging system. The consequence of system noise on the magnitude of the singular values was not assessed in previous work but was expected to influence the magnitude of the singular values associated with the decomposition of the imaging operator.

In this work, two additional imaging operators were produced based on the experimental imaging operator acquired in previous work. More specifically, a de-noised imaging operator was created by removing all extraneous system noise from the experimental imaging operator such that the matrix contained only photoacoustic signal above a specified threshold. A second imaging operator was produced by removing all signals above a threshold such that the imaging operator contained only system noise. Singular value decomposition of the experimental, de-noised, and noise-only imaging operators was computed. The magnitude of the singular values and the content of the singular vectors were analyzed to determine the contribution of noise to the singular vector spectrum.

### ***A2.1.2 Singular value decomposition***

Singular value decomposition provides a significant portion of the work in this chapter. For details, please refer to section 1.5.3.

## **A2.2 Methods**

The techniques utilized to acquire the experimental imaging operator were similar to those implemented in our earlier publications [7-9]. A brief summary of the experiment is noted in this section as well as any changes made to the procedure.

### ***A2.2.1 The photoacoustic system***

The imaging system utilized 30 ultrasound transducers (model V304, 1" Ø, 2.25 MHz with fractional bandwidth of 65%, *Panametrics-NDT*, Waltham, Massachusetts) in a staring hemispherical arrangement. Transducers were mounted on custom-built frames, each supporting 3 transducers at evenly spaced azimuthal angles ( $36^\circ$  between columns). Fifteen (15) of the transducers were mounted on frames with zenith angles of  $22.5^\circ$ ,  $45^\circ$ , and  $67.5^\circ$ . The remaining 15 transducers were mounted on frames placed azimuthally between the original frames, at zenith angles of  $33.75^\circ$ ,  $56.25^\circ$ , and  $78.75^\circ$ . A total of 31 channels collected data (30 transducers, 1 photodiode).

### ***A2.2.2 The imaging operator***

The imaging operator was acquired by raster scanning the optical fiber (photoacoustic point source) through each voxel in the imaging volume ( $30 \times 30 \times 30 \text{ mm}^3$  with 1.5 mm step-size) and recording the signal retrieved by each of the 30 transducers (50 MHz, 14-bit sampling). At each grid point (voxel) the motion of the optical fiber was paused and the laser was pulsed 10 times. Each averaged times series was rectified and smoothed (40 point moving average) to produce a signal representative of a velocity potential, which was copied to the matrix representative of the imaging operator. Each row in the imaging operator corresponded to the concatenated velocity potential acquired by each transducer at a position (voxel) in the imaging volume. Therefore, each column in the imaging operator corresponded to a time point for a particular transducer.

Two (2) additional imaging operators were derived from the experimental imaging operator. The first was produced by eliminating all signals below a specified threshold (referred to as the de-noised imaging operator). The second was produced by eliminating all signals above the same threshold (referred to as the noise-only imaging operator). The threshold was chosen such that photoacoustic transients representative of the point source were preserved. The threshold setting was approximately 15% of the maximum velocity potential intensity. Singular value decomposition of all three imaging operators was performed in MATLAB via the built-in function (svds).

## A2.3 Results

The decomposition of the system matrix yields a diagonal matrix of scalar values indicating the sensitivity of the system to the vectors in  $\mathbf{U}$  and  $\mathbf{V}^T$ . For each of the imaging operators, the magnitudes of the singular values were displayed versus their corresponding index in a log-linear plot (shown in Fig. A2.1). The singular values represented by the red curve, the black curve, and the blue curve, corresponded to the singular values of the experimental, de-noised, and noise-only imaging operators, respectively. The maximum number of singular values for each imaging operator was 6030, corresponding to the number of time points used to describe each voxel in the imaging volume. The magnitudes of the singular values below the minimum value selected on the y-axis were extremely small and were considered to be effectively zero. In order to better illustrate the trends in the useful region of the curve, the minimum value of the y-axis was selected to be  $10^0$ .

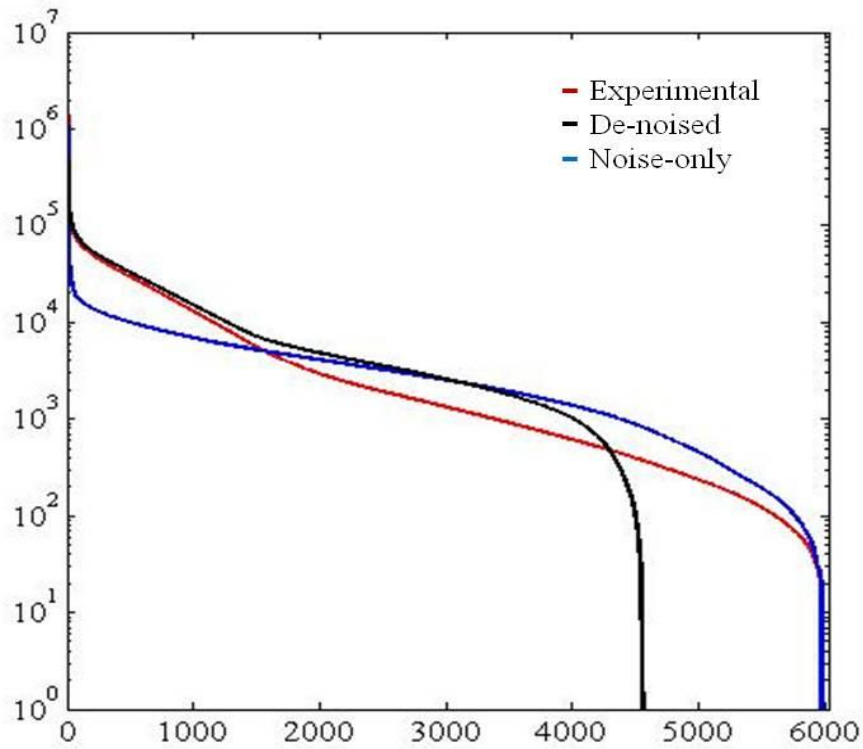


**Figure A2.1:** (a) Displays the magnitude of the singular values plotted against their index for the experimental imaging operator (red), the de-noised imaging operator (black), and the noise-only imaging operator (blue).

In order to better illustrate the differences in singular vector content for each of the imaging operators, representative object space singular vectors are shown in Fig. A2.2 in order to confirm the differing content of the vectors in each imaging operator. Figure A2.2(a) shows the centre planes of the 1<sup>st</sup> index singular vectors for the experimental and noise-only imaging operators, respectively. Figure A2.2(b) shows the centre planes of the 1555<sup>th</sup> index singular vectors for the experimental and noise-only imaging operators, respectively. At the 1555<sup>th</sup> index, the magnitudes of the singular values in experimental and noise-only imaging operators were equal. Figure A2.2(c) shows the centre planes of the 3134<sup>th</sup> index singular vectors for the de-noised and noise-only imaging operators, respectively. In a similar manner to Fig. A2.2(b), the magnitudes of the corresponding singular values at the 3134<sup>th</sup> index were equal.

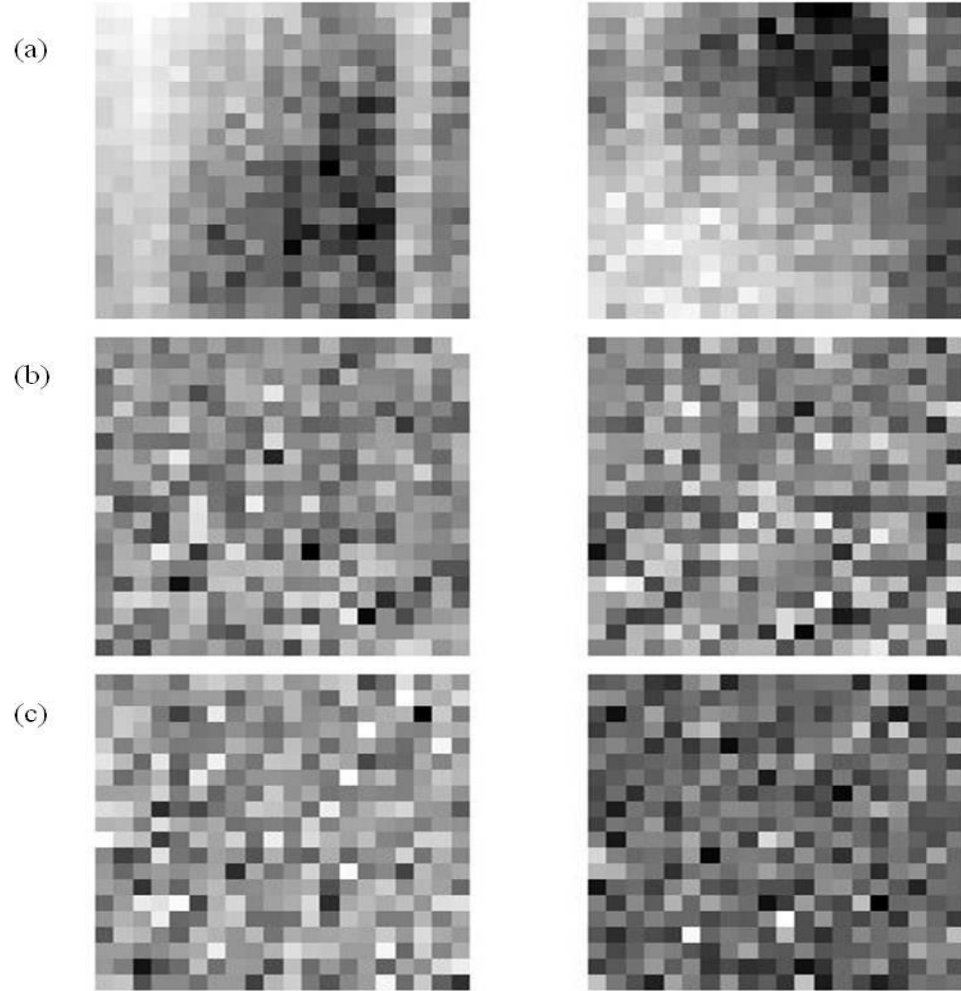


**Figure A2.2:** (a) Shows the centre planes of the singular vectors at the 1<sup>st</sup> index for the experimental and noise-only imaging operators. (b) Shows the centre planes of the singular vectors at the 1555<sup>th</sup> index for the experimental and noise-only imaging operators. (c) Shows the centre planes of the singular vectors at the 3134<sup>th</sup> index for the de-noised and noise-only imaging operators.

## A2.4 Discussion

Both the experimental (red) and de-noised (black) curves displayed in Fig. A2.1 show relatively similar trends as the magnitude of the singular values predictably decline until a threshold is reached where the subsequent singular values approach a zero value. It is expected that this threshold is reached sooner for the de-noised imaging operator as there is no background noise present in the imaging operator and, consequently, any vectors describing the system are provided by only photoacoustic signal. Of note is the

index at which the zero-threshold is reached by both the experimental and noise-only imaging operators is the same. This trend is expected as it is thought that at some index (after the de-noised zero-threshold), the content of the singular vectors is attributed to information provided by only the system noise.

The object space singular vectors shown in Fig. A2.2 confirm the content of the vectors differs even among the same index (and same singular value magnitude) of the imaging operators. The indices in which the singular values are equal were chosen to show explicitly that the vector space describing each of the imaging operators is different. While noise can be the cause of re-ordering singular vectors during the decomposition, the singular vectors shown in Fig. A2.2(a) show the lowest order singular vectors of two imaging operators indicating, still, that the content of the vectors differs among the imaging operators.

It is important to note the point at which the experimental and noise-only singular values cross each other is not the index where all subsequent singular vectors are produced by system noise, and so the crossing point does not fully identify the measurable number of singular vectors that contribute to objects in the field of view above the system noise. However, the singular vectors produced by the decomposition of the de-noised imaging operator are derived from photoacoustic signals almost exclusively (i.e. due to the nature of the thresholding procedure some system noise is still present in the signals). Therefore, a best estimate of the number of singular values and hence singular vectors that contribute to objects in the field of view above system noise is provided by the crossing of the de-noised and noise-only singular value plots at index 3134.

## **A2.5 Conclusion**

A technique was implemented to acquire an experimental imaging operator corresponding to a hemispherical array of 30 transducers with a specified imaging volume of  $30 \times 30 \times 30 \text{ mm}^3$  and step-size of 1.5 mm. Two additional imaging operators

were derived from the experimental imaging operator. The first represented a de-noised version of the experimental imaging operator, while the second represented a noise-only version of the experimental imaging operator. Singular value decomposition was performed on each of the three imaging operators and the magnitudes of the singular values declined with critical crossing points among the curves. The magnitudes of the singular values obtained from the experimental and de-noised imaging operators were larger than the singular values obtained from the noise-only imaging operator for indices below 1555 and 3134, respectively. Representative images at singular value indices of interest confirmed that the object space singular vector content was different among the three imaging operators. Based on the findings, approximately 3134 measurable singular vectors contribute to objects in the field of view for a staring photoacoustic transducer array with 30 transducers.

## **A2.6 References**

1. Xu, M. and Wang, L. V. , "Photoacoustic imaging in biomedicine," *Rev.Sci.Instrum.* 77(4) (2006).
2. Diebold, G. J., Sun, T. and Khan, M. I. , "Photoacoustic monopole radiation in one, two, and three dimensions," *Phys.Rev.Lett.* 67(24), 3384-3387 (1991).
3. Paltauf, G., Viator, J. A., Prael, S. A. and Jacques, S. L. , "Iterative reconstruction algorithm for optoacoustic imaging," *J.Acoust.Soc.Am.* 112(4), 1536-1544 (2002).
4. Kostli, K. P., Frauchiger, D., Niederhauser, J. J., Paltauf, G., Weber, H. P. and Frenz, M. , "Optoacoustic imaging using a three-dimensional reconstruction algorithm," *IEEE Journal on Selected Topics in Quantum Electronics* 7(6), 918-923 (2001).
5. Frauchiger, D., Kostli, K. P., Paltauf, G., Frenz, M. and Weber, H. P., "Optoacoustic tomography using a two dimensional optical pressure transducer and two different

reconstruction algorithms," Hybrid and Novel Imaging and New Optical Instrumentation for Biomedical Applications, June 18,2001 - June 21, 74-80 (2001).

6. Xu, M. H. and Wang, L. V. , "Universal back-projection algorithm for photoacoustic computed tomography," Photons Plus Ultrasound: Imaging and Sensing 2005 5697, 251-254 (2005).

7. Roumeliotis, M., Stodilka, R. Z., Anastasio, M. A., Chaudhary, G., Al-Abed, H., Ng, E., Immucci, A. and Carson, J. J. L. , "Analysis of a photoacoustic imaging system by the crosstalk matrix and singular value decomposition," Optics Express 18(11), 11406-11417 (2010).

8. Roumeliotis, M., Ephrat, P., Patrick, J. and Carson, J. J. L. , "Development and characterization of an omnidirectional photoacoustic point source for calibration of a staring 3D photoacoustic imaging system," Optics Express 17(17), 15228-15238 (2009).

9. Roumeliotis, M., Ephrat, P. and Carson, J. J. L. , "Development of an omni-directional photoacoustic source for the characterization of a hemispherical sparse detector array," Proc.SPIE 7177(1), 71772F (2009).



# Curriculum Vitae

**Michael Barret Roumeliotis**

## **EDUCATION**

---

Ph.D., Medical Biophysics, University of Western Ontario. (May 2008 – August 2011)

M.A.Sc., Engineering Physics, McMaster University. (September 2005 – December 2007)

B. Eng., Engineering Physics, McMaster University. (September 2001 – May 2005)

## **ACADEMIC AWARDS AND ACHIEVEMENTS**

---

Canadian Institute for Health Research, CaRTT – STP, 2009-2011. (\$53,400)

Society of Photo-Optical Instrumentation Engineers, April 2009. (\$2,000)

Western Graduate Research Scholarship, 2009-2011. (\$18,000)

Translational Breast Cancer Research Unit, 2008-2011. (\$69,300)

Dean's Honour List, McMaster University, 2003-2005.

Academic Excellence Scholarship, McMaster University, 2001. (\$1,000)

## **INTELLECTUAL PROPERTY**

---

Three dimensional photoacoustic imager. Jeffrey Carson, Pinhas Ephrat, Lynn Keenlside, and Michael Roumeliotis. United States Provisional Patent Application. File No. 37CFR1.76.

## **PEER-REVIEWED MANUSCRIPTS**

---

### Manuscripts

**M. Roumeliotis**, R.Z. Stodilka, E. Ng, J.J.L. Carson. "Estimate of effective singular values for a photoacoustic imaging system of varying transducer arrangement and sampling rate", *Optics Express* **19**(14), pp. 13405-13417, June 2011.

**M. Roumeliotis**, R.Z. Stodilka, M.A. Anastasio, G. Chaudhary, H. Al-Abed, E. Ng, A. Immucci, J.J.L. Carson. "Analysis of a photoacoustic imaging system by the crosstalk matrix and singular value decomposition", *Optics Express* **18**(11), pp. 11406-11417, May 2010.

P. Ephrat, G. C. Albert, **M. Roumeliotis**, M. Belton, F. S. Prato, J.J.L. Carson. "Localization of spherical lesions in tumour-mimicking phantoms by 3D sparse array photoacoustic imaging", *Medical Physics* **37**(4), pp. 1619-1628, 2010.

G.C. Albert, **M. Roumeliotis**, J.J.L. Carson. "Effect of temperature and freeze-thaw on gold nanorods", *Nanotechnology*, **20**(50), article: 505502, 2009.

**M. Roumeliotis**, P. Ephrat, J. Patrick, J.J.L. Carson. "Development and characterization of an omni-directional photoacoustic point source for calibration of a staring 3D photoacoustic imaging system", *Optics Express* **17**(17), pp. 15228-15238, 2009.

P. Ephrat, **M. Roumeliotis**, F. Prato, J.J.L. Carson. "Four-dimensional photoacoustic imaging of a moving target", *Optics Express* **16**(26), pp. 21570-21581, 2008.

## CONFERENCE PROCEEDINGS

---

### Manuscripts

E. Ng, F. Vasefi, B. Kaminska, **M. Roumeliotis**, J.J.L. Carson. "Three dimensional angular domain optical projection tomography" SPIE Annual Meeting, Symposium on Biomedical Optics (BiOS), 7897, San Francisco, USA, 2011.

**M. Roumeliotis**, M.A. Anastasio, J.J.L. Carson. "Estimate of effective singular values of a photoacoustic imaging system by noise characterization" SPIE Annual Meeting, Symposium on Biomedical Optics (BiOS), 7899-65, San Francisco, USA, 2011.

**M. Roumeliotis**, G. Chaudhary, M.A. Anastasio, R. Stodilka, A. Immucci, E. Ng, J.J.L. Carson. "Analysis of a photoacoustic imaging system by singular value decomposition" SPIE Annual Meeting, Symposium on Biomedical Optics (BiOS), 7564-113, San Francisco, USA, 2010.

G. Chaudhary, **M. Roumeliotis**, P. Ephrat, R.Z. Stodilka, J.J.L. Carson, M.A. Anastasio. "Characterization of sparse-array detection photoacoustic tomography using the singular value decomposition" SPIE Annual Meeting, Symposium on Biomedical Optics (BiOS), 7564-119, San Francisco, USA, 2010.

G. Chaudhary, M.A. Anastasio, **M. Roumeliotis**, J.J.L. Carson. "Comparison of reconstruction algorithms for sparse-array detection" SPIE Annual Meeting, Symposium on Biomedical Optics (BiOS), 7564-115, San Francisco, USA, 2010.

**M. Roumeliotis**, P. Ephrat, J.J.L. Carson. "Development of an omni-directional photoacoustic source for the characterization of a hemispherical sparse detector array" SPIE Annual Meeting, Symposium on Biomedical Optics (BiOS), 7177-88, San Jose, USA, 2009.

P. Ephrat, **M. Roumeliotis**, J.J.L. Carson. "Three-dimensional photoacoustic imaging of a moving target" SPIE Annual Meeting, Symposium on Biomedical Optics (BiOS), 7177-32, San Jose, USA, 2009.

## PRESENTATIONS AND ABSTRACTS

---

### *Peer-reviewed Abstracts*

E. Ng, F. Vasefi, B. Kaminska, **M. Roumeliotis**, J.J.L. Carson. "Three dimensional angular domain optical projection tomography" SPIE Annual Meeting, Symposium on Biomedical Optics (BiOS), 7897, San Francisco, USA, 2011. (Presentation)

**M. Roumeliotis**, M.A. Anastasio, J.J.L. Carson. "Estimate of effective singular values of a photoacoustic imaging system by noise characterization" SPIE Annual Meeting, Symposium on Biomedical Optics (BiOS), 7899-65, San Francisco, USA, 2011. (Presentation)

J.J.L. Carson, **M. Roumeliotis**, G. Chaudhary, R.Z. Stodilka, M.A. Anastasio. "3D photoacoustic imaging" Photonics North, 7750-45, Niagara Falls, Canada, 2010. (Presentation)

H. Al-Aabed, **M. Roumeliotis**, J.J.L. Carson. "Development of a hand-held 3D photoacoustic imaging system for breast cancer detection" Photonics North, 7750-127, Niagara Falls, Canada, 2010. (Presentation)

**M. Roumeliotis**, R.Z. Stodilka, M.A. Anastasio, J.J.L. Carson. "Analysis of a photoacoustic imaging system by singular value decomposition" COMP Annual Meeting, Ottawa, Canada, 2010. (Poster)

**M. Roumeliotis**, Govind Chaudhary, Mark Anastasio, Robert Stodilka, A. Immucci, Eldon Ng, J.J.L. Carson. "Analysis of a photoacoustic imaging system by singular value decomposition" SPIE Annual Meeting, Symposium on Biomedical Optics (BiOS), 7564-113, San Francisco, USA, 2010. (Poster)

G. Chaudhary, **M. Roumeliotis**, P. Ephrat, R.Z. Stodilka, J.J.L. Carson, M.A. Anastasio. "Characterization of sparse-array detection photoacoustic tomography using the singular value decomposition" SPIE Annual Meeting, Symposium on Biomedical Optics (BiOS), 7564-119, San Francisco, USA, 2010. (Poster)

G. Chaudhary, M.A. Anastasio, **M. Roumeliotis**, J.J.L. Carson. "Comparison of reconstruction algorithms for sparse-array detection" SPIE Annual Meeting, Symposium on Biomedical Optics (BiOS), 7564-115, San Francisco, USA, 2010. (Poster)

**M. Roumeliotis**, J.J.L. Carson. "Photoacoustic system characterization and four-dimensional imaging" BioPhotonics 2009, Ven, Sweden, 2009. (Presentation)

**M. Roumeliotis**, P. Ephrat, J.J.L. Carson. "Development of an omni-directional photoacoustic source for the characterization of a hemispherical sparse detector array" SPIE Annual Meeting, Symposium on Biomedical Optics (BiOS), 7177-88, San Jose, USA, 2009. (Poster)

P. Ephrat, **M. Roumeliotis**, J.J.L. Carson. "3D photoacoustic imaging of a moving target" SPIE Annual Meeting, Symposium on Biomedical Optics (BiOS), 7177, San Jose, USA, 2009. (Presentation)

### Poster Presentations

**M. Roumeliotis**, R.Z. Stodilka, M.A. Anastasio, J.J.L. Carson. "Analysis of a photoacoustic imaging system by singular value decomposition" COMP Annual Meeting, Ottawa, Canada, 2010.

**M. Roumeliotis**, Govind Chaudhary, Mark Anastasio, Robert Stodilka, A. Immucci, Eldon Ng, J.J.L. Carson. "Analysis of a photoacoustic imaging system by singular value decomposition" SPIE Annual Meeting, Symposium on Biomedical Optics (BiOS), 7564-113, San Francisco, USA, 2010.

**M. Roumeliotis**, P. Ephrat, J.J.L. Carson. "Development of an omni-directional photoacoustic source for the characterization of a hemispherical sparse detector array" SPIE Annual Meeting, Symposium on Biomedical Optics (BiOS), 7177-88, San Jose, USA, 2009.

**M. Roumeliotis**, P. Ephrat, J.J.L. Carson. "Development of an omni-directional photoacoustic source for the characterization of a hemispherical sparse detector array" Imaging Network Ontario, Toronto, Canada, 2008.

**M. Roumeliotis**, R. LaPierre. "Mesa-assisted Vapor-Liquid-Solid growth of GaAs nanowires" Canadian Semiconductor Technology Conference, Montreal, Canada, 2007.

**M. Roumeliotis**, R. LaPierre. "Periodic arrays of electron beam lithography patterned Au particles" Canada Nanoscience and Nanotechnology Forum, Waterloo, Canada, 2007.

### Oral Presentations

**M. Roumeliotis**, M.A. Anastasio, J.J.L. Carson. "Estimate of effective singular values of a photoacoustic imaging system by noise characterization" SPIE Annual Meeting, Symposium on Biomedical Optics (BiOS), 7899-65, San Francisco, USA, 2011.

**M. Roumeliotis**, H. Al-Abed, J.J.L. Carson. "Analysis of a photoacoustic imaging system via singular value decomposition and the crosstalk matrix" Ontario Photoacoustics Workshop, Toronto, Canada, 2010.

**M. Roumeliotis**. "Photoacoustic system characterization and four-dimensional imaging" BioPhotonics 2009, Ven, Sweden, 2009.

**M. Roumeliotis**, R. LaPierre. "Mesa-assisted Vapor-Liquid-Solid growth modeling of GaAs nanowires" Centre for Emerging Device Technology, Hamilton, Canada, 2006.